博士論文

Study on Melted Fuel Debris Material Analysis by Portable X-band Linac Neutron Source

(可搬型 X バンドライナック中性子源による溶融燃料デブリ成分分析の研究)

クスマワティ　ユディティヤ

(Yudhitya Kusumawati)

Contents

List of Figures

List of Tables

Abstract

Study on Melted Fuel Debris Material Analysis by Portable X-band Linac Neutron Source

Yudhitya Kusumawati

The University of Tokyo, 2019

After the Fukushima Daiichi nuclear reactor incident, as part of its decommissioning project, unaccountable nuclear fuel debris especially the ones from the reactor core are subject of nuclear safeguards and criticality safety which needs to be removed. In order to contribute to efficient debris extraction process, on-site nuclear debris screening activity is necessary. The proposed screening activity will consist of two different methods that complements each other: polychromatic X-ray CT and neutron resonance transmission analysis (NRTA). The latter is a method to identify isotopes inside a material and has been widely used in nuclear data analysis by using high-energy neutron sources in various accelerator facility in the world. This research introduced the short-distance NRTA using the compact, mobile version of neutron source for the purpose of on-site screening of nuclear fuel debris.

By using 3.95 MeV X-band electron linac coupled with tungsten as electron-to-photon converter and beryllium as photon-to-neutron converter, a compact pulsed neutron source with high mobility can be realized for the purpose short-distance neutron time-of-flight (TOF) measurement and performing NRTA of the nuclear debris content. Experiment result show this system can measure neutron energy spectrum up to 100 eV with only 2.5 meters TOF path distance in regards to the X-band accelerator's short pulse. Within this energy range, neutron energy absorption value for ^{235}U, ^{238}U, ^{239}Pu, ^{240}Pu and ^{242}Pu happens, and their resonance peaks should be able to be observed. By using tungsten and indium as dummy sample with the closest neutron energy absorption value with ^{238}U and ^{240}Pu respectively, short-distance NRTA with ^{3}He neutron detector has been performed successfully, and it shows the capability of simultaneous multiple isotopes identification as well. The smallest sample this system can measure is $20 \times 20 \times 1.2$ mm^3 within 2 hours. It proves that this system is feasible to detect uranium and plutonium inside nuclear debris, through the observation of neutron energy absorption by limited U/Pu isotopes of ^{235}U, ^{238}U, ^{239}Pu, ^{240}Pu and ^{242}Pu.

With its compact size and short TOF path, this advantage will make the system able to be implemented in on-site nuclear debris screening system as a complementary of polychromatic X-ray CT imaging method in clarifying the existence of uranium and plutonium inside nuclear debris. Combination of them will be used to obtain nuclear debris material density data necessary for nuclear debris activity mapping of Fukushima Daiichi reactor core area, as well as criticality control of nuclear debris storage.

Acknowledgements

I would like to express my gratitude to the people who have helped me and made contribution to this dissertation. Without their guidance and support, the completion of this dissertation would not become possible.

I am particularly thankful to Professor Uesaka Mitsuru, who had been advising and guiding me as supervisor for the past five years since my master study. Being a student under his lab, I have learned a lot of valuable knowledge and experience, and thanks to him too I got the chance to participate in scientific conferences, be it national or international abroad, and even participate in experiments and research meetings outside Japan. On a personal level, his provisions on financial, positive personality and encouragement also have been one of my greatest supports during my time studying here.

I would also like to thank Mitsuya Yuki-san, as he is one of the most important people that had helped a lot during the completion of this dissertation. He guided me on many things regarding this topic, especially on technical matters for the experiments, when I have very little knowledge about it on the beginning. I really appreciate his help and cooperation during the time working on this research theme.

I am also grateful for the help from other researchers I worked with on this research theme. The people from JAEA and their Nuclear Sensing Group in which I did a fellowship research work for a while there, the people from GELINA, and from The University of Sheffield and The University of Bristol who became a host for the research meeting, especially the people at Tokai, Dobashi Katsuhiro-san and Kusano Joe-san, who always assist me in operating the linac for the experiments. My deepest thanks also go to the other students in Uesaka lab for their support both in academics and daily life, and always make the lab atmosphere lively as well.

And then I am also thankful all my friends in Tokyo who have been very supportive and helpful during my time in here, who are always willing to meet up, doing activities and chat together, as well as my online friends who always up for talks and become an effective stress-reliever.

Lastly, I would like to thank God, who always gives me strength to move forward, and my parents and family in Indonesia who never stop encouraging and supporting me during my doctoral program and dissertation completion.

1. Introduction

Fukushima Daiichi Nuclear Power Station is located along the central Pacific coast of Fukushima Prefecture, straddling the towns of Futaba and Okuma in the Futaba District. The site is a semi-elliptical shape stretched along the coast and covers approximately 3,500,000 m^2 of the area. This power station complex has six boiling water reactors (BWR), where unit 1 to 4 are in the southern area and unit 5 to 6 are in the northern area. Unit 1 has a generator output of 460MW, Unit 2 to 5 each have output capacity of 784MW, all having the Mark-I type primary containment vessel (PCV), except unit 6 which is a Mark-II PCV that has an output capacity of 1,100MW. The total generation capacity of the power station is 4,696MW, and the six units commenced commercial operation in succession, starting with Unit 1 in March 1971 through Unit 6 in October 1979[1]. Figure 1.1 shows the picture of the inside structure of Fukushima Daiichi power reactors[2].

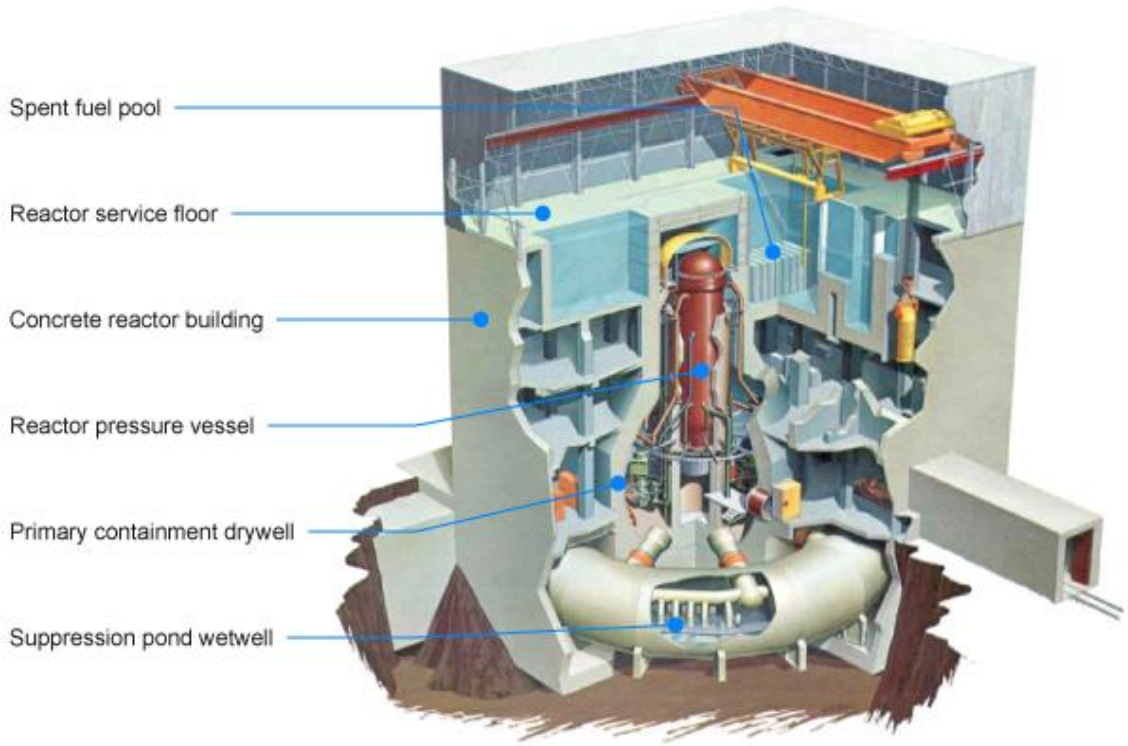

Figure 1.1 The inside structure of Fukushima Daiichi reactors.

When the disaster struck on March 11, 2011, Unit 1 to 3 were in operation at rated power output, while Unit 4 to 6 were in outage for periodic inspection. However, due to the Tohoku great earthquake occurring at 14:46, whose focal area widely ranged from offshore of Iwate Prefecture to offshore of Ibaraki Prefecture, all reactors in operation were automatically shut down. At the same time, all off-site electric power supply (the ones supplied via power transmission lines and other sources) to Fukushima Daiichi was lost due to the earthquake, but the emergency diesel generators (EDGs) supplied the electric power needed to maintain reactor safety.

Later at Fukushima Daiichi, a huge tsunami on the scale of historical proportions subsequently arrived and flooding many power panels, causing EDGs in operation except for Unit 6 to shut down. This resulted in the loss of all AC power (station black out) and the cooling function of the reactor core was shut down as well. In addition, at Units 1 to 3, the loss of DC power resulted in the sequential shut down of core cooling functions, which were designated to be operated without AC power supply. As the decay heat removal function inside the reactor was lost due to flooding of the cooling seawater pumps, alternative water injection of freshwater and seawater using fire engines through the Fire Protection (FP) line was conducted.

However there remained the situation where water could not be injected into the reactor pressure vessels (RPVs) in Unit 1 to 3 for a certain period of time. Consequently, the fuels in each unit were exposed without water, damaging the fuel claddings. The radioactive materials in the fuel rods were released into the RPV, and the chemical reaction between the fuel claddings (zirconium) and steam caused the generation of a substantial amount of hydrogen which raised the internal pressure of the PCV. At that point, PCV venting was attempted several times, but explosions caused by hydrogen leakage from the PCV destroyed the upper structures of the reactor buildings[1]. Due to volatile and easily-airborne fission products being carried with the hydrogen and steam, the venting and hydrogen explosions discharged a lot of radioactive material into the atmosphere, notably iodine and cesium.

After that, cooling water injection and cooling functions in each unit were successfully restored through accident response actions. Major fuel melting occurred early on in all three units, though the fuel remains essentially contained[2]. Nevertheless, the accident escalated into a chain of events and developed into a serious nuclear disaster.

1.1 The need for Fukushima Daiichi reactor core debris removal

After the incident, the reactor cores of Fukushima Daiichi nuclear reactor suffered from relatively serious damage due to the fuel melting that happened between the absence of cooling water in the PCV. Even when the reactor fuel is safely contained now, the massive amount of melted fuel debris is subject to nuclear safeguards and criticality safety. Therefore, as a part of the decommissioning project of Fukushima Daiichi, nuclear fuel debris removal from the containment vessel is necessary for further control through measuring and quantification.

1.1.1 Condition of the reactor core in Fukushima Daiichi unit 1, 2, and 3 after the accident

Nuclear Damage Compensation and Decommissioning Facilitation Corporation (NDF), who is in charge of formulating strategy and provide technical support for nuclear reactors decommissioning process, has been investigating and working on the strategy for the decommissioning of Fukushima Daiichi nuclear reactor Unit 1, 2 and 3. They are periodically updating the latest condition and progress of the reactor core PCV of each unit, including the strategy to handle the current problem in them such as fuel debris retrieval.

After some technical inspection using remote technology such as robots and non-destructive inspection like muon detection system, the information of the current condition of the three units has been able to be retrieved for further analysis. The latest condition of Fukushima Daiichi unit 1, 2, and 3 are shown in the figure 1.2 to figure 1.4[3].

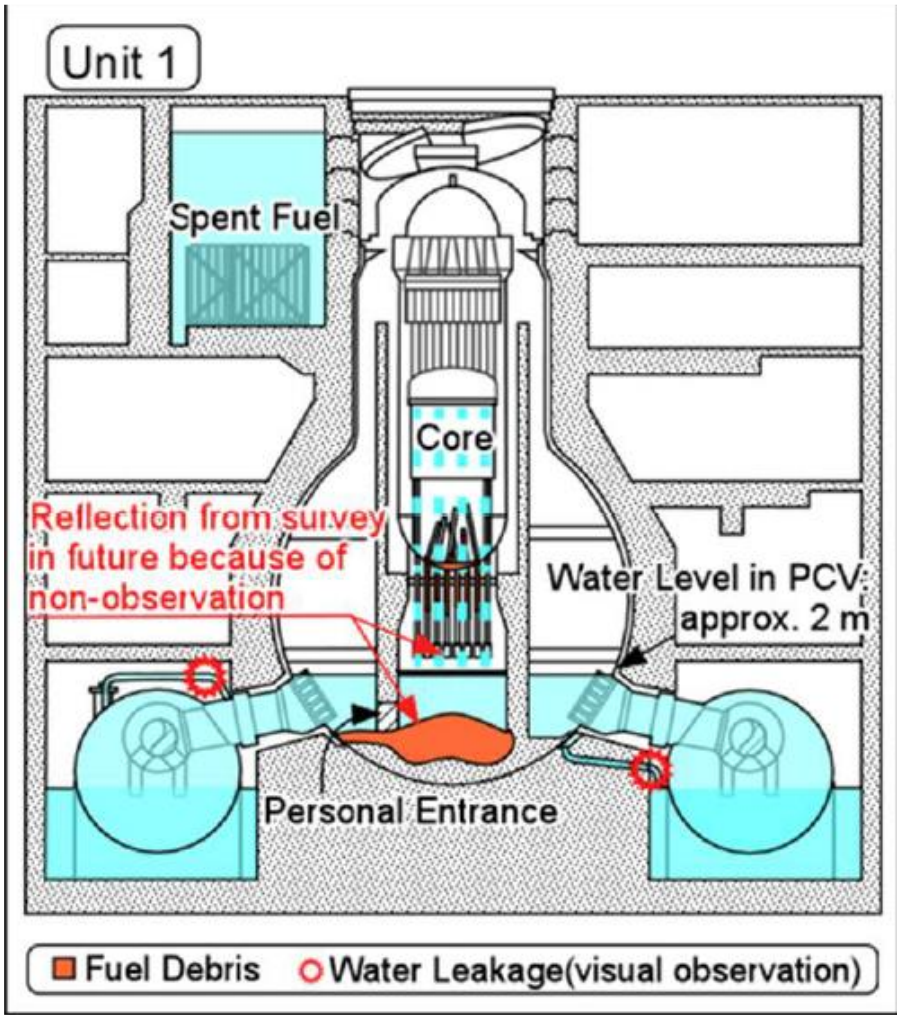

Figure 1.2 Schematic of the current status of the Fukushima Daiichi Unit 1 nuclear reactor PCV.

Table 1.1 Current status of the Fukushima Daiichi Unit 1 nuclear reactor PCV.

Core region	**RPV lower head**	**Pedestal (inside)**	**Pedestal (outside)**
Little fuel remains.	• A small amount of fuel debris is still present. • A small amount of fuel debris is present in the inside and on the outer surface of the CRD housing.	Most of fuel debris is present.	Fuel debris may have spread on the pedestal outside through the personal entrance.

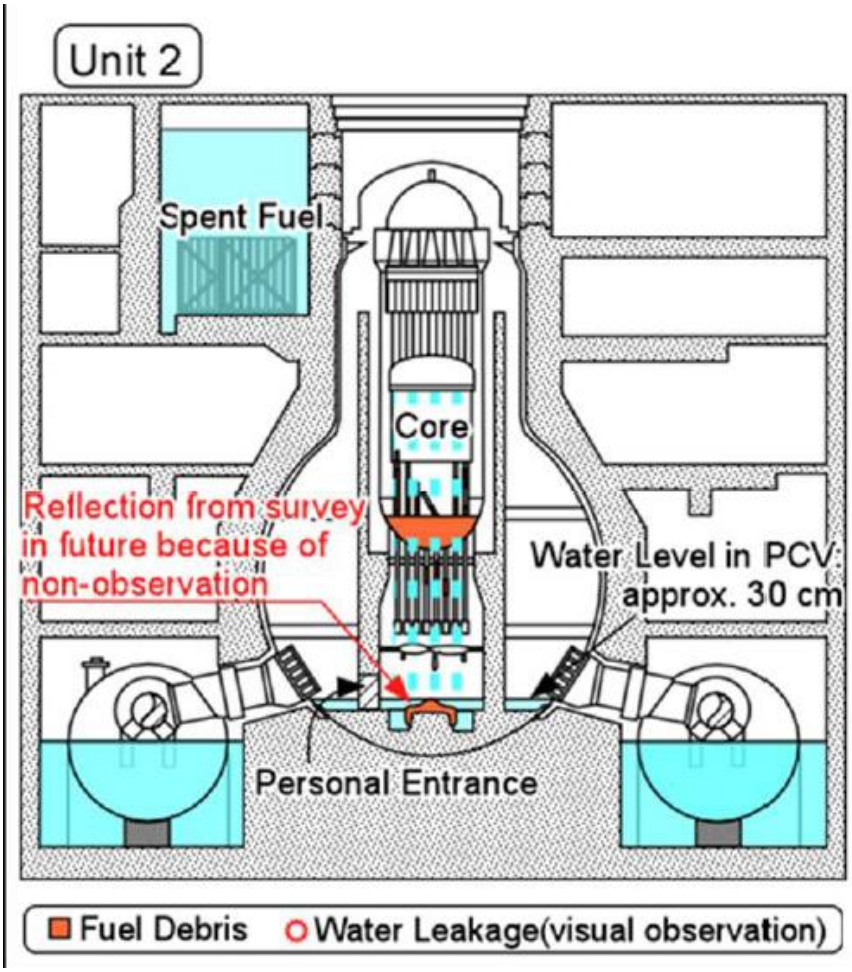

Figure 1.3 Schematic of the current status of the Fukushima Daiichi Unit 2 nuclear reactor PCV.

Table 1.2 Current status of the Fukushima Daiichi Unit 2 nuclear reactor PCV.

Core region	**RPV lower head**	**Pedestal (inside)**	**Pedestal (outside)**
• Little fuel remains. • (Stub-shaped fuels might exist in peripheral region.)	• Large amount of fuel debris is still present. • A small amount of fuel debris is present in the inside and on the outer surface of the CRD housing.	A small amount of fuel debris is present.	The possibility of fuel debris spreading on the pedestal outside through the personal entrance is low.

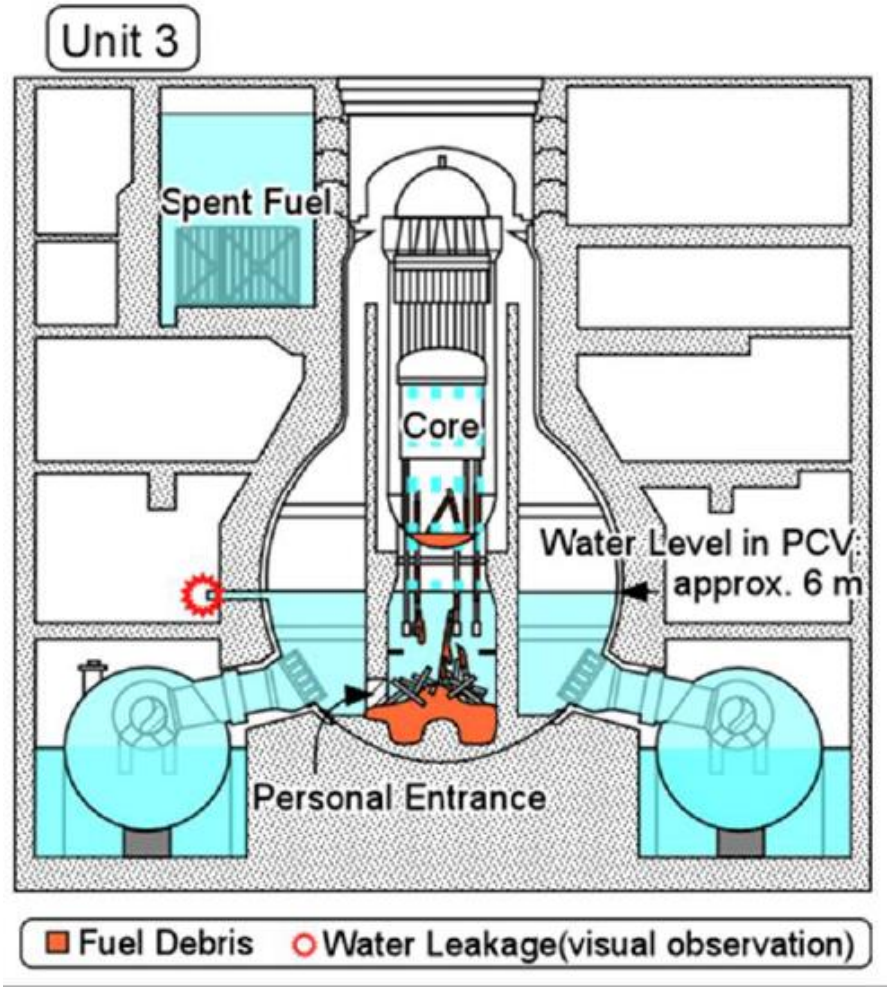

Figure 1.4 Schematic of the current status of the Fukushima Daiichi Unit 3 nuclear reactor PCV.

Table 1.3 Current status of the Fukushima Daiichi Unit 3 nuclear reactor PCV.

Core region	**RPV lower head**	**Pedestal (inside)**	**Pedestal (outside)**
Little fuel remains.	• Fuel debris remains on the RPV lower head partly. • A small amount of fuel debris is present in the inside and on the outer surface of the CRD housing.	Amount of fuel debris in Unit 3 is larger than that in Unit 2.	Fuel debris may have spread on the pedestal outside through the personal entrance.

1.1.2 Strategy of nuclear fuel debris retrieval method from Fukushima Daiichi unit 1, 2, and 3

Decommission activity of a nuclear reactor is a very long and complicated process, especially in the case of Fukushima Daiichi nuclear reactor where it was struck by an accident of the melted reactor core, resulting in the addition of the reactor parts to be cleaned up. Therefore, any effort to a more efficient decommissioning process is a very valuable asset. Based on the current condition of the PCV in Fukushima Daiichi Unit 1, 2, and 3, strategies for nuclear debris retrieval method has been planned by NDF.

In order to evaluate the feasibility of the fuel debris retrieval method, which are based on combination of water level and access routes, three priority methods have been selected. These strategies for nuclear debris retrieval are shown in figure 1.5 to 1.7[3].

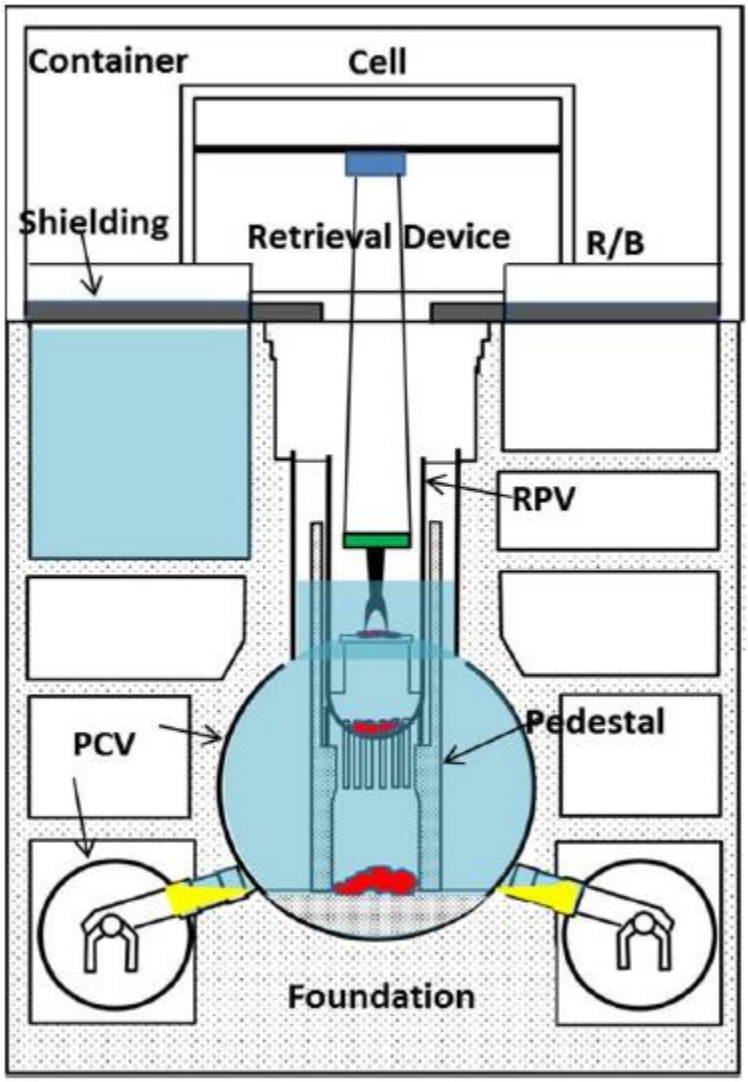

Figure 1.5 Schematic of the Submersion-Top Access method.

1. Submersion-Top Access method: Fuel debris is accessed from the top. PCV will be completely filled with water or filled with water to a level at which the fuel debris is present. However, there is a risk for water leakage and development of technologies for remotely fixing penetration holes for water sealing is difficult.

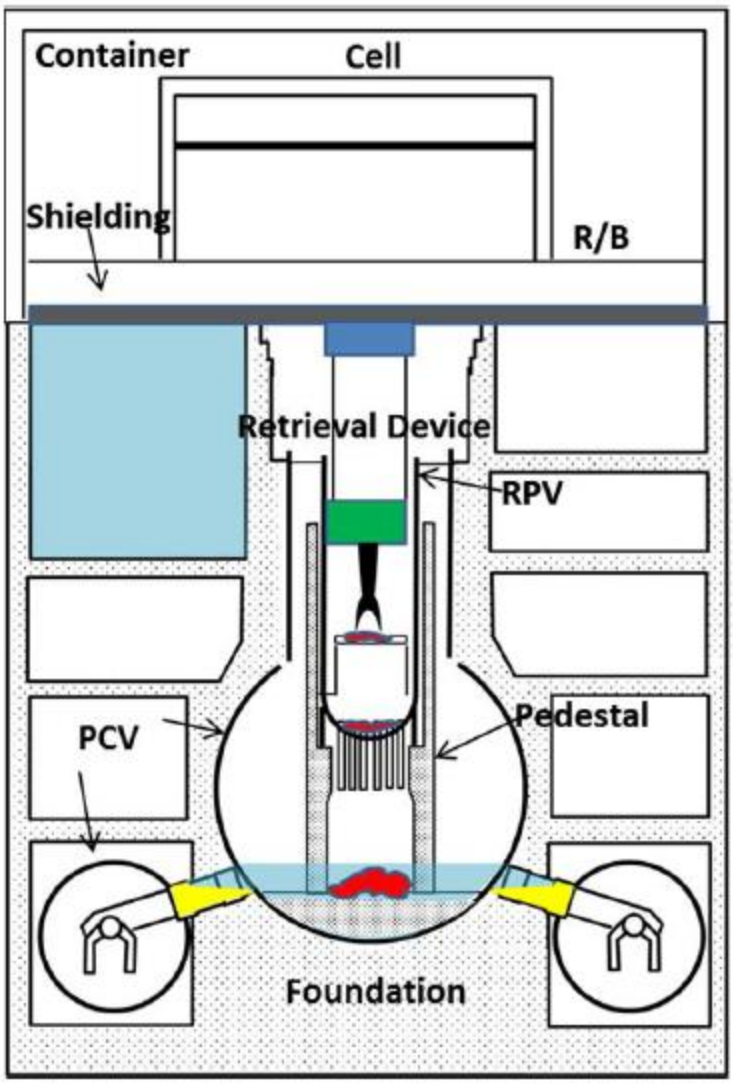

Figure 1.6 Schematic of the Partial Submersion - Top Access method.

2. Partial Submersion - Top Access method: Fuel debris is accessed from the top. Part of fuel debris will be dealt with in the air without water covering in the PCV. Risk for water leakage can be dealt in less complicated way than the full submersion method, but it is necessary to develop gas-control system and technology for maintaining negative pressure in order to contain alpha-emitting nuclides in the gas-phase portion.

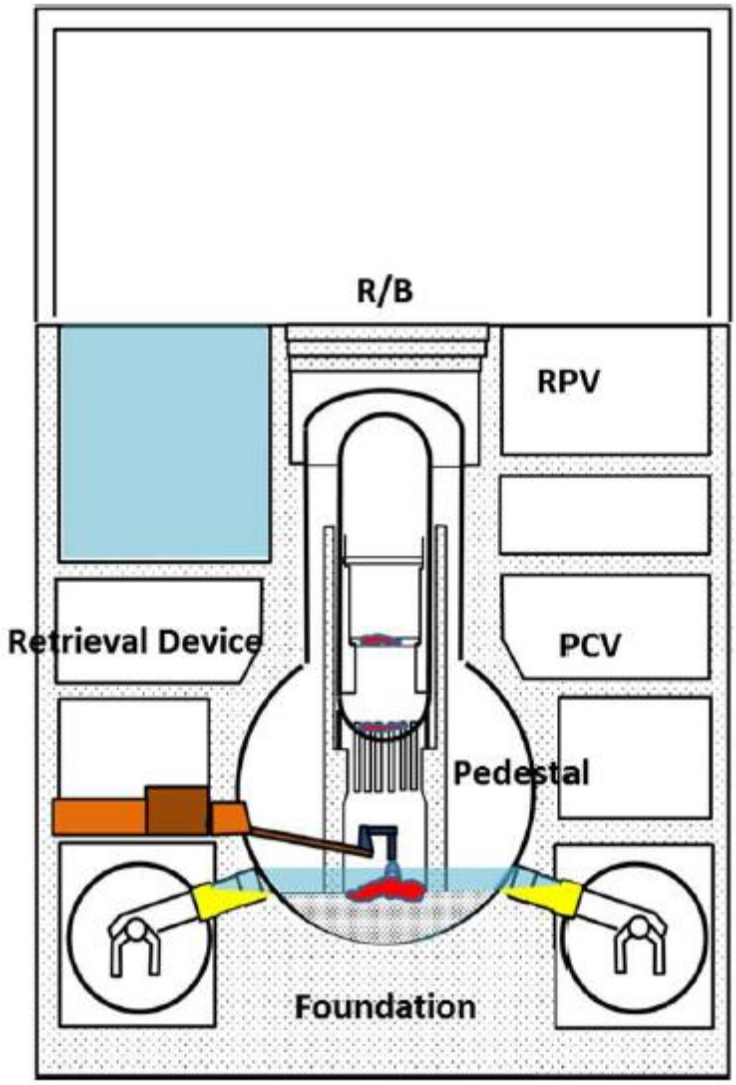

Figure 1.7 Schematic of the Partial Submersion - Side Access method.

3. Partial Submersion - Side Access method: Fuel debris is accessed from the side. Part of fuel debris will be dealt with in the air without water covering in the PCV. From the feasibility of access routes, this method is more difficult than the top access method, but it is more reasonable to retrieve the fuel debris at the bottom of PCV from the side. It is also can reduce the radiation exposure rate of workers and equipment performing maintenance work.

From the three strategies explained above, it is more realistic to retrieve the fuel debris from the bottom of the PCV first by accessing it from the side of the PCV (Partial Submersion - Side Access method), due to the following reasons:

- The bottom of the PCV in Units 1 to 3 has been investigated and, as a result, a certain amount of knowledge on the routes for accessing the bottom from the side has been accumulated, which can be used for realistic engineering.

- The actual time to reach the fuel debris will be longer when accessing the inside of the RPV from the top than when accessing the bottom of the PCV from the side.

- In order to streamline the decommissioning process as a whole, preparations for side access to the bottom of the PCV can be made concurrently with the removal of the fuel from the pool.

According to the roadmap for fuel retrieval from Fukushima Daiichi nuclear reactor unit 1, 2, and 3, trial fuel extraction from unit 1 and 2 is scheduled to be started from 2021, as shown in the timeline pictured in figure 1.8[4]. This roadmap was planned by NDF and Ministry of Economy, Trade and Industry (METI).

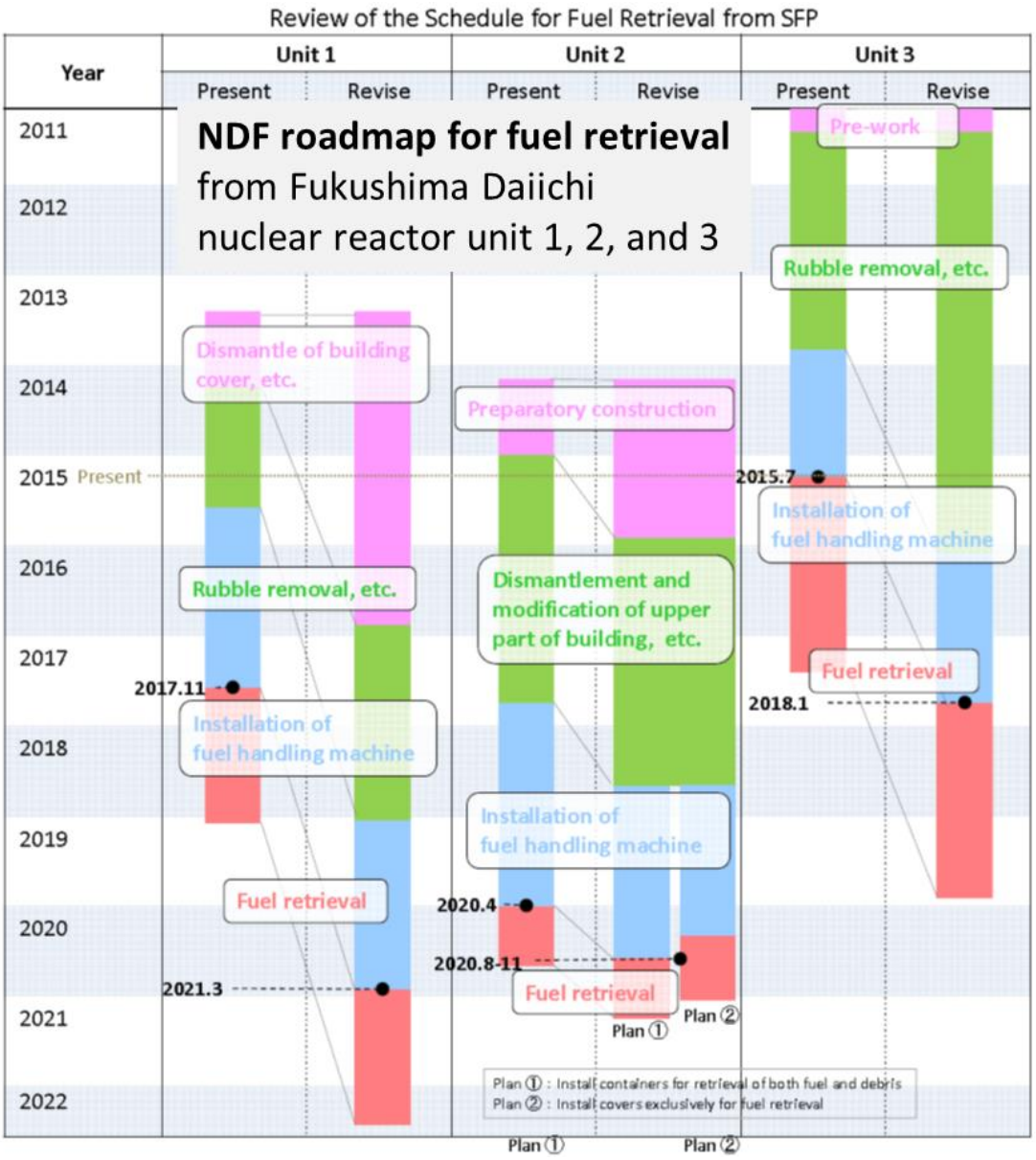

Figure 1.8 Roadmap of the Fukushima Daiichi nuclear reactor fuel retrieval project for Unit 1, 2, and 3.

1.1.3 Nuclear fuel debris

Debris are expected to be appearing during the Fukushima Daiichi accident, but in this case, the debris that needs special treatment is the one that contains radioactive material, or nuclear debris, as we call it. The most critical nuclear debris is the one at the reactor pressure vessel which small part of it has melted due to the heat from fissile products after cooling failure incident happened. Nuclear debris in the reactor pressure vessel mainly came from the rock of solidified melted fuel. These rocks also came in various shape as shown in the figure 1.9, based on the investigation of the nuclear debris from TMI-2 (Three Mile Island 2) nuclear reactor accident. The prediction of the contents of these solid nuclear debris is as pictured in figure 1.10.

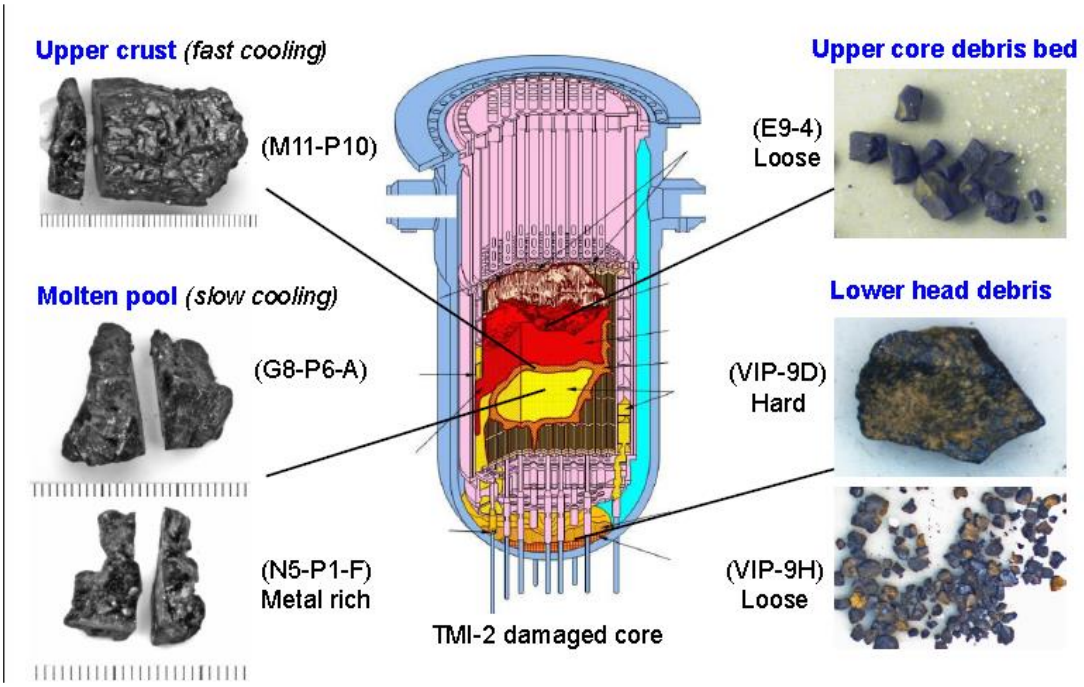

Figure 1.9 Core melt fuel debris specimens from TMI-2 nuclear reactor[5].

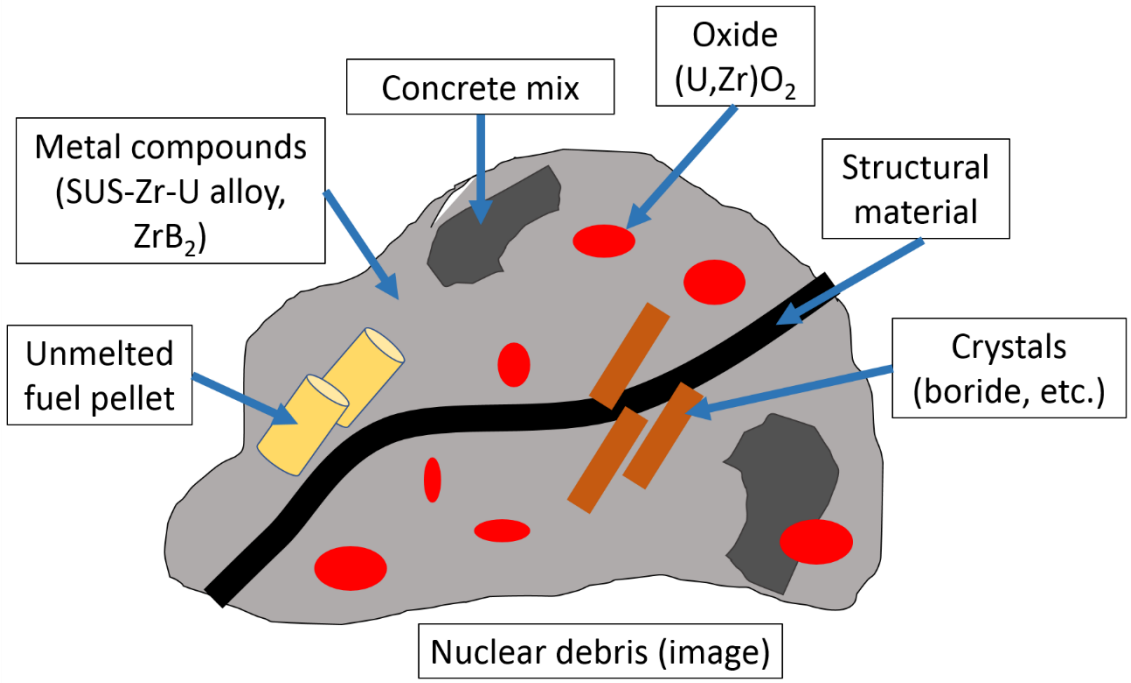

Figure 1.10 Image of the estimated contents of nuclear debris.

These solid nuclear fuel debris were formed from a phenomenon called Molten Core-Concrete Interactions (MCCI) that occurred during a nuclear reactor core meltdown, usually when an accident like Fukushima Daiichi nuclear reactor accident happens. The core of a nuclear reactor consists of uranium dioxide in the fuel, zirconium in the fuel rod cladding, carbon steel and stainless steel in other structures. At high temperatures, zirconium is oxidized by water vapor, so the main elements of core melt (corium) are UO_2, ZrO_2, Zr, Fe, Cr and Ni. The density of corium is around 6000-7000 kg/m^3.

Melting point of the pure oxides is around 2700° C while metals melt at 1350-1900° C, causing the corium to change from solid to liquid over a range of temperatures since mixtures of different species do not have single melting points. Solid concrete and the molten corium pool may be separated by a thin layer of partly molten concrete, which later rises upwards as “streamers” because it is less dense and cause mixing of the liquids. A layer of solid corium crust may also exist at the core-concrete interface, which probably porous and permeable to gases from the concrete.

The oxides in corium and concrete are miscible with each other, but the metallic ones are not. Because of this, a metallic layer may be formed on the surface of the oxidic pool since the metals are lighter than the corium oxide. When concrete oxides are added to the melting mix, its density decreases eventually below the density of the metals, causing the metallic layer to relocate to the bottom of the pool. Intense stirring of the pool by the rising gas bubbles may cause the metals and the oxides to be mixed with each other.

The corium is continuously heated by the radioactive decay of the fission products in it, with chemical reaction heat as another heat source. The most important chemical reaction in the corium pool is the oxidation of metals by the concrete decomposition gases, as shown in the chemical reaction diagram below[6]. The image cross-section of the MCCI result is shown in figure 1.11.

$$Zr + 2\ H_2O \rightarrow ZrO_2 + 2\ H_2 + 6.3\ MJ/kg_{Zr}$$

$$Zr + 2\ CO_2 \rightarrow ZrO_2 + 2\ CO + 5.7\ MJ/kg_{Zr}$$

$$2\ Cr + 3\ H_2O \rightarrow Cr_2O_3 + 3\ H_2 + 3.6\ MJ/kg_{Cr}$$

$$2\ Cr + 3\ CO_2 \rightarrow Cr_2O_3 + 3\ CO + 2.8\ MJ/kg_{Cr}$$

$$Fe + H_2O + 3.0\ kJ/kg_{Fe} \rightarrow FeO + H_2$$

$$Fe + CO_2 + 480\ kJ/kg_{Fe} \rightarrow FeO + CO$$

The reduction of SiO_2 and Fe_2O_3 by zirconium also plays an important role:

$$Zr + SiO_2 \rightarrow ZrO_2 + Si + 1.6\ MJ/kg_{Zr}\ (T<1870°\ C)$$

$$Zr + 2\ SiO_2 + 4.7\ MJ/kgZr \rightarrow ZrO_2 + 2\ SiO(g)\ (T>1870°\ C)$$

$$3\ Zr + 2\ Fe_2O_3 \rightarrow 3\ ZrO_2 + 4\ Fe + 5.8\ MJ/kg_{Zr}$$

$$Si + 2\ H_2O \rightarrow SiO_2 + 2\ H_2 + 15\ MJ/kg_{Si}$$

$$Si + 2\ CO_2 \rightarrow SiO_2 + 2\ CO + 14\ MJ/kg_{Si}$$

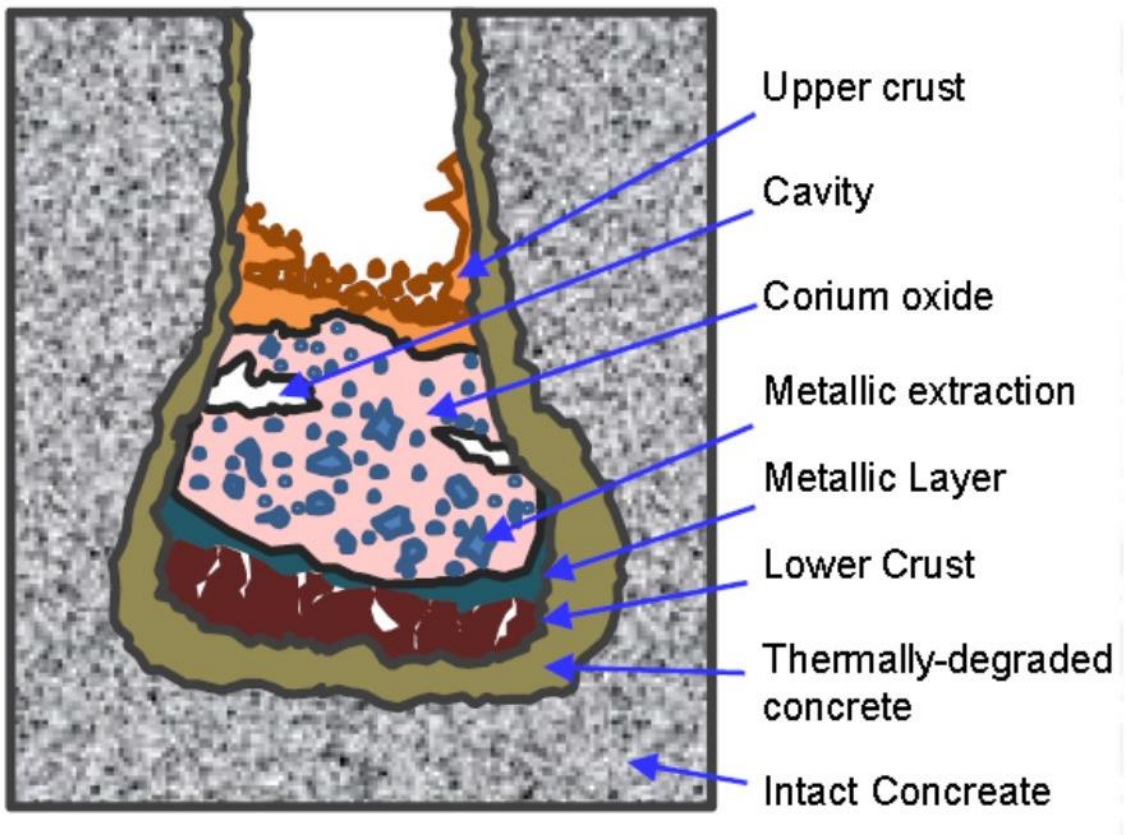

Figure 1.11 Image cross-section of MCCI.

Several research on MCCI simulations of Fukushima Daiichi reactor core PCV has been done in order to get the realistic condition of the nuclear debris. One of it was done by collaboration with JAEA and French Atomic Energy and Alternative Energies Commission (CEA). The experiment was performed at engineering-scale MCCI Test Facility VULCANO, France[7]. The setup of this MCCI simulation is pictured in figure 1.12.

From the research on MCCI, it can be learned that nuclear debris from the reactor core mostly contains mixed material between zirconium, iron (stainless steel), chromium, and uranium. Zirconium, uranium and silicone came in oxide phase, while iron and chromium came in metallic phase. The SEM analysis result shown in figure 1.13 shows the elements contained in nuclear debris obtained from the MCCI simulation mentioned previously.

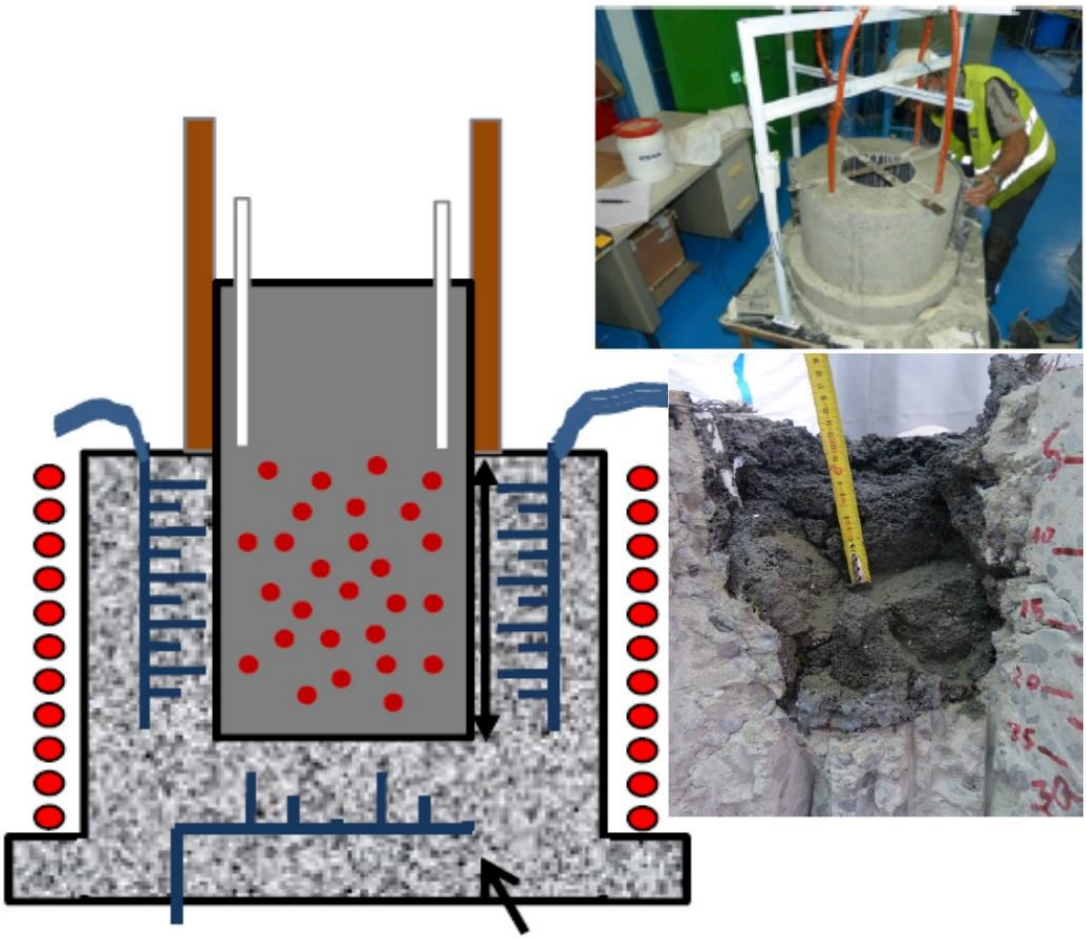

Figure 1.12 Engineering-scale MCCI simulation at VULCANO facility (CEA, France).

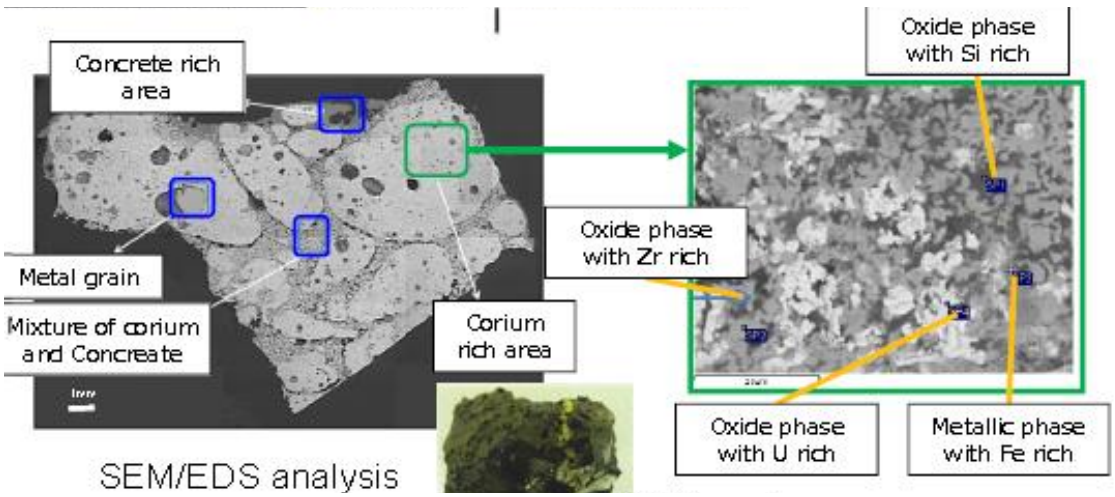

Figure 1.13 Scanning electron microscope images of the sample from MCCI simulation.

From recent research, study on the 1F nuclear debris composition has been performed through the evaluation of the actual nuclear debris that are managed to be extracted. As the condition happening to 1F reactor core is similar to TMI-2, comparison between their respective nuclear debris composition was done. Table 1.4 shows the main elements found in reactor core nuclear debris, such as uranium and zirconium, and their weight ratio (mol %) in the nuclear debris obtained from different reactors[8].

Table 1.4 Weight ratio (wt%) of core materials from 1F (BWR) and TMI-2 (PWR).

	1F (unit 1)	**1F (unit 2,3)**	**TMI-2**
U/Zr/Fe/B mol%	31.8/38.8/24.7/4.7	31.4/38.5/25.4/4.7	–
U/Zr/Fe/AgInCd mol%	–	–	50.5/37.0/8.9/3.7
U/Zr mol%	45.1/54.9	44.9/55.1	57.7/42.3

From the data shown in table 1.4, the weight ratio of U/Zr between 1F and TMI-2 don't have significant difference, and therefore can be assumed that the conditions of the nuclear debris in both reactors are similar. The analysis result of TMI-2 should be able to be used as a valid reference to estimate the nuclear debris condition in 1F before screening is conducted. Further details of the nuclear debris composition of TMI-2 is shown in table 1.5, where it is divided according to the location of the retrieved debris[5]. The data from the table shows that each of the sample debris from different locations contains 70~80% of $(U,Zr)O_2$ in average. Therefore, $(U,Zr)O_2$ can be expected to be the material target for on-site screening.

Table 1.5 Characteristics of TMI-2 core melt specimens.

Location	**Sample name**	**$(U,Zr)O_2$ matrix part**	**Precipitation**
Upper crust	M11-P10	C-$(U,Zr,Fe,Cr,Ni)O_2$ (large part) U~77at%, Fe+Cr+Ni ≤ 3at%, O/U~2.0, T+M (slightly)	(scarce)
Molten pool	G8-P6-4	C-$(U,ZrFe,Cr,Ni)O_2$ U 66~79 at% (av.) Fe+Cr+Ni 1~3at%, O/U~2.0, T+M (slightly)	Fe-Cr-Ni
	N5-P1-F	C-$(U,Zr,Fe,Cr)O_2$ U~75 at%, Fe+Cr ~2at%, O/U~2.0	Ag-In-Sn Ni-Sn Fe-Cr

		T(+M)-(U,Zr,Fe,Cr)O_2, U~21at%, Fe+Cr~4at%	
Upper core debris bed	E9-4	C-(U,Zr,Fe,Cr,Ni)O_2 U~93, 77 at%, Fe+Cr+Ni~2at%, O/U~2.0 Unmolten UO_2 pellet (a=0.5468 nm)	Fe-Cr-Ni Al-O
Lower head debris	VIP-9D (hard)	C-(U,Zr,Fe,Cr)O_{2+x} U 81~83 at%, Fe+Cr~4at%, O/U > 2.2	Fe-Cr-Ni-Al-O
	VIP-9H (loose)	C-(U,Zr,Fe,Cr)O_{2+x} U 79~87 at%, Fe+Cr 1.5~4at%, O/U > 2.2	Fe-Cr-Ni-Al-O

As for the reference of the nuclear debris shape estimation, experiment done by Kazakhstan National Nuclear Center (NNC) simulate the cooling process of the reactor core that leads to the production of nuclear debris[9]. The materials used in this experiment were a total 60 kg of UO_2 (71.5%), Zr (27.8%), B_4C (0.7%), and various SUS alloy. The device used to perform this experiment is called LAVA-B, one of the reactor core simulators used to investigate processes related to interaction between corium melt and water/concrete, typical in loss of coolant (LOCA) type accident. The schematic of LAVA-B is shown in figure 1.14. The subjected materials are put on the stainless-steel tray.

Two different cooling speed, slow and rapid, were simulated, and each of the process produced different type of debris. Slow cooling produced mostly solidified debris, and rapid cooling produced mostly powder debris. As the solidified debris were too large and difficult to be extracted, the target debris possible to be extracted for screening is the powder type debris. In the slow cooling process, ratio of the powder debris is only 13.6%, while rapid cooling produces 83.4% powder debris. Schematics and the ratio of the debris produced by each cooling process are shown in figure 1.15.

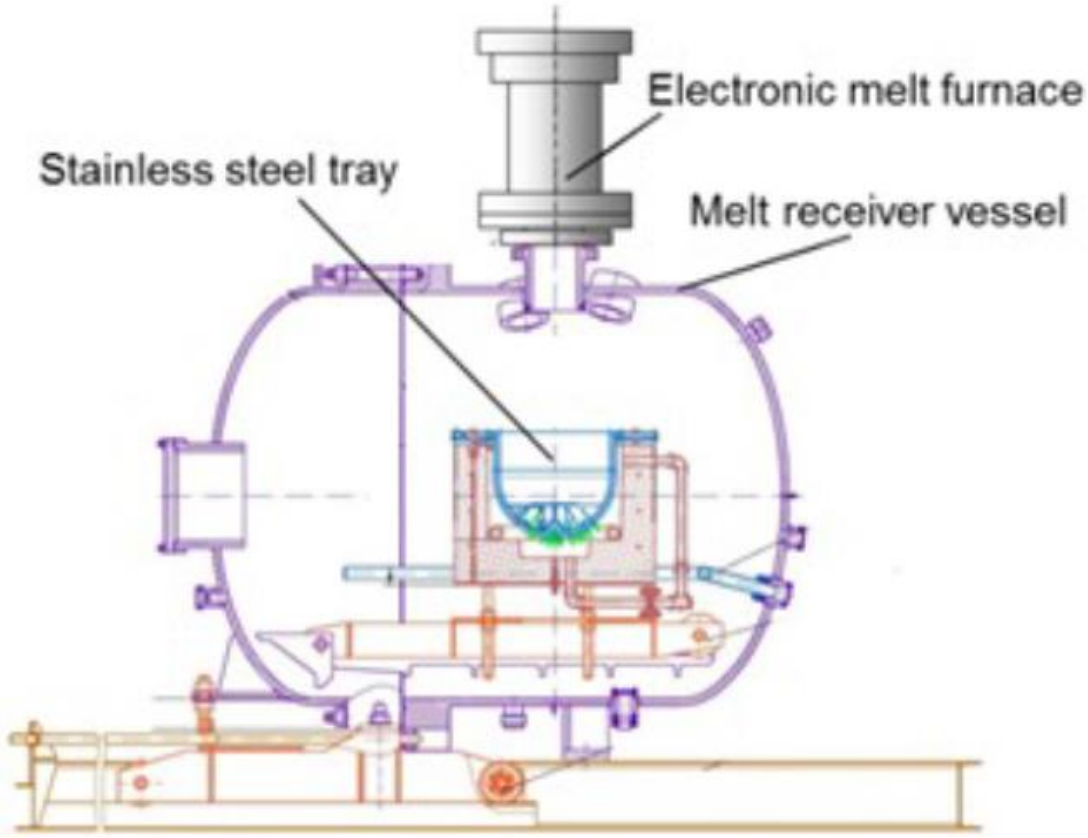

Figure 1.14 LAVA-B device schematic used to simulate the reactor core cooling process.

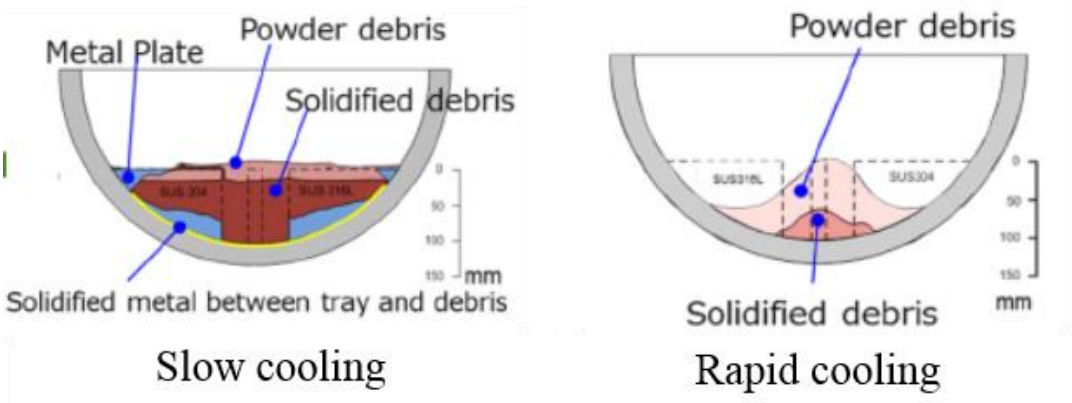

Figure 1.15 Schematic of the cooling process result simulated by LAVA-B.

Figure 1.16 shows the appearance example of powder debris formed through rapid cooling. The powder debris formed from rapid cooling were classified by its size, and its distribution plot is shown in figure 1.17. From this data, it can be concluded that the average diameter of retrievable nuclear debris would be around 5~10 mm.

Figure 1.16 Appearance of powder debris formed through rapid cooling.

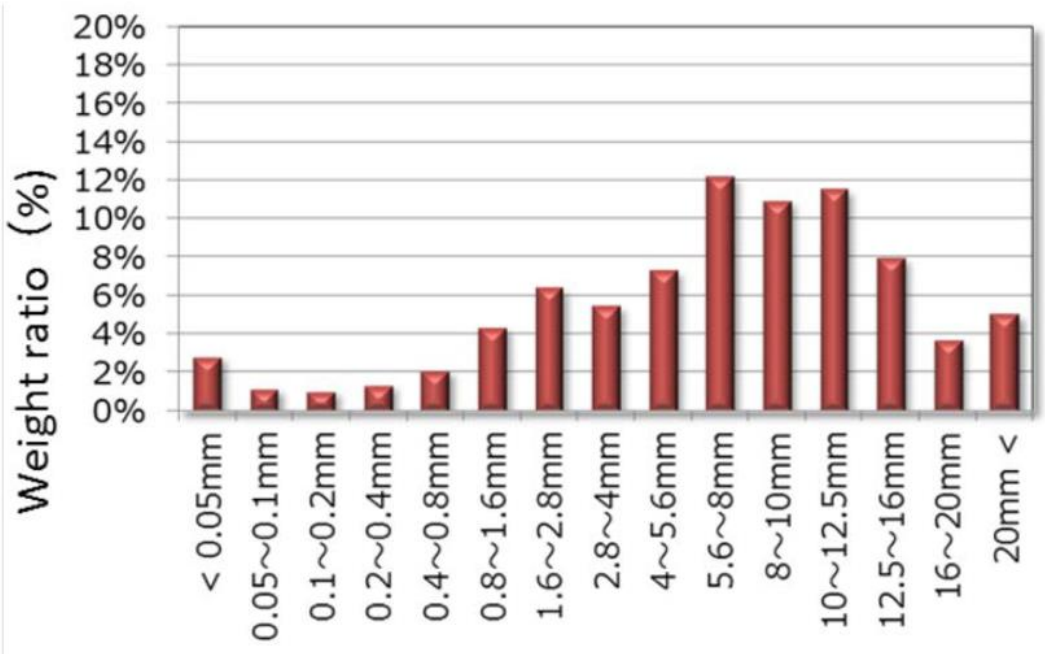

Figure 1.17 Particle size distribution of powder debris.

All kind of nuclear debris, including particle or rock-like debris, are object for nuclear security and safeguards as well as criticality safety, therefore it needs to be secured and evaluated. In the Fukushima Daiichi nuclear reactor decommissioning project, the most important elements to be retrieved for safeguards subject first are uranium and plutonium.

1.1.4 Plan for the nuclear debris removal from Fukushima Daiichi reactor PCV

As explained so far, it can be understood that the nuclear fuel debris removal and further quantitative evaluation of them are necessary as a part of the Fukushima Daiichi nuclear reactor decommissioning project. To provide critical and reliable information for nuclear debris removal planning, a preliminary research on the basic condition of the area containing the nuclear debris is necessary. Following the timeline of the nuclear debris extraction project scheduled by NDF, several methods by various research facilities in order to carry the process effectively and efficiently.

One of the proposed methods for this purpose is the mapping of the nuclear debris activity. Mapping of the nuclear debris activity is a project collaboration between JAEA, The University of Tokyo, The University of Sheffield, and The University of Bristol. The objective of this project is to do a mapping of nuclear debris activity and its uranium and/or plutonium contents using Kriging method around the reactor core area, especially at the spots where the nuclear debris removal activity will be performed in the future.

Kriging is an interpolation method for spatially discrete data developed in the field of mining technology, in which applicated to nuclear field as well such as for the spatial dose rate distribution of decommissioned facility, and so on. In this method, sampling is performed to find the concentration of a certain physical and/or chemical index A (C_A) in a debris lump. And then Kriging is use to interpolate the sampling points. There are two kinds of Kriging method:

- Ordinary Kriging: Estimation of the distribution of C_A with only the information of index A sampling points.
- Kriging with External Drift (KED): There would be a case where index B is correlated with index A of interest. For better accuracy of C_A, index B is combined with index A as the supplemental information of concentration of index B (C_B). From there, a more probable distribution of C_A can be obtained.

The elements data for mapping with Kriging method is obtained through on-site nuclear debris screening system, and at the same time, research on the analysis of nuclear debris structure as well as fabrication of model nuclear debris for more realistic result is being developed. Diagram for this project is shown in figure 1.18. The background and motivation behind the chosen methods for nuclear debris on-site screening system will be explained in the next section.

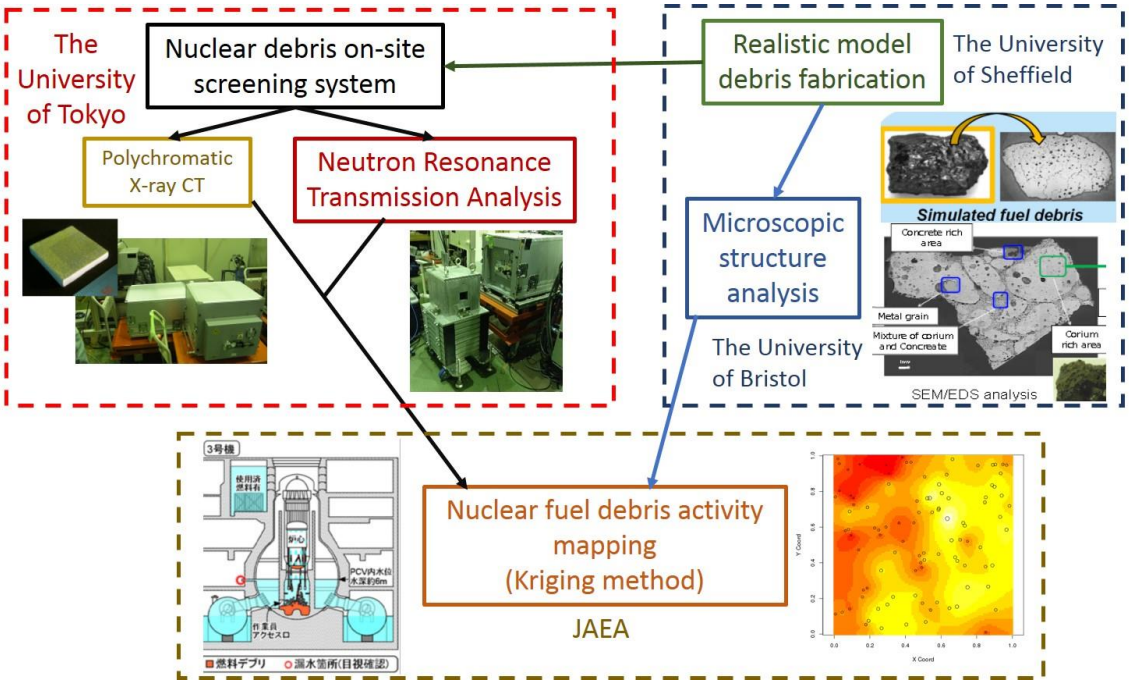

Figure 1.18 Diagram of the nuclear debris evaluation and mapping for the safety of debris removal.

1.1.5 Nuclear debris composition identification methods

In order to provide a necessary data for nuclear debris activity mapping, an on-site screening system for nuclear debris is needed for more efficient decommissioning activity, rather than taking the debris sample to the nuclear facility for inspection. The on-site screening system will only perform qualitative analysis instead of quantitative, but it would still increase the efficiency and is enough for the purpose of supplying data for nuclear debris activity mapping.

As mentioned in the previous paragraphs, the necessary information for application of this mapping method is the distribution of uranium and plutonium content in fuel debris lumps. Therefore, for this purpose, an appropriate method of analyzing the debris and determining its composition on-site is required. Some established methods on nuclear debris analysis such as laser-induced breakdown spectroscopy (LIBS) can be used on-site nuclear reactor core[10]. However, as the analyzed sample would be instantaneously evaporated to induce light-emitting plasma, it would be difficult to obtain the weight information of the debris as well. On the other hand, induction coupling plasma mass spectrometer (ICP-MS) method that has been established by IRID to analyze Fukushima

Daiichi nuclear debris[11] has minimum destructive effect to the sample, but it is not available for on-site use.

The proposal of this research is to realize an on-site non-destructive analysis method for nuclear debris at 1F by making use of the mobile, compact-sized, high-frequency X-band electron linac to construct a linac-based X-ray and neutron source. The diagram in figure 1.19 (debris sample retrieval route by robot in the reactor pressure vessel from source [12]) shows the flow of on-site screening of nuclear debris activity. This system utilizes two kinds of measurement technologies that complement each other.

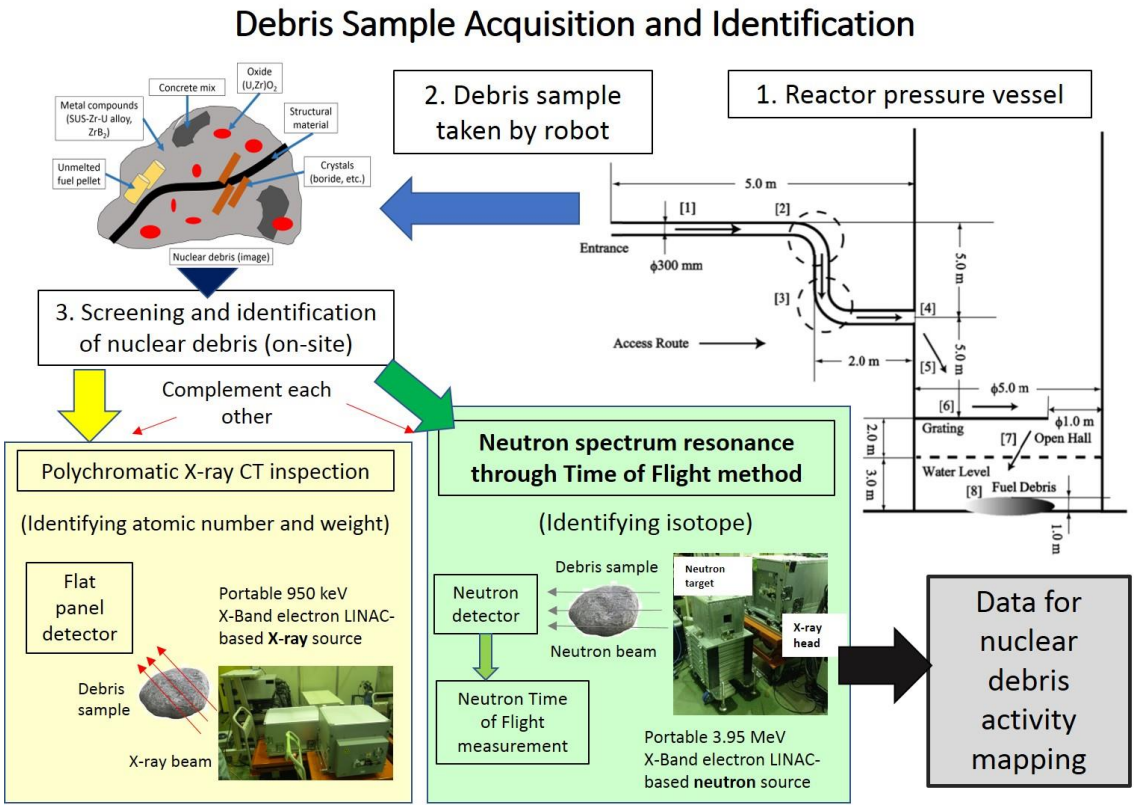

Figure 1.19 Schematic of on-site nuclear debris screening activity before detailed analysis at nuclear research facilities.

In regards to the inspection methods incorporated for on-site screening system, X-ray CT will be the one to provide quantitative data of nuclear debris size and imaging necessary for nuclear debris activity data. Polychromatic X-ray CT method was chosen as it has very good capability of identifying material with large gap on their atomic number (Z)[13]. It is suitable for detecting uranium and plutonium as both have the highest Z number among other materials contained in the nuclear debris.

Even so, it is difficult to set a proper thresholding in order to get accurate identification of materials with close Z number[14], which would be the downside of this method in clear differentiation between uranium and plutonium. The two radioactive elements have very different microscopic cross-section value where plutonium microscopic cross-section is 200 times larger than uranium microscopic cross-section. This characteristic would make plutonium to be more reactive and prone to reach critical condition faster. Therefore, it is necessary to be able to distinguish between uranium and plutonium when handling the screening and analysis of nuclear debris' contents.

For this purpose, another nuclear debris screening method which can determine the existence of uranium and plutonium with higher accuracy to complement the X-ray CT imaging result is needed. Local nuclear waste facility Ningyo-Toge has established several techniques on uranium and plutonium identification in spent nuclear fuel such as fast neutron direct interrogation and gamma-ray to determine enrichment[15]. But these methods are mainly applicated to uniform, large quantity nuclear waste drums, aside from the measurement equipment being heavy and stationary. Therefore, it would be unsuitable for the purpose of this research, as its approach is the on-site screening. Measurement target are the smaller, mixed-elements nuclear debris just to provide a rough estimation of the contents.

One of other practical methods for identifying the mixed composition of a nuclear debris sample is via neutron resonance transmission analysis (NRTA). In NRTA, the neutron energy is measured via a neutron time-of-flight (TOF) method using a pulsed neutron source, which enables the specification of the neutron energy to be absorbed by the corresponding nuclide in the sample. NRTA uses each isotopes' unique neutron energy absorption value as an indicator of a material's compositions[16], and would be a great complement for polychromatic X-ray CT since it has high accuracy to the microscopic level on isotope identification. By integrating NRTA in the on-site nuclear debris screening system, we can accurately confirm the material composition of a nuclear debris contents, specifically the content of uranium and plutonium, from the combination of both methods. Figure 1.20 shows the flow of the nuclear debris screening with this combined detection system.

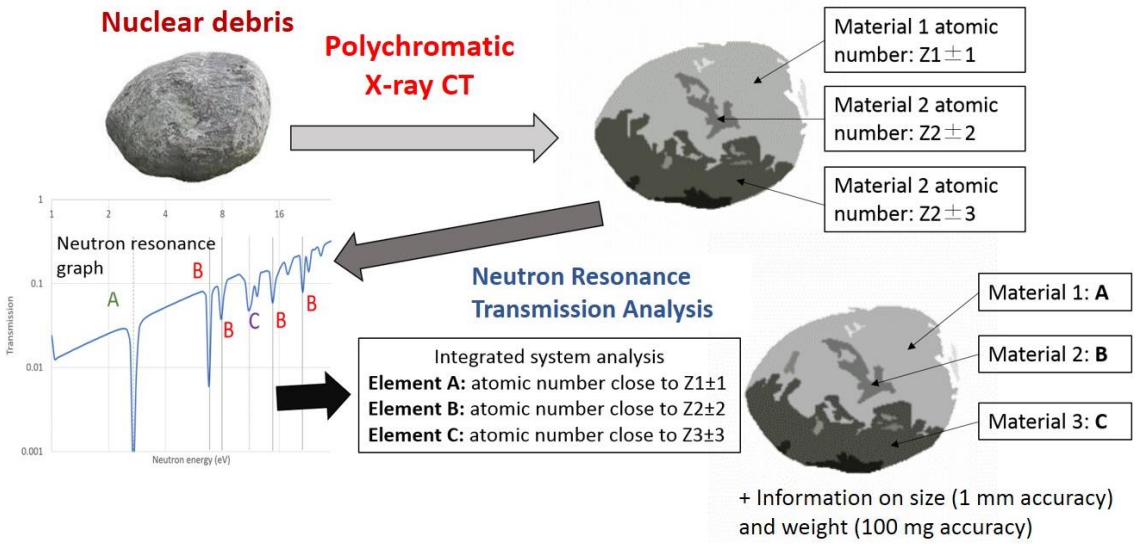

Figure 1.20 Schematic of on-site nuclear debris screening activity flow according to combined detection system using polychromatic X-ray CT and NRTA.

The essential measurement activity in NRTA is neutron TOF measurement, which will be explained in further details in the next section, followed by explanations about NRTA mechanism as well.

1.1.6 Neutron time-of-flight measurement method

According to the de Broglie equation that relates the wavelength (λ) of a neutron to its momentum (*mv*), velocity (*v*) of the neutron is inversely proportional to its wavelength. This relation in shown in the equation (1).

$$\lambda = h/mv \tag{1}$$

Where h is Planck's constant (h = 6.626×10^{-34} Js) and m is the mass of neutron (m = 1.675×10^{-27} kg).

Neutron's velocity itself is very fast, but times scale of nanoseconds to microseconds can be readily measured with modern electronics these days. This is the principal concept of neutron TOF method, a way to measure neutron energy over fixed distance through calculation of neutron detection time difference (neutron's flight time). If the start time

of the neutron is fixed, the rest is only to measure is the arrival time at its destination, for example in the neutron detector. By calculating neutron's flight time over a fixed path length, the neutron's velocity (and consequently its wavelength) can be measured. Through the relation between the neutron's velocity and its kinetic energy, a continuous neutron energy spectrum of a neutron source can be obtained through this method. Figure 1.21 shows the schematic of the neutron TOF measurement method.

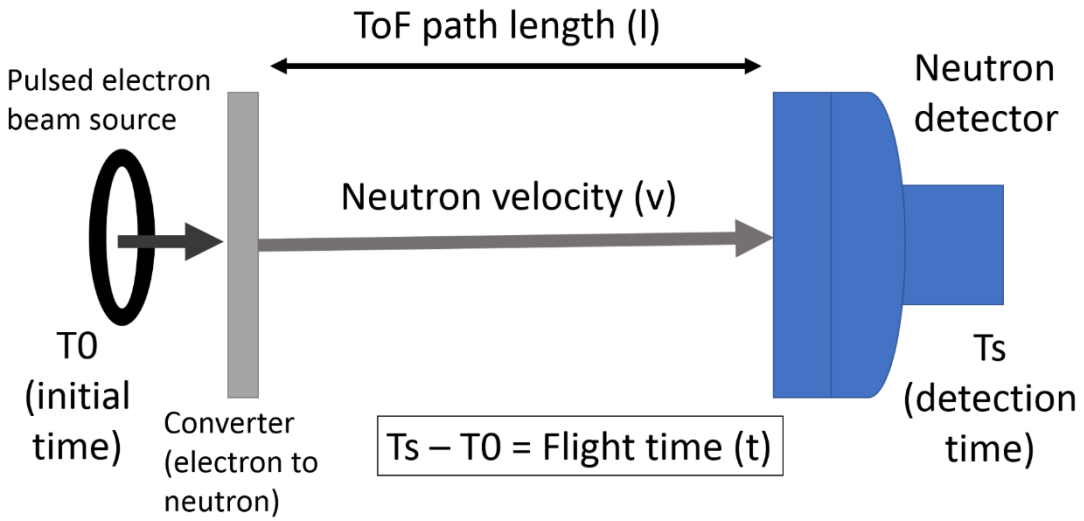

Figure 1.21 Schematic of neutron time-of-flight measurement method.

Neutron spectroscopy applying the TOF technique relies on a measurement of the time t that a neutron needs to travel a given distance *l*. The time *t* and distance *l* are related to the velocity *v* and kinetic energy E of the neutron as shown in equation (2) and (3), with *c* as the speed of light.

Velocity of neutron:

$$\nu = \frac{l}{t} \tag{2}$$

Energy of neutron:

$$E = mc^2(\gamma - 1) \tag{3}$$

Where γ (Lorentz factor) is:

$$\gamma = \frac{1}{\sqrt{1-(v/c^2)}} \tag{4}$$

Experimentally a TOF (t_m) is derived from the difference between a start (T_0) and stop (T_S) signal:

$$t_m = (T_S - T_0) + t_0 \tag{5}$$

Where t_0 is a time-offset, which mostly due to a difference in cable lengths. For scintillator detectors the off-set can be deduced accurately from a measurement of the TOF of the γ -ray flash produced in the target. For other detectors, e.g. solid state or gaseous neutron or charged particle detectors, the time-offset derived from the γ -ray flash might be biased due to the difference between the energy-loss process of a γ -ray and a charged particle and the time-offset is best derived from transmission peaks or resonance peaks of high energy resonances for which the resonance energies are accurately known. Equation (6) shows that the observed time-of-flight (t_m) is related to the time t that a neutron, leaving the target-moderator assembly with a velocity v[17].

$$t_m = t + t_t + t_d \tag{6}$$

In order to perform a TOF measurement, the neutron source needs to be pulsed in short well-defined intervals to be able to obtain a continuous neutron energy spectrum. Pulsed neutron source usually produced by using accelerator that can generate pulsed electron, which later converted to neutron through other nuclear reaction with specific material. Usually this kind of neutron source use high-energy accelerator that is stationed in nuclear research facility, but this research will introduce the usage of compact and mobile neutron source for neutron TOF measurement.

1.1.7 Neutron resonance transmission analysis

In common with gamma rays, neutrons carry no charge and therefore cannot interact in matter by means of the coulomb force, which dominates the energy loss mechanisms for charged particles and electrons. Neutron interaction is with a nucleus of the absorbing material and may result in neutron totally disappear and be replaced by one or more secondary radiations, or the energy or direction of the neutron is changed significantly. Neutrons can also travel through considerable distance inside matter without any type of interaction, thus making it to be totally invisible to a detector of common size.

In contrast to gamma rays, the secondary radiations resulting from neutron interactions are almost always heavy charged particles. These particles may be produced either as a result of neutron-induced nuclear reactions or the nuclei of the absorbing material itself, which have gained energy as a result of neutron collisions. For neutrons of a fixed energy, the probability per unit path length is constant for any of the interaction mechanisms. This probability is expressed in terms of the cross-section per nucleus for each type of interaction. The cross-section has units of area and has traditionally been measured in units of the barn (10^{-28} m^2). For example, each nuclear species will have an elastic scattering cross-section, a radiative capture cross-section, and so on, each of which will be a function of the neutron energy[18]. The neutron resonance transmission analysis (NRTA) is the method that use a nucleus' neutron total cross-section to identify a material.

NRTA is a non-destructive method which is based on well-established methodologies applied for neutron induced cross-section measurements in the resonance region[19]. It relies on the TOF technique, which is a standard technique for neutron resonance spectroscopy. NRTA is based on the analysis of characteristic peaks in a transmission spectrum resulting from a measurement of the attenuation of a neutron beam by the sample under investigation [16, 17]. These peaks are observed at TOF values that correspond to resonance energies. The quantity of interest in a transmission experiment is the fraction of the neutron beam traversing the sample without any interaction, expressed in the equation (7). The transmission is directly related to the total cross-section and the areal density of the nuclides present in the sample.

$$T_{exp} = \frac{C_{in}}{C_{out}} \tag{7}$$

Resonances appear at energies, which are specific for each nuclide. Position and amplitude of resonances can be used as fingerprints to identify and quantify nuclides, assuming that the total cross-sections of the materials present in the sample are known[17]. The said resonance peak can be observed and used to identify the isotopes contained in the sample material through neutron energy absorption data reference for specific isotopes from JENDL or other nuclear data library.

The picture shown in figure 1.18 and figure 1.19 are the example of isotope identification using NRTA method. The peaks marked by red dashed lines are the neutron energy value part with the highest total neutron cross-section. Nuclear data reference is then used for comparison with the neutron resonance transmission analysis result of a U_3O_8 sample. In the nuclear data reference of neutron total cross-section of ^{238}U and ^{235}U as shown by figure 1.22[20], the highest cross-section for neutron reaction happened at the neutron energy value of 8-40 eV. NRTA experiment result of an U_3O_8 sample at figure 1.23[21] shows that resonance peaks happened at the neutron energy range of 5-40 eV. These resonance peaks represent the isotopes contained in the sample, and it shows a good agreement with the neutron energy value for neutron reaction in the reference. It proves that NRTA is an effective multiple isotopes identification method with good accuracy for a sample containing mixed material, especially for the isotopes which neutron reaction energy value at resonance neutron area such as Uranium isotopes.

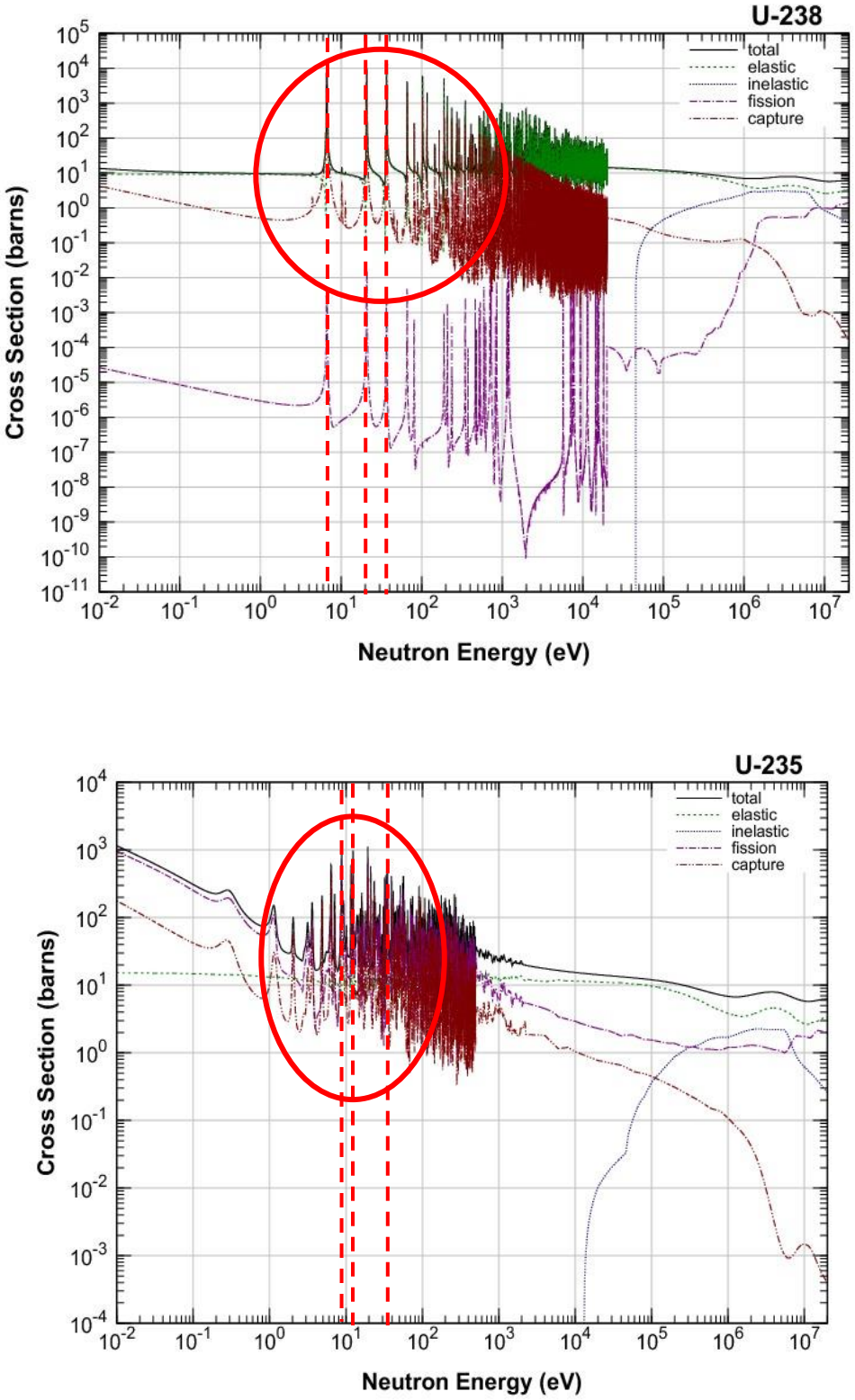

Figure 1.22 Neutron reaction energy spectrum for ^{238}U (top) and ^{235}U (bottom).

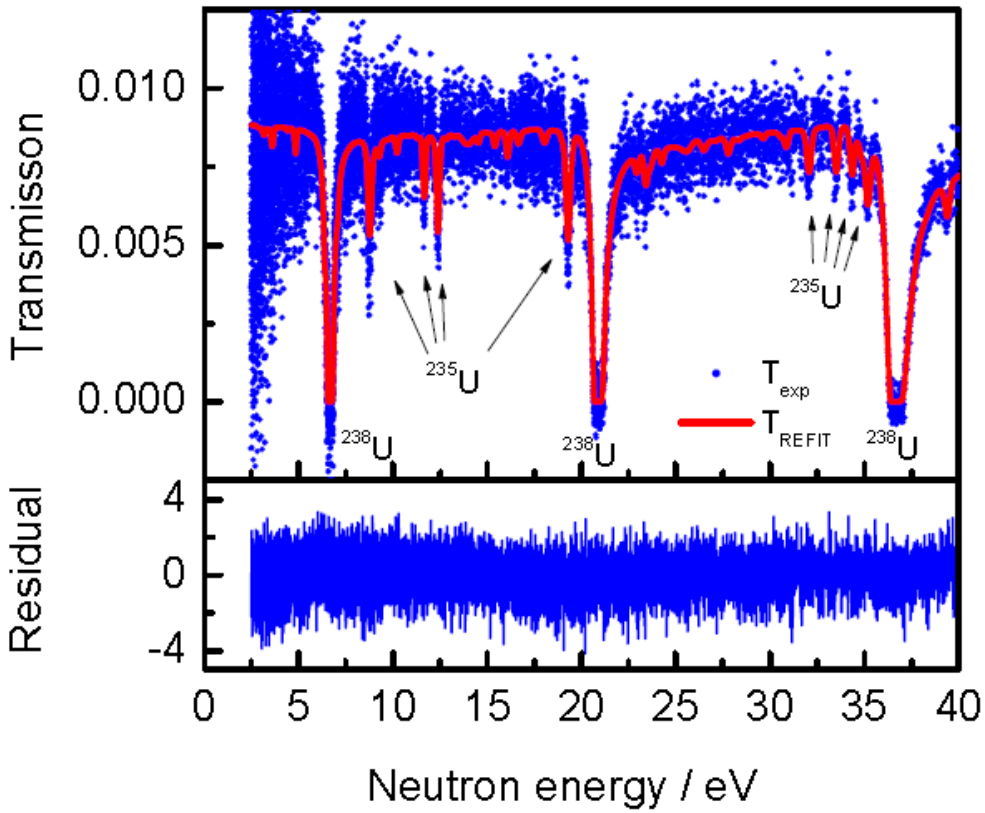

Figure 1.23 NRTA experiment result of a U_3O_8 sample performed at GELINA.

NRTA does not require any additional calibration measurements using reference samples that are representative for the material under investigation[18]. The accuracy of the results relies on the quality of the nuclear data, in particular, the total neutron cross-sections of the nuclides present in the sample. Since total cross-sections for neutron interactions are one of the most accurate nuclear data, NRTA can be considered as one of the most accurate absolute NDA methods for the characterization of materials.

As a reference regarding NRTA method to identify nuclear debris composition, a research on uranium and other minor actinides identification for Fukushima nuclear debris using NRTA has been conducted by the cooperation between Japan Atomic Energy Agency (JAEA) and Joint Research Center (JRC)[22]. Their main subject for identification is the rock-like and particle-like mixed-elements nuclear debris, which analysis is more complex and challenging due to their uncertainties in various aspects. They did an experiment using Geel Electron Linear Accelerator (GELINA) with 100 MeV energy and flight path of 10-12.5 meters. As the result, they have successfully identified each element contained in a mixed sample that represents nuclear debris. Based on this experience, NRTA was chosen as the complementary method for X-ray CT in the on-site nuclear debris screening system.

1.2 Pulsed neutron source

Neutron source generates radiation (neutron) from accelerated charged particles. Because alpha particles are the only heavy charged particles with low Z conveniently available from radioisotopes, reactions involving incident protons, deuterons, and so on must rely on artificially accelerated particles. Two of the most common reactions of this type used to produce neutrons are D-D (deuterium-deuterium) and D-T (deuterium-tritium), which reactions are explained below:

D-D reaction: ${}_1^2H + {}_1^2H \rightarrow {}_2^3He + {}_0^1n$ (Q-value = -1.666 MeV)

D-T reaction: ${}_1^2H + {}_1^3H \rightarrow {}_2^4He + {}_0^1n$ (Q-value = -2.226 MeV)

Because the coulomb barrier between the incident deuteron and the light target nucleus is relatively small, the deuterons need not be accelerated to a very high energy in order to create a significant neutron yield. These reactions are widely exploited in neutron generators in which deuterium ions are accelerated by a potential of about 100-300 kV. Because the incident particle energy is then small compared with the Q-value of either reaction, all the neutrons produced have about the same energy (near 3 MeV for the D-D reaction and 14 MeV for the D-T reaction). A 1 mA beam of deuterons will produce about 10^9 n/s from a thick deuterium target and about 10^{11} n/s from a tritium target.

A number of other charged-particle-induced reactions that involve either a negative Q-value or a target with higher atomic number are also applied to neutron generation. Some common examples are ^{9}Be(d, n), ^{7}Li(p, n), and ^{3}H(p, n). For these reactions, larger accelerators are required to produce the higher charged particle energies needed for useful neutron production, although there has been progress in reducing their size[17]. Some of the small-size neutron source will be introduced in the latter part of this section.

As mentioned in the previous section, in order to be able to perform neutron Time-of-flight measurement, the neutron source needs to be pulsed in short well-defined intervals, in other words, pulsed, to be able to obtain a continuous neutron energy spectrum. Usually this kind of pulsed neutron source use high-energy accelerator that is stationed in nuclear research facility.

Past research by Japan Atomic Energy Agency (JAEA) with Kyoto University Research Reactor Institute (KURRI) on pulsed neutron source, shows that time-delay of neutron generation from the injection of electron beam into the neutron target, in other words, neutron's pulse width, affects the energy resolution of the measurement as well. Figure 1.24 shows time distributions of pulsed neutron at the tally surface obtained by the Monte Carlo simulation. In order to mean time structure, an expected value of time-delay is defined as shown in equation (8).

$$\overline{\Delta t} = \frac{\sum_i P_i \Delta t_i}{\sum_i P_i} \tag{8}$$

Where Δt_i is time-delay of neutron passing through the tally surface from the injection of electron beam into the neutron target (in this case, tantalum). A P_i is probability distribution of Δt_i, which is obtained from the histograms shown in figure 1.20, respectively.

Energy resolution ($\Delta E/E$) is related to the time resolution ($\Delta t/t$), where t is flight time, expressed through equation (9).

$$\frac{\Delta E}{E} = -2\frac{\Delta t}{t} \tag{9}$$

The relation of the flight time and the neutron energy E (eV), is expressed in equation (10), where L is flight path (m).

$$\mathrm{t[\mu s]} = \frac{72.3L[m]}{\sqrt{E[eV]}} \tag{10}$$

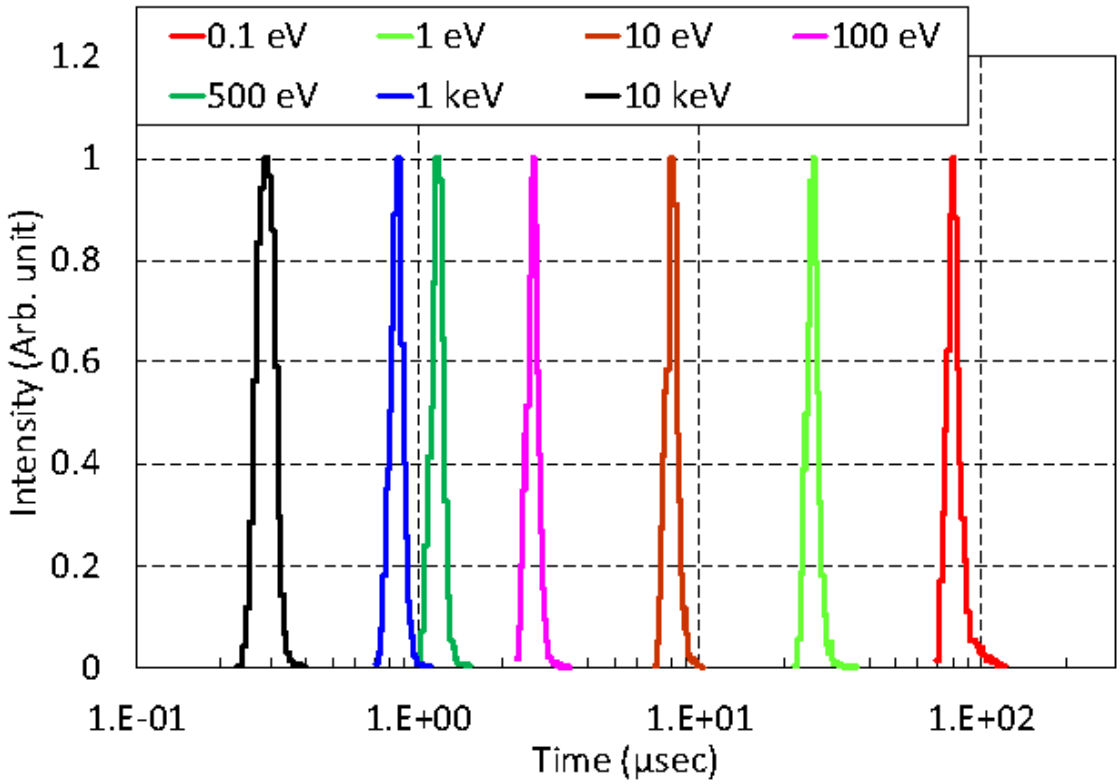

Figure 1.24 The time distributions of pulsed neutron at the tally surface from simulation.

The experiment on the uncertainties of measurements with different pulse widths performed with KURRI's neutron source with 10 meters TOF path shows the result pictured in figure 1.25. When measuring higher neutron energy above 10 eV, 4 μs electron beam pulse width doesn't show any resonance peak on the TOF spectrum. Longer pulse width increases the uncertainty of the measurement of neutron energy[23]. This means that in order to be able to detect the neutron absorption in the resonance neutron area (1-100 eV) efficiently, the pulse width of the neutron source needs to be as short as 500 ns.

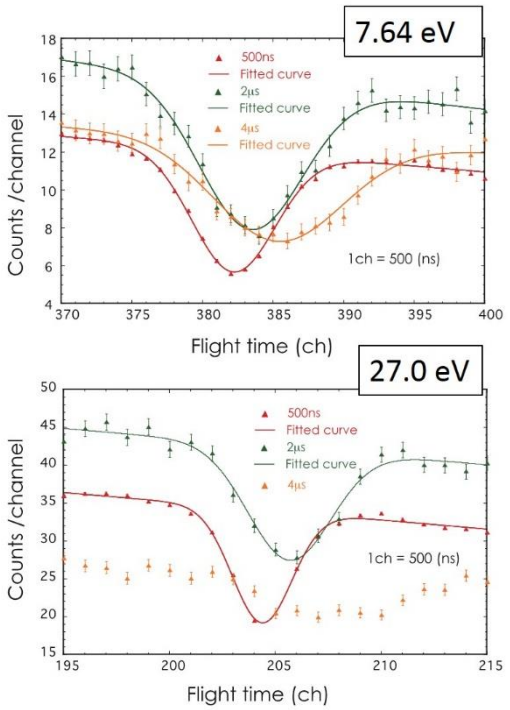

e-beam pulse width	Peak channel	FWHM
500ns	382.2±0.1	4.1±0.1
2μs	383.4±0.1	5.1±0.2
4μs	385.4±0.2	6.5±0.4

e-beam pulse width	Peak channel	FWHM
500ns	204.4±0.1	2.0±0.1
2μs	205.6±0.1	2.8±0.2
4μs	-	-

*peak does not appear at 4 μs pulse

Figure 1.25 Uncertainties of measurements with different pulse widths.

Several of the pulsed neutron source facilities established in Japan for the purpose of nuclear material analysis, as well as some of the compact neutron source, will be explained in this section.

1.2.1 Kyoto University Research Reactor Institute's neutron source

The electron linear accelerator (KURRI-LINAC), which photo is shown in figure 1.26, is one of the pulsed neutron source at Kyoto University Research Reactor Institute (KURRI), and is used as various types of particle beam source, i.e. electrons, neutrons, and photons. The electron beam is generated by a thermionic gun and accelerated to 46 MeV in two accelerator tubes by L-band (1.3 GHz) microwave. The pulse width is variable from 2 ns to 4 μs. Frequency is variable up to 300 Hz. The research region covers a wide field of nuclear data acquisition with the neutron TOF method and a lead slowing down spectrometer, isotope production by the (γ,n) (γ,p) reaction, low temperature electron irradiation, a photon activation analysis, and a spectroscopy with coherent THz radiation[24]. The layout of the linac is shown in figure 1.27.

Figure 1.26 Electron Linear Accelerator of KURRI.

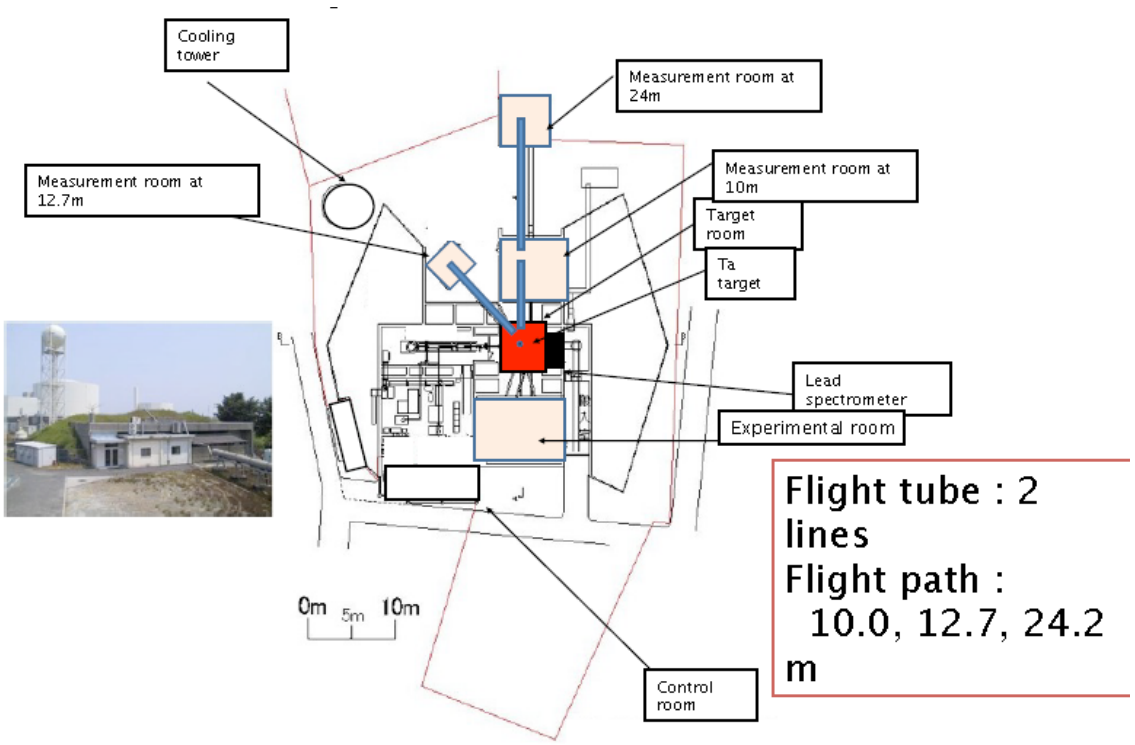

Figure 1.27 Layout of KURRI-LINAC.

KURRI-LINAC has the specifications of 30 MeV electron energy with frequency of 100 Hz and pulse width of 100 ns. The neutron target is tantalum with water moderator which photo is shown in figure 1.28, with neutron flux production around 8 x 10^{12} neutrons/second.

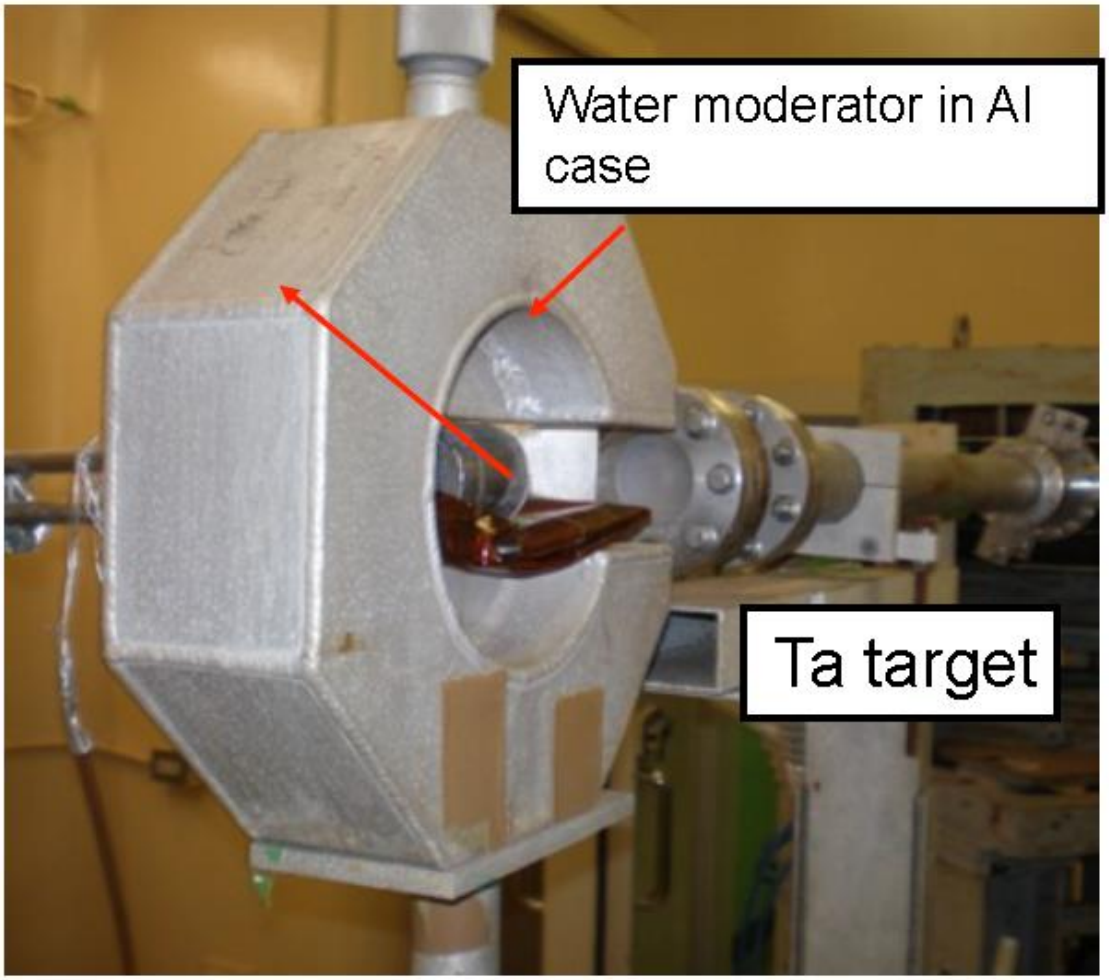

Figure 1.28 Tantalum neutron target and water moderator at KURRI-LINAC.

KURRI-LINAC also has 10, 12.7, and 24.2 meters TOF path for the nuclear data measurement purpose, with the neutron energy range of 0.005 eV to 40 MeV. It has been used for various measurements such as neutron capture cross-section, fission cross-section, and photo reaction cross-section mainly for minor actinides and long-lived fission products[25]. This neutron source is also a stationary type.

1.2.2 Hokkaido University Neutron Source

Hokkaido University Neutron Source (HUNS) is an accelerator-based neutron source, that use S-band RF type electron linac with the 50 Hz pulse repetition, maximum energy of 45 MeV and pulse width of 3 μs. It produces neutron through electron bremsstrahlung and photonuclear reaction with lead (Pb) as neutron target, plotite as neutron reflector and solid methane as moderator, where the high-energy evaporation neutrons slowdown from the MeV region to the meV region through it. The total yield of fast neutrons emitted from the target material is about 1.6×10^{12} n/s, where the cold neutron flux is 3.1 x 10^{3} n/cm^{2}/s. The picture of the neutron source is shown in figure 1.29[26], while the schematic is shown in figure 1.30[27].

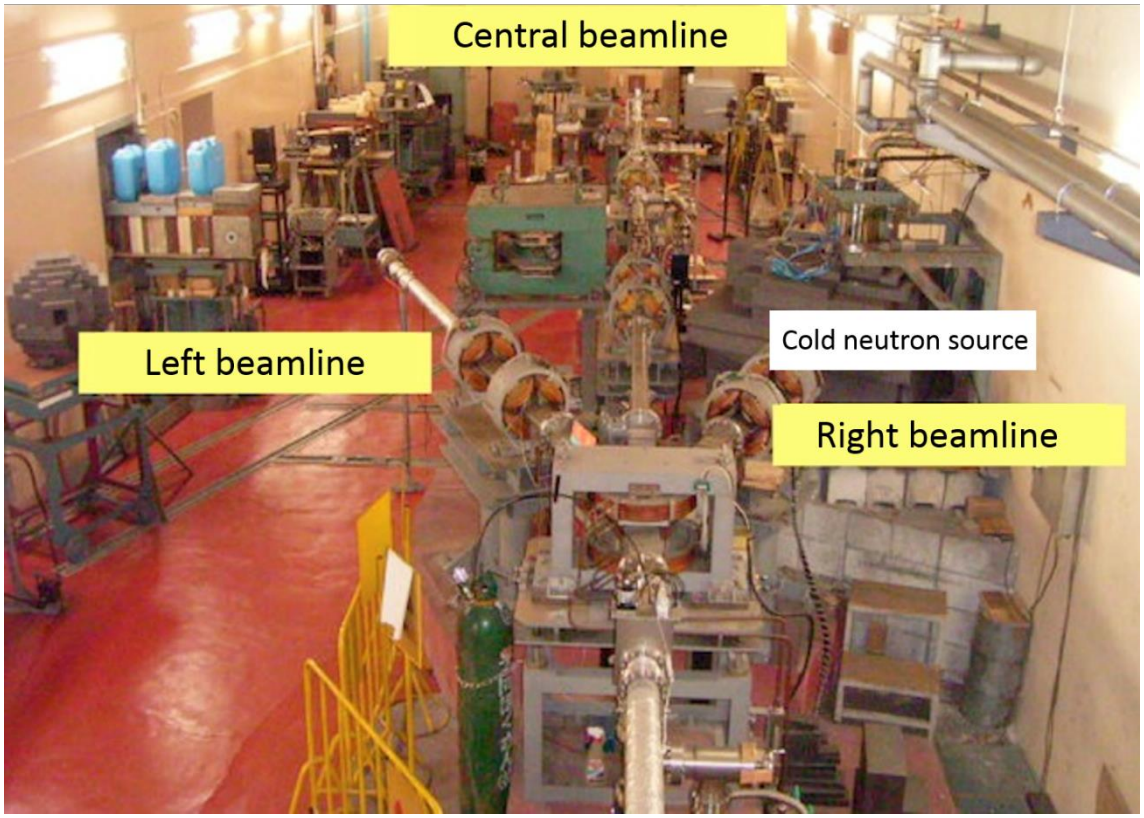

Figure 1.29 Photo of HUNS.

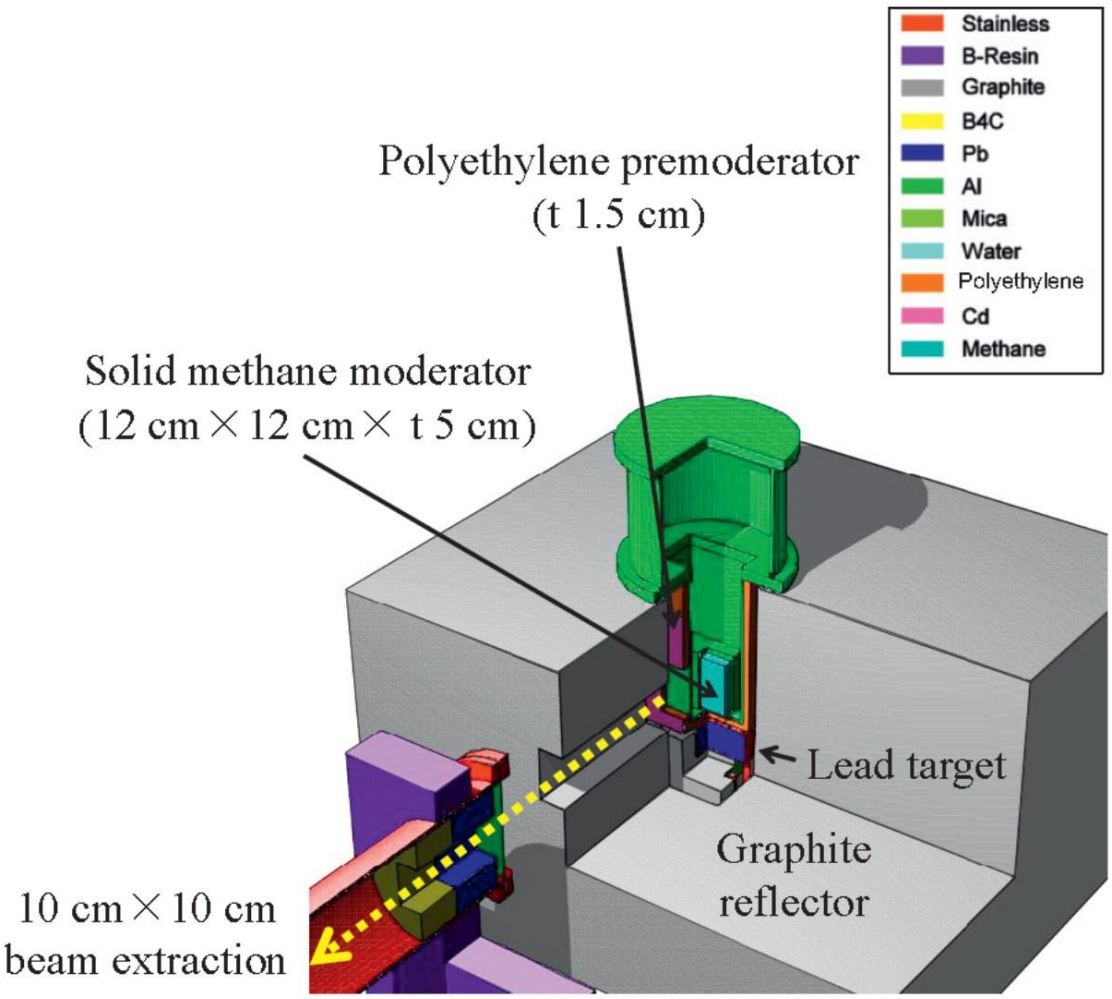

Figure 1.30 Schematic 3D view of HUNS.

Research at HUNS are mostly related to the neutron imaging, such as pulsed neutron imaging method and a new type of small angle neutron scattering method. Neutron imaging itself is one of the useful radiation transmission imaging that usually uses neutrons with a wide energy range, but pulsed neutron imaging is a unique method that can give the physical quantities[28]. By using the pulsed neutron source, transmission spectra at each pixel of a two-dimensional position sensitive detector coupled can be obtained with the TOF method. The spectra reflect structure of the neutron total cross section, in which there exists crystalloplotic information, elemental information, magnetic field information, etc[29].

1.2.3 JAEA D-T pulsed neutron source for integrated NDA system

Japan Atomic Energy Agency (JAEA), in cooperation with Joint Research Centre (JRC) has been working on a project related to measurement and detection of nuclear material for nuclear security and safeguards. One of the technology that they are currently establishing is the integrated detection and measurement system using active neutron non-destructive analysis (NDA) techniques for nuclear material. The system consists of Differential Die-away Analysis (DDA), Delayed Gamma-ray Spectroscopy (DGS), Prompt Gamma-ray Analysis (PGA) and Neutron Resonance Transmission Analysis (NRTA). All of these methods will perform their measurement using D-T pulsed neutron source. The picture of this integrated system is shown in figure 1.31.

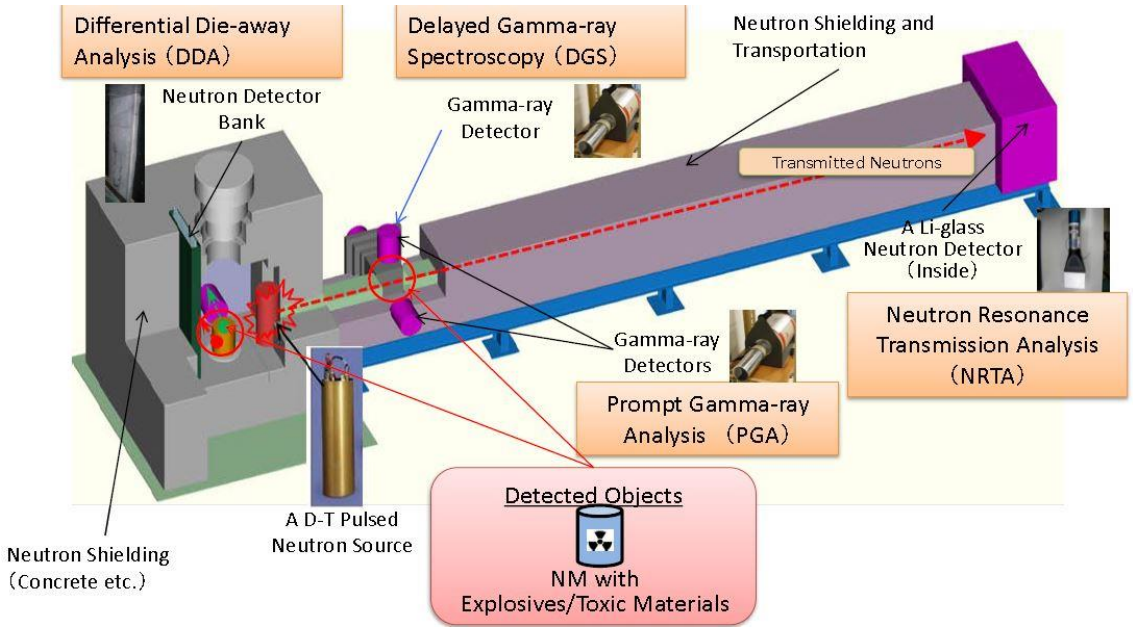

Figure 1.31 Integrated NDA system for nuclear material analysis developed by JAEA.

D-T neutron source in this system can produce neutron flux up to 10^{10} neutrons/second, with the pulse width of 100 μs. They are also using TOF method for the NRTA with neutron track of several meters distance[30]. However, this integrated system is stationary, therefore the sample for the object of the measurement needs to be carried to the measurement facility where this system resides.

1.2.4 Compact and mobile pulsed neutron source

Even if usually the kind of neutron sources used for NRTA are large-sized with high-energy particle linear accelerator as the trigger, the size of the neutron source can be reduced greatly and even possible for mobility if compact pulsed neutron source system were used instead. Compact neutron generators consisting of a sealed tube containing the ion source and target, together with a portable high-voltage generator. They produce smaller yields, but high enough for portable application. There are several types of commonly-used compact neutron source, and three of them will be explained in this section.

The first type of compact neutron source is D-D (deuterium-deuterium) neutron source. This is a type of small-size neutron source that generates neutron through D-D fusion reaction ($D + D \rightarrow n + {}^{3}He$). The generated neutron has pulse width of 100 μs, and it has the ability to penetrate further into objects, which makes D-D neutron source benefits for screening and imaging applications. This device doesn't use any radioactive material in its reaction, therefore it is safe to be carried and used outdoor. The image of D-D neutron source is shown in figure 1.32[31].

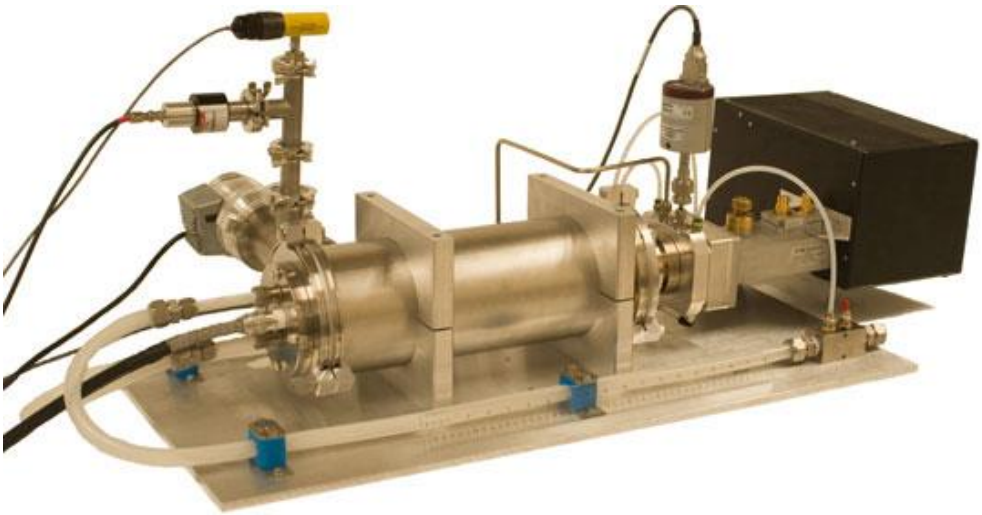

Figure 1.32 D-D (deuterium-deuterium) neutron source.

The second type of compact neutron source is D-T (deuterium-tritium) pulsed neutron source. It has the similar principle to D-D neutron source as well as generates the same pulse width, but the difference is that it produces neutron from fusion reaction between deuterium and tritium. This type of neutron source can produce higher neutron energy that is 100 times more efficient than D-D reaction with less power consumption.

However, as its name implies, D-T neutron source use tritium which is a radioactive material, and it will need to go through more process of local regulation of radioactive substance for mobile and outdoor use. The image of D-T neutron source is shown in figure 1.33[32].

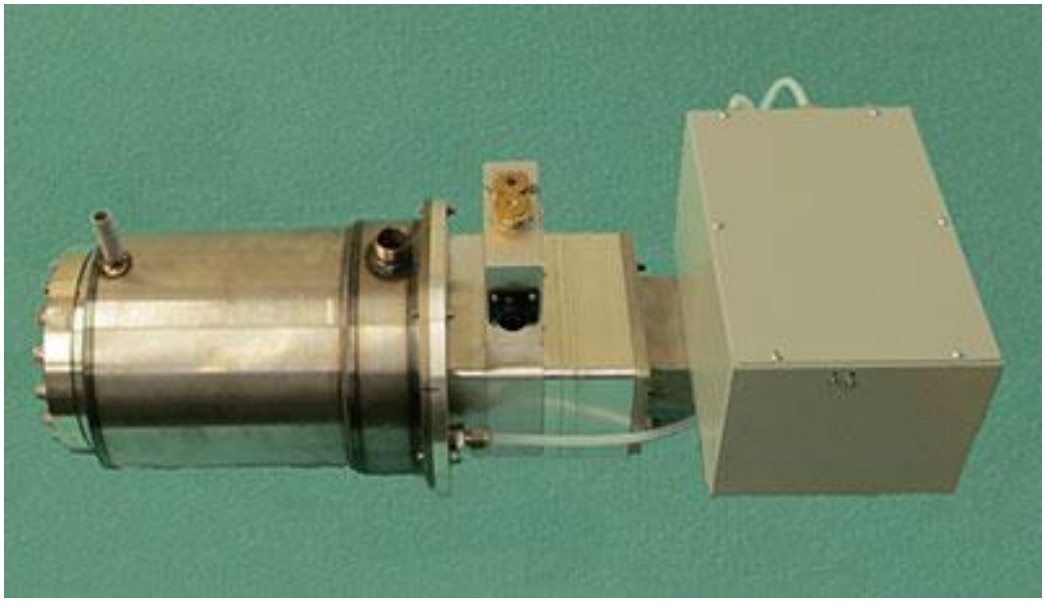

Figure 1.33 D-T (deuterium-tritium) pulsed neutron source (portable).

The last type of the compact neutron source explained in this section is the portable electron linac-based neutron source. This neutron source uses photonuclear reaction from Beryllium and X-ray source, generated from X-band electron linear accelerator (linac) with electron and photon converter of Tungsten and Beryllium target. There is no highly-radioactive material used in this system, and it has high portability and compactness for a neutron TOF measurement system.

Even though usually higher electron energies are required to produce acceptable neutron fluxes, it can be achieved by lower energy values as well. Past research on low energy linac-based neutron source was developed by an Italian research group through the utilization of low-energy electron linac of 5 MeV[33]. To compensate with this, they are using photoneutron converter material with low energy threshold. This way, even when irradiated by low energy electron linac and X-ray source, an adequate neutron flux can be generated by the neutron target. In this particular research, the low energy threshold materials chosen as neutron target are beryllium (1.66 MeV) and deuterium (2.2 MeV). By using 5 MeV electron linac and neutron target beryllium block with the size of $14 \times 28 \times 10$ cm^3, a neutron source with neutron flux of 8.48×10^7 $n/s/cm^2/mA$ can be realized. Figure 1.34 shows the schematic of this 5 MeV neutron source.

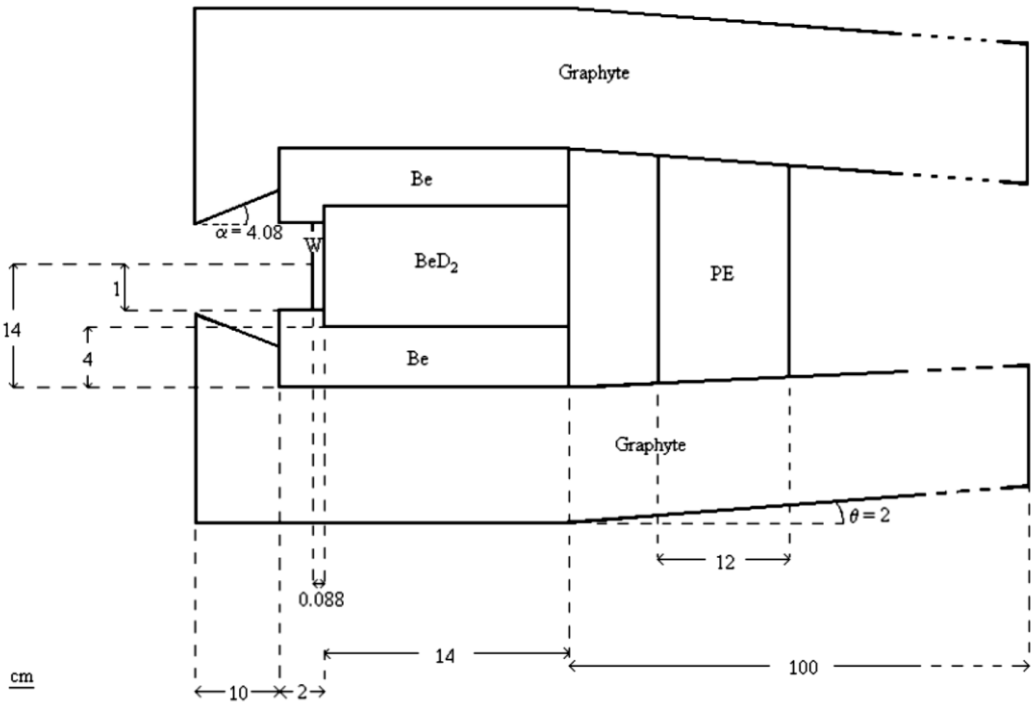

Figure 1.34 Schematic of 5 MeV electron linac-based neutron source using BeD_2 neutron target.

Using this research as reference, a compact and portable pulsed neutron source concept is developed as the neutron generator necessary for on-site NRTA. This neutron source uses beryllium block as the neutron target with lead collimator and boron polyethylene shielding. The image of portable electron linac-based neutron source is shown in figure 1.35. Details of this neutron source will be explained further in the next chapter.

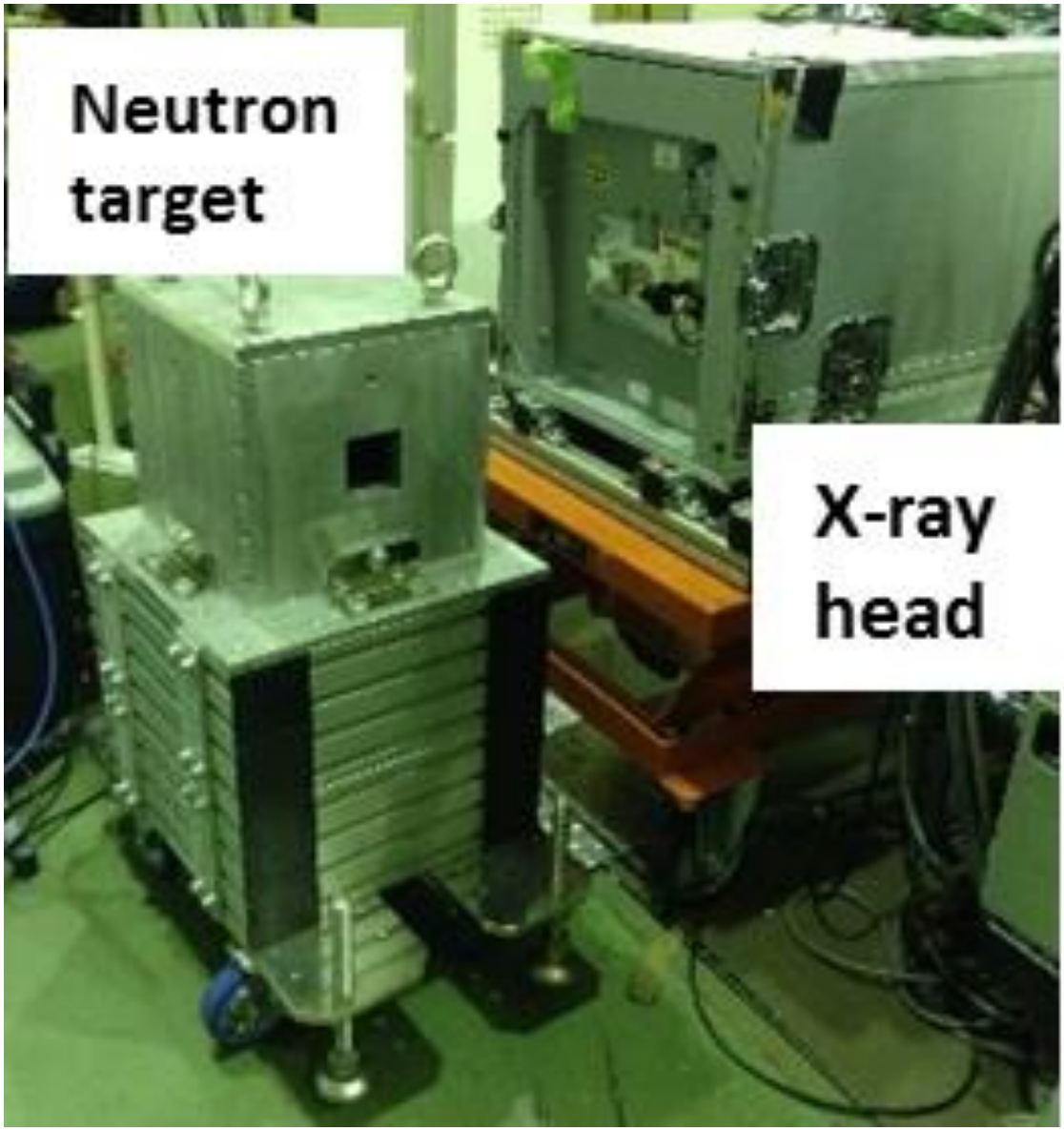

Figure 1.35 Portable electron linac-based neutron source.

The most important feature is that it produces the shortest neutron pulse among the D-D and D-T neutron source mentioned previously, which is 500 ns. For the purpose of measuring elements with higher neutron absorption energy, a short neutron pulse in the nanoseconds range is needed to obtain better resolution of the resonance peak. Therefore, X-band electron linac-based neutron source would be the most appropriate choice to be used in the on-site screening activity through neutron TOF method.

1.3 Research objective -Short-distance neutron time-of-flight concept-

Based on the explanations on the neutron source and method to identify nuclear material in the previous sections, it can be understood that in order to perform an effective and efficient Fukushima Daiichi nuclear reactor decommissioning, especially on debris removal activity, a nuclear debris activity mapping is necessary for making a reliable debris removal plan. From the project urgency, the first priority is to identify the uranium and plutonium content inside the nuclear fuel debris. To achieve this, a high-accuracy isotope detection method called NRTA is needed. As the current available neutron source capable to perform NRTA are all the stationary type at relatively far nuclear facilities from Fukushima Daiichi, the need for a mobile pulsed neutron source to increase the efficiency of the mapping project activity arise.

Therefore, the focus of this research is to develop a short-distance neutron TOF measurement system and NRTA that is capable to identify isotopes of uranium and plutonium using a mobile and compact pulsed neutron source. The diagram of this research objective is shown in figure 1.36. The novelty of this research will be the optimization of small neutron target for compact neutron source, and the short-distance NRTA able to identify uranium and plutonium isotopes (with limitation to ^{238}U, ^{235}U, ^{239}Pu, ^{240}Pu and ^{242}Pu which reasons will be explained in the further chapters).

The short distance is the most necessary feature since the total of the system should be compact and mobile for on-site use, particularly around the Fukushima Daiichi nuclear reactor area. Approach used by means to achieve this objective is through the utilization of low-energy electron linac-based neutron source as the pulsed neutron source necessary for neutron TOF measurement.

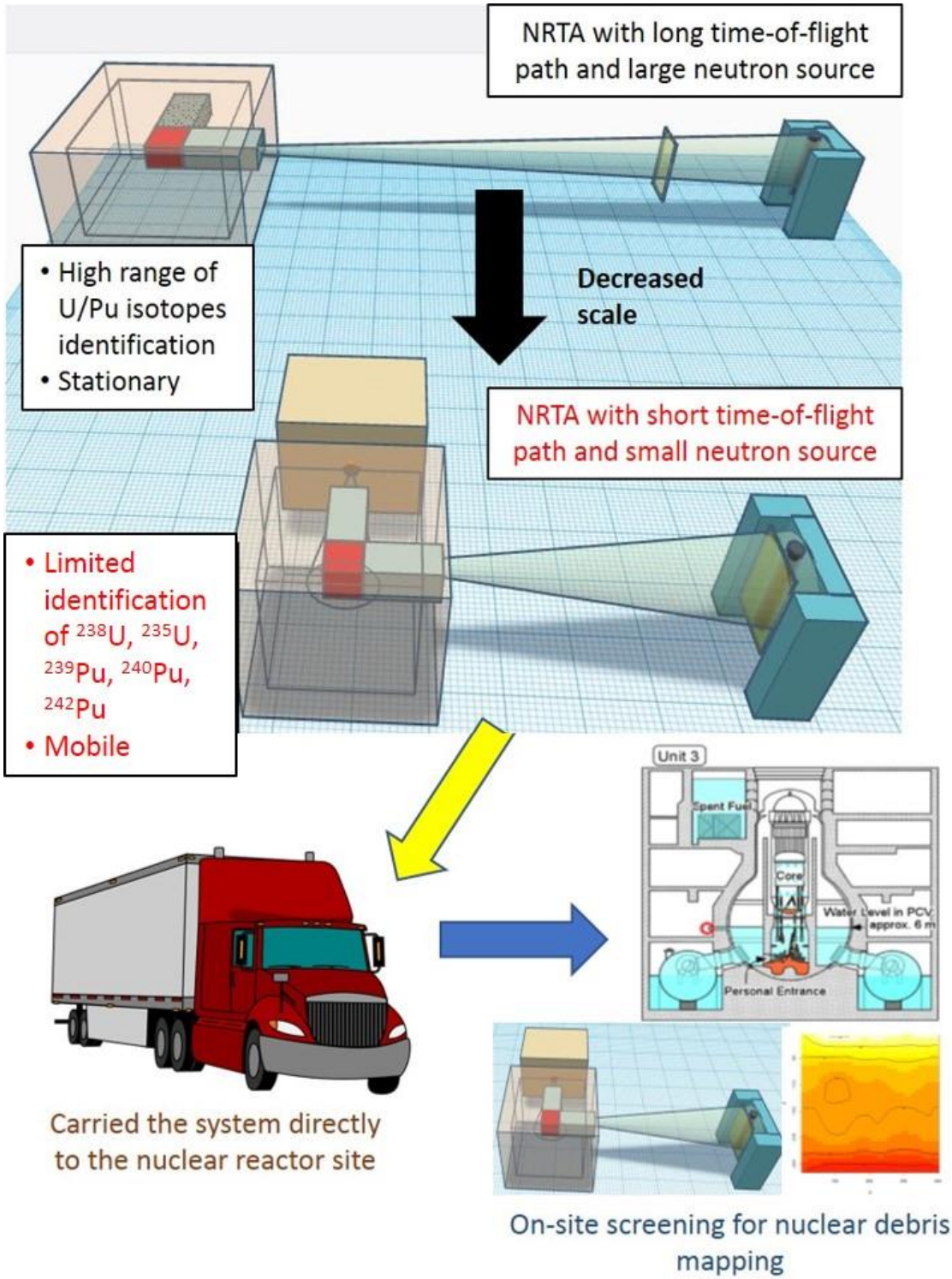

Figure 1.36 Diagram of the short-distance TOF concept for research objective.

2. X-band electron linac-based compact neutron source

Based on the explanation about various kind of neutron source and their advantages in the previous section, the neutron source used in this research will be the compact neutron source with X-band type accelerator as the trigger for the neutron generation reaction. This section will explain more about the mechanism of the said X-band electron linac-based neutron source.

2.1 X-band electron linac

Electrons can be accelerated with resonance in an almost linear orbit by a radio frequency (RF) electric field. The principle of operation for linear accelerators is to accelerate electrons through a waveguide by the use of alternating microwave fields. Two basic waveguide designs exist, which are standing wave and traveling wave. Waveguide length is a function of the maximum acceleration energy, in which the longer waveguide gives higher energy, and the frequency of the microwave field. The most common frequency for gantry-based linear accelerators is 2.998 GHz (S-band), but shorter waveguides are possible at 9.3 GHz (X-band) that produce megavoltage energies above 6 MeV[34].

X-band is a type of linear accelerator that has smaller size than S-band or C-band but compensates it with having higher RF frequencies which resulted in shorter pulse compared to the other two. In result, it is also has higher portability. Accelerating structures of S-band (2.856GHz), C-band (5.712GHz), and X-band (9.3GHz) linac and their usage in cancer therapy systems are shown in figure 2.1. [35] Recently, X-band linac is adopted such a backup for international linear collider, which is CLIC by CERN, and FEL by Elettra, Syncrotrone-Trieste and Compton scattering X-ray system for nuclear physics in ELI (Extreme Light Infrastructure) [36].

Another type of X-band linac is 30 MeV linac with 11 GHz operating frequency and input power of 5 MW. This type of linac, while not a portable type, is still relatively compact for its high energy capacity. The picture of the 30 MeV linac at Tokai Campus of The University of Tokyo can be seen in figure 2.2.

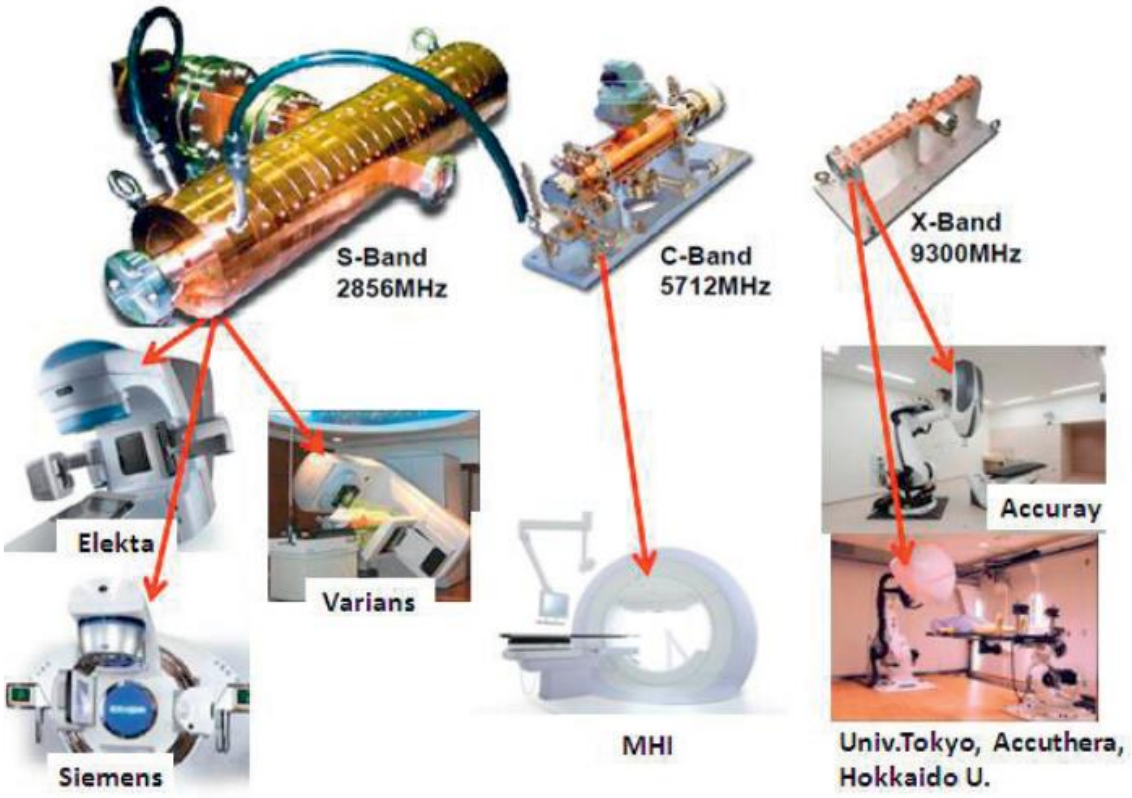

Figure 2.1 S-band, C-band, and X-band linear accelerator accelerating structures and their use for cancer therapy systems.

Figure 2.2 30 MeV linac at Tokai Campus of The University of Tokyo.

From the past research, the 950 KeV X-band electron linac with tungsten converter to produce Bremsstrahlung X-ray has been successfully utilized for on-site non-destructive infrastructure inspection[37]. The 3.95 MeV linac is another variation of X-band electron linac which has flexible waveguide connecting magnetron to X-ray source part, for the purpose of on-site use in which X-ray source part can be adjusted to the need of the measurement. This linac system consists of a 62-kg X-ray head (with additional target collimator of 80 kg), 62-kg of an RF power source, and other utility box which weights 116 kg. Parameters of 3.95 MeV X-band used in the experiment in this research is listed in the table 2.1[38].

Table 2.1 Parameters of the 3.95 MeV X-band electron linac-based neutron source.

Operating frequency	9.3 GHz
RF source	Magnetron
Input RF power	930 kW
Length of acceleration tube	50 cm
Form of acceleration tube	Side coupled structure
Accelerating cell	Half 1+full 20
Number Cells coupling	3%
Filling time	0.23μs
Shunt impedance	110-130MΩ/m (Regular part)
Focusing fashion	RF focusing
Voltage of electron gun	20 KV
Electron gun type	Triode
Electron beam size	5 mm
Beam energy	3.95 MeV
Beam current	80 mA
Pulse width	2.5 μs
Pulse frequency	220 pulses/s
Tungsten target size (ø x thickness)	5 x 0.5 mm
Neutron intensity (calculation)	3.86×10^7 n/ s

2.2 Conversion to compact neutron source

If an X-band compact electron linac can be generate pulsed accelerated electron, then theoretically it should be able to generate pulsed neutron as well just like the neutron source in larger nuclear facilities, through the use of some converters. In 3.95 MeV X-band electron linac's case, these converters would be electron-to-bremsstrahlung X-ray conversion and X-ray-to-neutron. The picture of the conversion process for the 3.95 MeV X-band electron linac-based neutron source that is being used in this research is shown in figure 2.3.

For the electron-to-bremsstrahlung X-ray part, the requirement for photon converter is material that can produce bremsstrahlung X-ray when by accelerated electrons, which in this case, the chosen material would be tungsten. As for neutron converter, it should have low threshold energy to be able to produce neutron through photonuclear reaction from low-energy X-ray. In this research, beryllium is used since its threshold photonuclear energy is only 1.67 MeV, which means neutron can be produced through exposure of Beryllium with 3.95 MeV X-ray. Further explanation about the theory on the beam converter materials will be explained in this section.

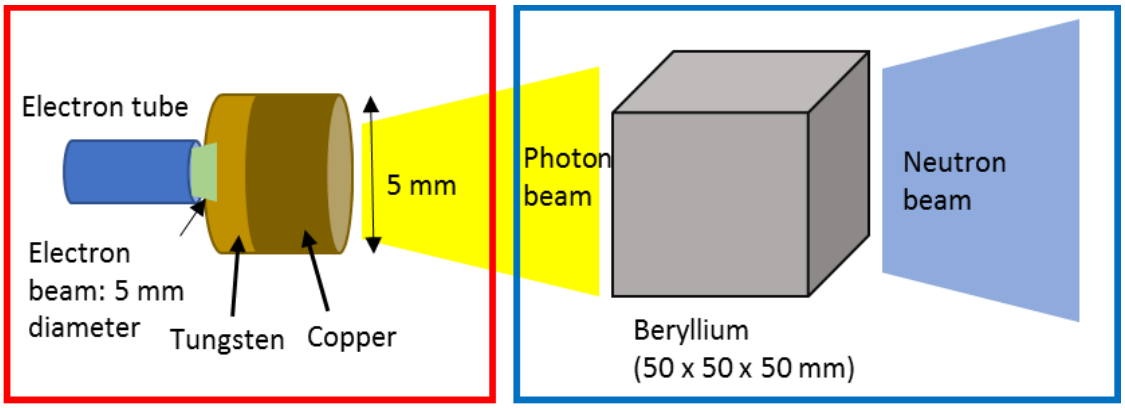

Figure 2.3 Principle of the pulsed neutron generation in the electron linac-based neutron source.

2.2.1 Theory of Bremsstrahlung X-ray production

Accelerated charged particle usually resulted in the emission of electromagnetic radiation, but there are case when fast electron can undergo elastic collisions with the nucleus which results in no electromagnetic radiation. Figure 2.4 shows how electron must accelerate towards the nucleus during its deflection but, despite this acceleration, a quantum of electromagnetic radiation is emitted in only small percentage of cases. When such a quantum is emitted, the electron's kinetic energy is suddenly reduced by an amount equal to the energy of the quantum, which resulted in its sudden slow down or brake. The said quantum energy may be in the X-ray spectrum, and the radiation is known as Bremsstrahlung (braking radiation). The process is important in the production of X-rays from conventional X-ray tubes.

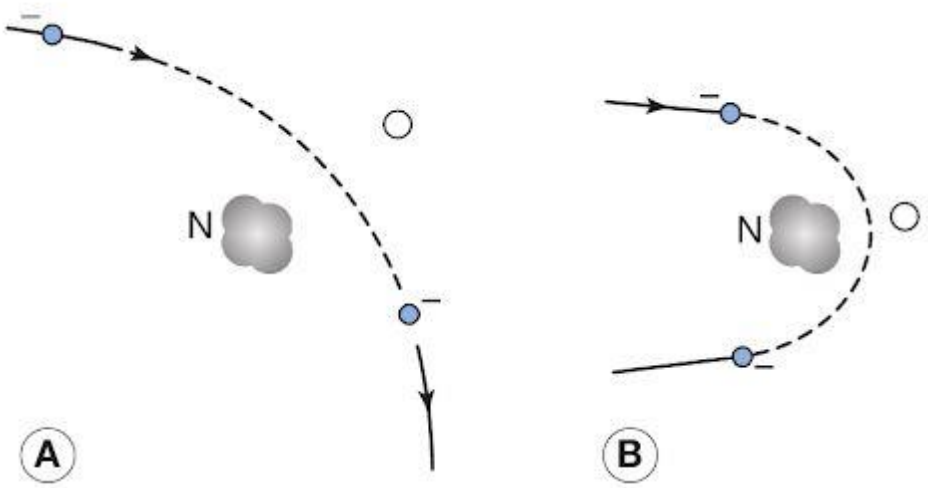

Figure 2.4 Illustration of neutron deflection when it interacts with nucleus of the target atom in the X-ray tube: (A) small deflection, (B) large deflection.

Figure 2.5 shows the process of Bremsstrahlung radiation. Electron at point P suddenly loses energy by the emission of an X-ray photon. After "braking" for a moment, the electron continues moving with a reduced energy (E_2). Only electrons that able to undergo a sudden loss of energy by an inelastic interaction with the nucleus can emit such photon, therefore the probability of Bremsstrahlung radiation to happen is very small (1-5% for diagnostic X-ray tubes).

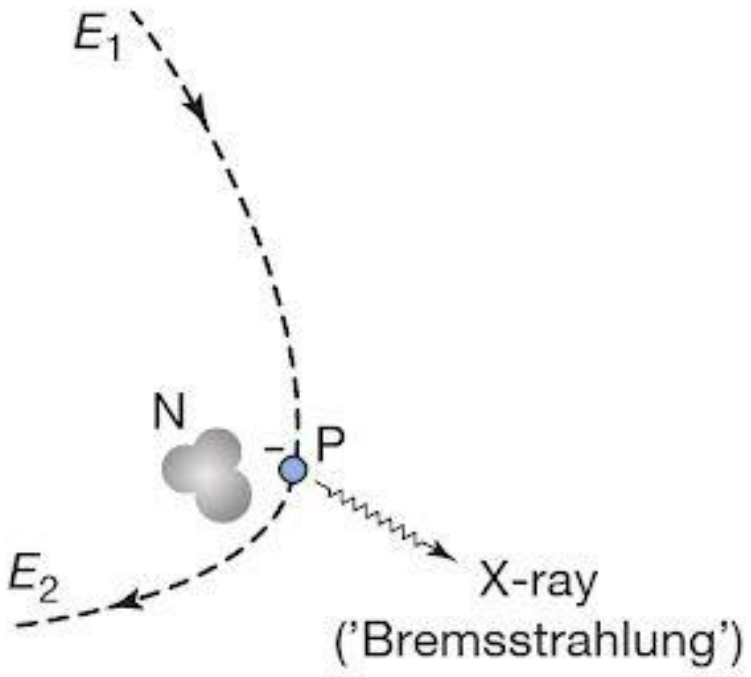

Figure 2.5 The production of Bremsstrahlung X-ray.

The atomic number of the target material for Bremsstrahlung radiation production affects the efficiency of the process. The higher atomic number of the target material, the more positive its nucleus, therefore it attracts more electron from the filaments which pass close to it, resulting in a more efficient Bremsstrahlung process and higher X-ray beam intensity. In diagnostic X-ray tubes, tungsten is used as the target material as its high atomic number (Z=74) leads to a higher intensity of X-ray production[39].

For monoenergetic electrons that slow down and stop in a given material, the Bremsstrahlung energy spectrum is a continuum with photon energies that extend as high as the electron energy itself. The emission of low-energy photons predominates, and the average photon energy is a small fraction of the incident electron energy. Because these spectra are continuous, they cannot be applied directly to the energy calibration of radiation detectors. The shape of the energy spectrum from an X-ray tube can be beneficially altered by filtration or passage through appropriate absorber materials. Through the use of absorbers that preferentially remove the lower-energy photons, a peaked spectrum can be produced that, although far from monoenergetic, can be useful in the energy calibration of detectors whose response changes only gradually with energy.

Bremsstrahlung is also produced by other sources of fast electrons, including beta particles. Therefore, some Bremsstrahlung photons are generated by any beta-active isotope encapsulated to stop the beta particles. Most commonly-available gamma-ray

sources decay by beta-minus emission, and the source encapsulation is usually also thick enough to stop these beta particles. In other cases, an external absorber may be used to prevent the beta particles from reaching the detector where their energy deposition would needlessly complicate the gamma-ray spectrum. In the absorption process, however, some secondary radiation in the form of Bremsstrahlung will be generated and may reach the detector and contribute to the measured spectrum. In principle, the Bremsstrahlung spectrum may extend to an energy equal to the maximum beta particle energy, but significant yields are confined to energies that are much lower than this value.

Because the Bremsstrahlung contribution cannot simply be subtracted as a background, its inclusion can lead to errors in quantitative measurements of areas under peaks in the gamma-ray spectrum. To minimize the generation of Bremsstrahlung, the use of beta absorbers made from low atomic number materials, such as beryllium, is often preferred. When compared with heavy charged particles, fast electrons lose their energy at a lower rate and follow a much more tortuous path through absorbing materials. These radiative losses take the form of Bremsstrahlung or electromagnetic radiation, which can emanate from any position along the electron track. From classical theory, any charge must radiate energy when accelerated, and the deflections of the electron in its interactions with the absorber correspond to such acceleration.

The linear specific energy loss through this radiative process is shown in equation (11)[18]:

$$-\left(\frac{dE}{dx}\right) = \frac{NEZ(Z+1)e^4}{137m_0^2c^4}\left(4\ln\frac{2}{m_0c^4} - \frac{4}{3}\right) \tag{11}$$

2.2.2 Theory of photonuclear reaction

When a photon is traveling through matter, there are several ways in which it can interact with the material and lose its energy. Some radioisotope gamma-ray emitters can also be used to produce neutrons when combined with an appropriate target material. The resulting photonuclear sources are based on supplying sufficient excitation energy to a target nucleus by absorption of a gamma-ray photon to allow the emission of a free neutron (photoneutron/photo-disintegration reaction).

Photoneutron or (γ ,n) sources emit near monoenergetic neutrons when the γ -emitter is also monoenergetic. Only two target nuclei, ^{9}Be and ^{2}H, are of any practical significance for radioisotope photonuclear sources, since the photon energy of isotopic γ -ray sources rarely exceeds 3 MeV. Beryllium photonuclear energy threshold is 1.665 MeV, and deuterium is 2.225 MeV. The corresponding reactions can be written as followed[40]:

$$^{9}_{4}Be + h\nu \rightarrow {}^{8}_{4}Be + {}^{1}_{0}n \quad \text{(Q-value = -1.665 MeV)}$$

$$^{2}_{1}H + h\nu \rightarrow {}^{1}_{1}H + {}^{1}_{0}n \quad \text{(Q-value = -2.225 MeV)}$$

When photonuclear reaction happens in a material, there is also a competition process going on simultaneously, and if the competition process' cross-section is as significant as the photonuclear reaction's cross-section, the photonuclear reaction will 'lose' to the competition process and the efficiency of neutron generation will decrease. In deuterium and beryllium's case, the competition process would be Compton scattering.

The photonuclear cross-section value for D_2O and ^{9}Be is 2.5 mb and 0.5 mb, respectively[41]. First, we shall calculate the cross-section ratio between deuterium's photonuclear reaction and Compton scattering:

D_2O σ (γ ,n) = 2.5 mb at 5 MeV

D_2O σ (compton) = 83 mb

D_2O σ (γ ,n) and σ (compton) ratio = 2.5/83 = 0.030

In the case of beryllium, the Compton scattering cross-section can be estimated from the comparison of the density between ^{9}Be and D_2O:

$^{9}Be/D_2O$ density = 1.85/1.11 (g/cm^3) = 1.67

^{9}Be σ (compton) = 83 x 1.67 = 138 mb

^{9}Be σ (γ ,n) = 0.5 mb (average)

^{9}Be σ (γ ,n) and σ (compton) ratio = 0.5/138 = 0.0036

From this calculation, it can be understood that beryllium has 10 times smaller ratio between its photonuclear reaction competition process' cross-section compared to D_2O. It shows that Compton scattering reaction is more dominant as the competition process, making it to be less efficient in terms of neutron generation.

However, in this research of compact electron linac-based neutron source, beryllium is chosen as the neutron target instead of deuterium mainly because it's less difficult to handle for the mobile usage. Since the efficiency decline is only within the factor of 10, using beryllium won't give so many significant differences when it comes to neutron

production for compact neutron source, as long as the advantage of its mobility and easy to handle can still be preserved.

A gamma-ray photon with an energy of at least the negative of the Q-value is required to make the reactions energetically possible, so that only relatively high-energy gamma rays can be applied. For gamma-ray energies that exceed this minimum, the corresponding neutron energy can be calculated from the equation (12):

$$E_n(\theta) \cong \frac{M(E_\gamma+Q)}{m+M} + \frac{E_\gamma\sqrt{(2mM)(m+M)(E_\gamma+Q)}}{(m+M)^2}cos\theta \qquad (12)$$

θ = angle between gamma photon and neutron direction

E γ = gamma energy (assumed << 931 MeV)

M = mass or recoil nucleus $\times c^2$

m = mass of neutron $\times c^2$

The advantage of photonuclear sources is that if the gamma rays are monoenergetic, the neutrons are also nearly monoenergetic. For large sources, the spectrum is also somewhat degraded by the scattering of some neutrons within the source before their escape. The main disadvantage of photonuclear sources is the fact that very large gamma-ray activities must be used in order to produce neutron sources of attractive intensity[18].

From the relation between photon yield of tantalum target and photoneutron yield of beryllium shown in figure 2.6, they both increase almost linearly with the electron energy increase, and beam current is decreasing as orbit number (energy) increases. This shows that in order to get maximum photoneutron yield, either electron energy or electron beam current can be increased. Figure 2.7 shows the neutron energy spectrum generated from the beryllium irradiation with 8.75 MeV bremsstrahlung radiation[42].

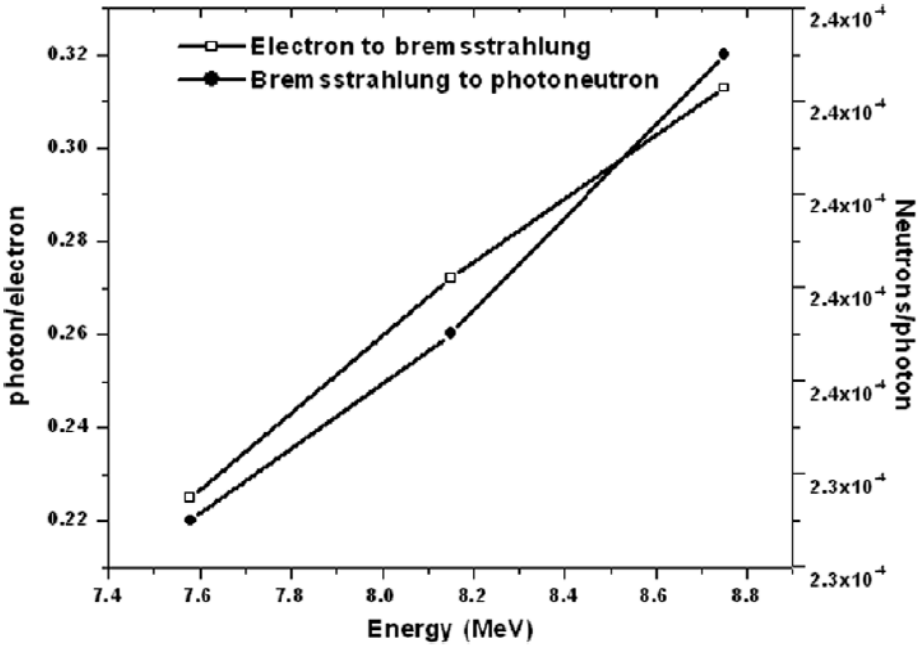

Figure 2.6 Electron to bremsstrahlung conversion factors for Tantalum target and bremsstrahlung to photoneutron conversion for beryllium target for different energy electrons and peak energy bremsstrahlung radiation.

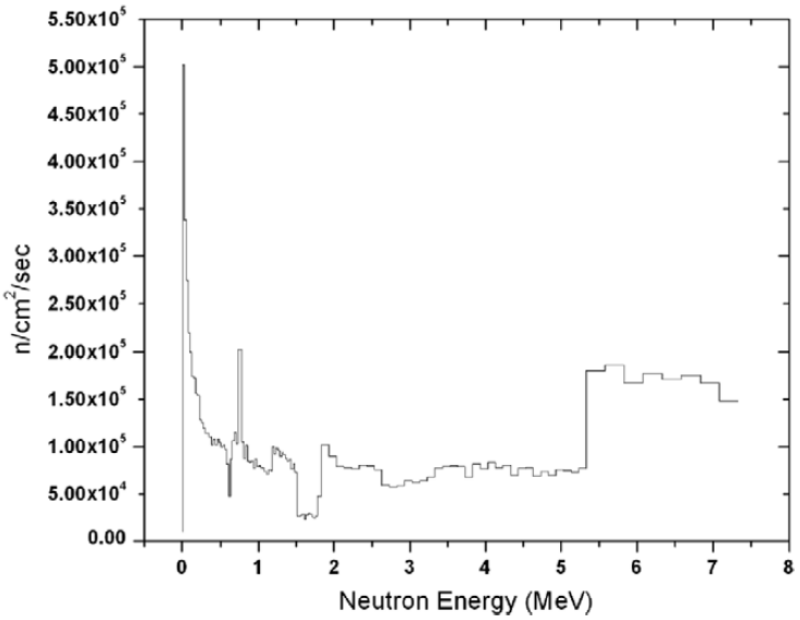

Figure 2.7 Photoneutron spectrum of beryllium irradiated by the 8.75 MeV microtron-based bremsstrahlung radiation.

2.3 X-band electron linac-based compact neutron source

From the explanation about the X-band linac and neutron source in the previous section, it can be understood that a compact linac-based neutron source is possible to be made by the combination of these two components. The 3.95 MeV X-band electron linac coupled with Tungsten and Beryllium is the system that we are using to build the compact neutron source in this research, which then would be able to produce pulsed neutron necessary for on-site NRTA for the purpose of identification of uranium and plutonium content inside nuclear debris sample.

By using electron linac, we can make a pulsed neutron source system by shooting a neutron target with electron. Tungsten (with copper layer as cooler) will convert these electrons into Bremsstrahlung X-ray, which then exposed to neutron target. Using a material with low threshold energy such as Beryllium (1.67 MeV) as neutron target will trigger photonuclear reaction by only using a relatively low energy electron, resulting in a more compact system of pulsed neutron source. Figure 2.8 shows the schematic of the X-band electron linac-based neutron source, and the neutron target schematic in the figure 2.9[43]. Figure 2.10 and 2.11 shows the actual photo of the system[44].

The 100-kilograms photo-neutron target was composed of $23 \times 23 \times 23$ cm^3 cube of lead which mainly serves as gamma ray shielding, filled with boric acid resin layer for neutron shielding and lead beam collimator. An L-shaped empty space is available inside to put in beryllium, as well as collimator for 3.95 MeV X-ray beam input and for pulsed neutron output. By using Monte-Carlo code and PHITS, the simulation of this pulsed neutron source has been performed to optimized the neutron flux, with the current calculated neutron intensity is 3.86×10^5 n/cm^2/sec (7.13×10^6 n/sec). In order to be able to get resonance neutron within the energy of 100 eV, a 2-cm thick polyethylene neutron moderator was put in front of the beryllium inside the lead beam collimator.

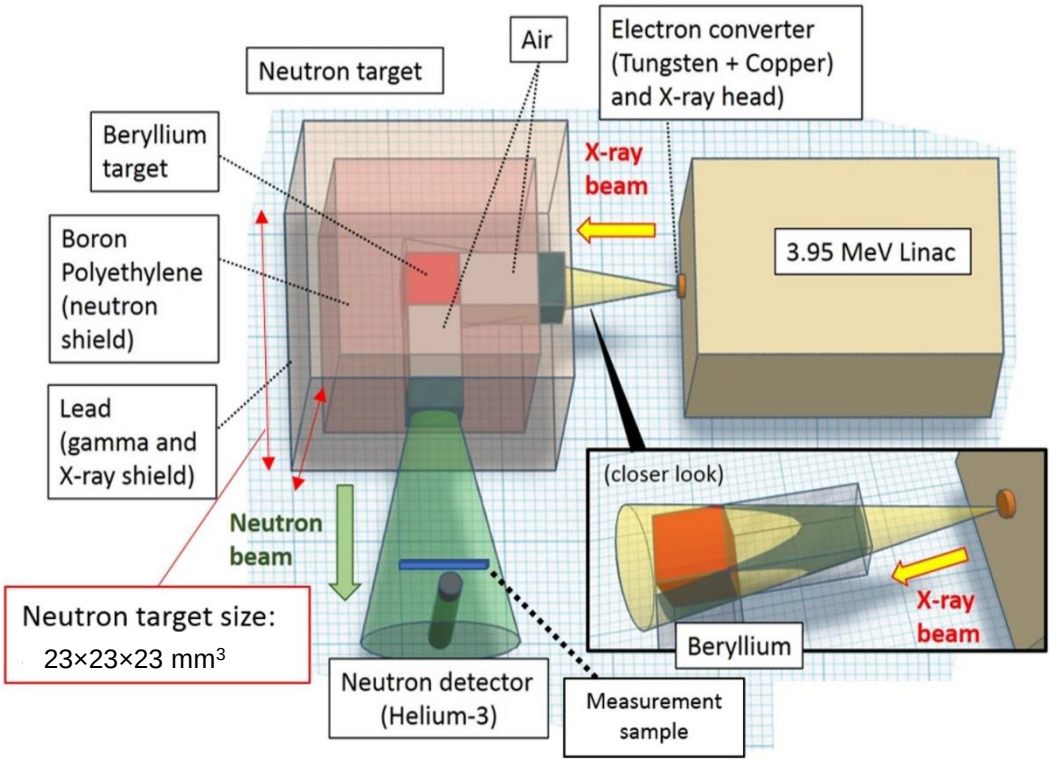

Figure 2.8 Schematic of the compact X-band electron linac-based neutron source.

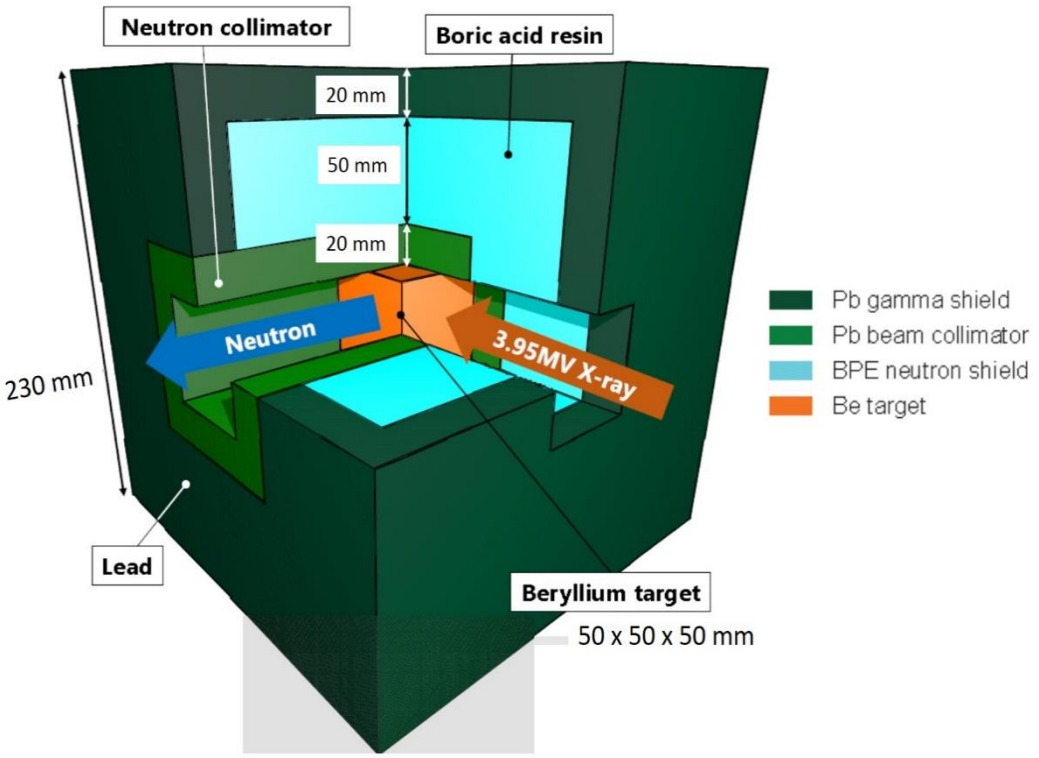

Figure 2.9 Schematic of the neutron target in compact neutron source.

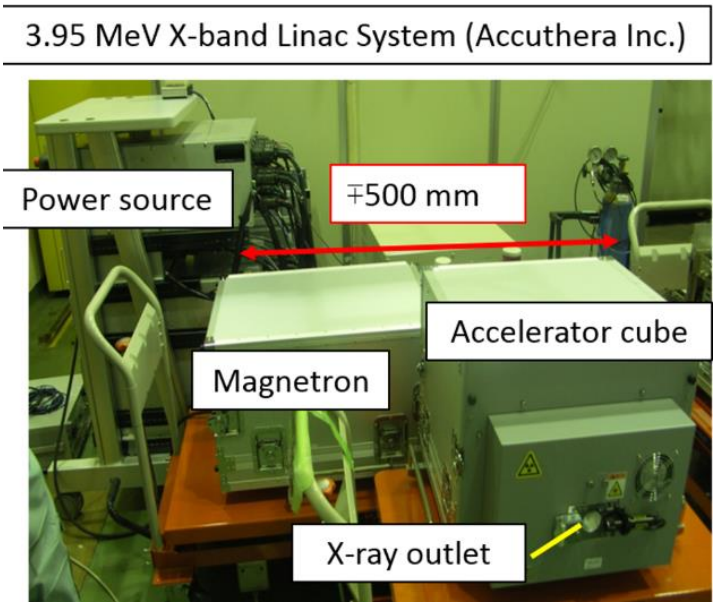

Figure 2.10 Photo of the actual 3.95 MeV electron linac-based neutron source: electron linac part.

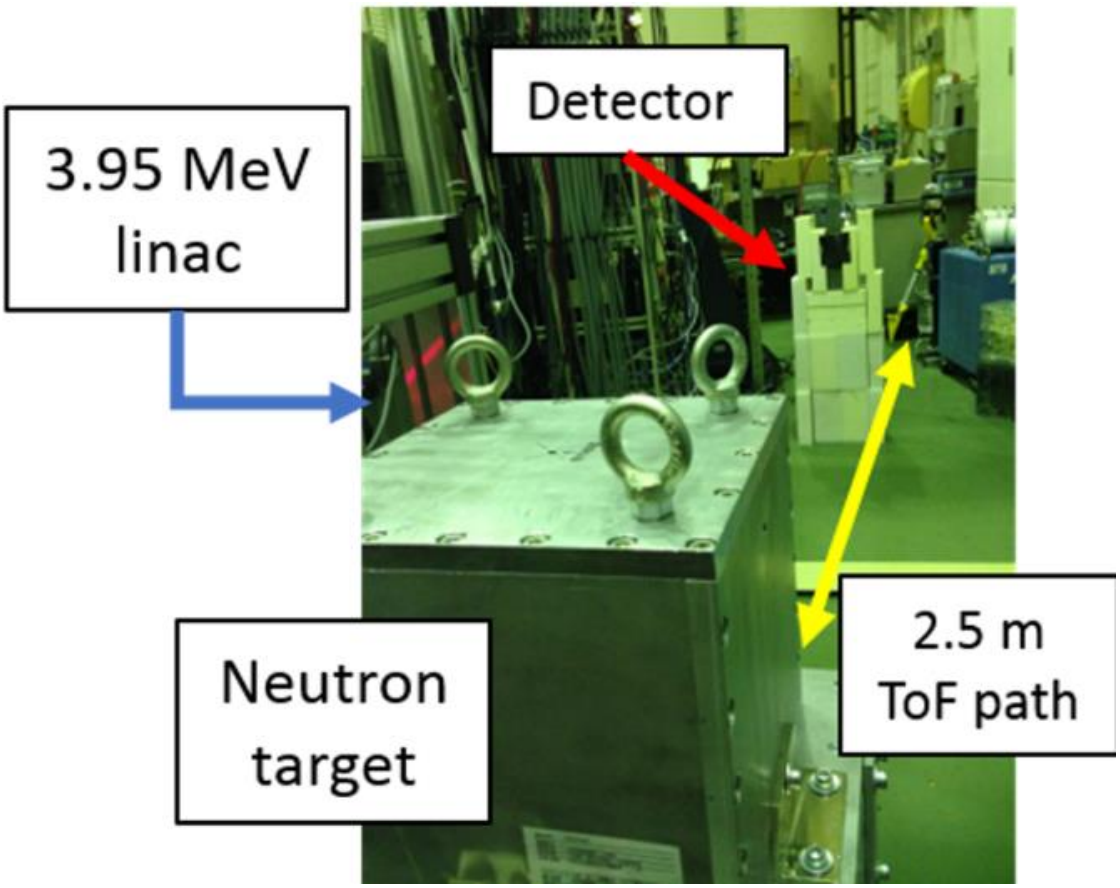

Figure 2.11 Photo of the actual 3.95 MeV electron linac-based neutron source: neutron target and detector part.

As mentioned in the introduction, the objective of the on-site inspection is only for screening of the nuclear debris. For that purpose, the mobility of the device is a priority compared to the detailed measurement information. Therefore, this X-band electron linac-based pulsed neutron source which biggest advantage is compactness and mobility would be the best choice for this screening system's neutron source.

2.4 Simulation on compact electron linac-based neutron source

To verify the neutron production and the flux of this neutron source, a Monte Carlo simulation using PHITS has been performed. The condition where the current setup of 3.95 MeV X-band electron linac-based neutron source were operating is simulated, and from there the estimation of the neutron flux and the distribution of the neutron energy can be calculated (details on the code and geometry of the simulation can be seen in appendix A).

This neutron source simulation uses a 3.95 MeV bremsstrahlung X-ray energy spectrum as the particle source, where cone-shaped X-ray beam source is placed at 30 cm distance from the beryllium target. Beam source energy spectrum value was obtained from the separate simulation of bremsstrahlung X-ray production by 3.95 MeV electron linac and tungsten target. The simulation of photon and neutron generation process were done separately to shorten the simulation time and minimize error. Parameters for the X-ray and neutron target size used in this simulation is shown in table 2.2.

Table 2.2 Parameters of the material size in the 3.95 MeV X-band electron linac-based neutron source simulation.

Tungsten thickness	0.5 mm
Copper thickness	1.6 mm
Tungsten and copper diameter	5 mm
Beryllium dimension	5 x 5 x 5 cm
Neutron target dimension	23 x 23 x 23 cm
Electron energy	3.95 MeV
Electron beam diameter	5 mm

In the figure 2.12 is the correlation between neutron energy and the flux produced by this compact neutron source system, according to the simulation result. Tally surface for the neutron energy spectrum sampling is at the surface of the beryllium target. Through PHITS calculation, the estimated neutron flux production is 3.86×10^5 n/cm^2/sec, which rounds it up to around 10^7 n/sec. This value is relatively low compared to the usual neutron source for NRTA that has produced neutron with flux value around 10^{10} n/sec, but since the TOF path that will be used for the NRTA experiment in this research is much shorter, this flux value should be enough for that purpose.

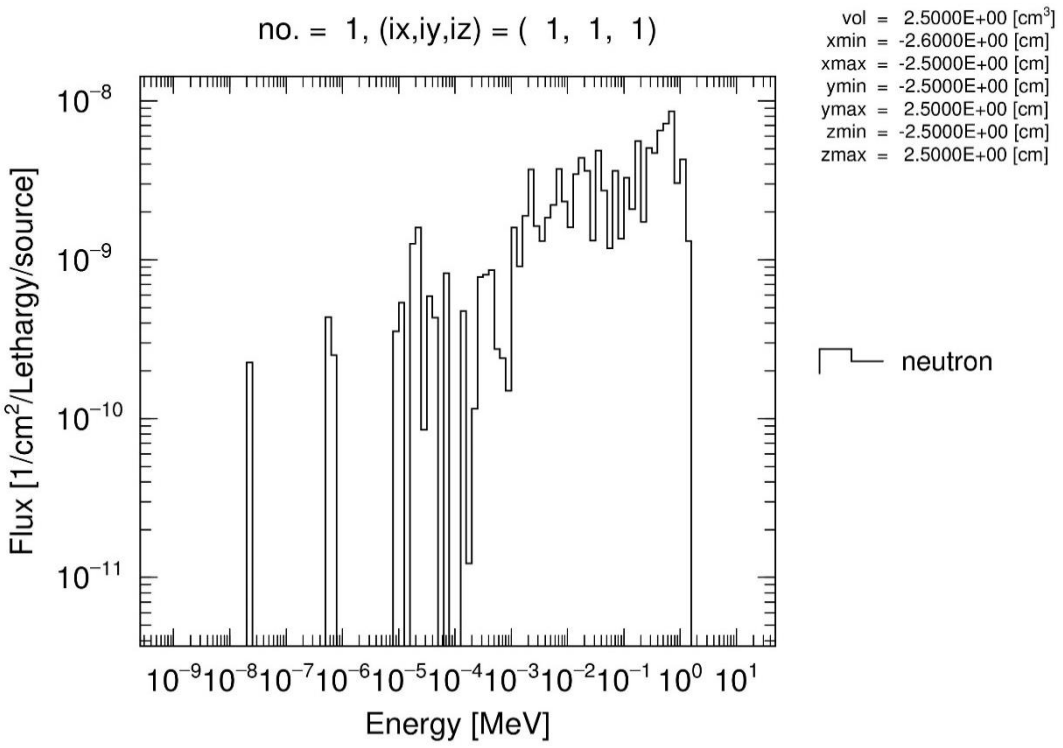

Figure 2.12 Simulation result of 3.95 MeV electron linac-based neutron source, a plot of the neutron source's energy spectrum versus its corresponding neutron flux.

2.5 Radiation safety control for compact neutron source usage

As this compact neutron source system is a new technology, it needs to comply with Japan's regulation of radiation source usage. Previously, 950 KeV X-ray source has been registered at the local agency of labor supervision, and it was allowed to be used in a Controlled Radiation Area at the measurement site with a sufficient shielding around the source and object to reduce the air dose rate below 1.3 mSv/3 months. This area has radiation safety system under the provisions of the Regulations on Prevention of Ionizing Radiation Hazards[37].

In Japan, as long as the application is only for non-destructive testing of infrastructures, X-ray source with energy below 4 MeV is allowed to be used outside. The X-ray source for this compact neutron source system has the energy of 3.95 MeV, but it would be a different case with neutron source. The main concern with it is that with neutron source usage, the argon dose in the air gets increased by 30%. Therefore, a special room designed to control the dose of the neutron radiation needs to be prepared as well on the measurement site. Another thing is the cooling of the system is necessary to reduce the radiation dose in the air, meaning that the on-site measurement can only be done few times in a month, and performed within a short time for each session.

2.6 Discussion

Pulsed neutron source system is usually consisted of pulse electron accelerator coupled with material that can emits neutron when hit by fast electrons. In this case, in order to make a compact and portable pulsed neutron source, the electron linac should be the compact type as well. The one used in this research is X-band type electron linac with the highest RF frequency, resulting in short nanosecond pulse. Its small size is also making it possible for portability. By coupling it with an electron-to-photon converter and photon-to-neutron converter, a compact electron linac-based neutron source can be constructed.

The photon converter will be bremsstrahlung X-ray source, and tungsten is used as the target material because of its high atomic number that leads to a higher intensity of X-ray production. As for the neutron target, the only effective material for photonuclear reaction are only D_2O and ^9Be, where both materials have photonuclear reaction threshold energy below 3 MeV. Even though its competitive reaction cross-section is higher, ^9Be is easier to handle and use compared to D_2O when it comes to mobile neutron source use. With that consideration and that the effectivity ratio difference is only within the factor of 10, the neutron target chosen for this research is ^9Be.

PHITS calculation to estimate the neutron flux production of this compact neutron source has been performed as well and shows the value of 3.86×10^5 n/cm^2/sec, which rounds it up to around 10^7 n/sec. This value is relatively low compared to the usual neutron source for NRTA that has produced neutron with flux value around 10^{10} n/sec, but since the TOF path that will be used for the NRTA experiment in this research is much shorter, this flux value should be enough for short-distance neutron TOF measurement. Moreover, the biggest advantage of this X-band electron linac-based neutron source is its compactness and portability, which makes it possible to perform on-site nuclear debris screening.

3. Neutron resonance transmission analysis using short-distance time-of-flight method

Based on the explanations of the electron linac-based neutron source and its simulation, the pulsed neutron can be produced by coupling the electron linac with tungsten to produce bremsstrahlung X-ray, and with neutron target beryllium to produce neutron from the X-ray. Therefore, it is also possible to construct a neutron TOF measurement system by using this neutron source.

This system will be the first kind to utilize mobile neutron TOF measurement system through short-distance TOF path, which main purpose is to identify Uranium and Plutonium isotopes in a nuclear debris. Schematic and theory of this concept, as well as the experiment settings on the feasibility test of this system will be explained further in this chapter.

3.1 Schematic of the system

The short-distance TOF measurement method will utilize more or less the same settings with the normal-distance TOF method, but with a much smaller scale. If the normal TOF path distance is 10 to 20 meters at the shortest, this short-distance measurement system will have 2.5 meters distance. Shorter distance will make the neutron energy range that can be measured to be much smaller, but it would still be within the range of the resonance neutron and the neutron energy absorption value of the isotopes subjected for detection. The schematic of the short-distance TOF measurement schematic is shown in the figure 3.1, and the details on the neutron detector part is shown in figure 3.2. The distance of 2.5 meters for flight path were calculated from the relation between thermal neutron energy of 0.025 eV and its velocity of 2200 m/s. in order to reach 100 eV neutron energy spectrum range, and considering the detector's dead time, the minimum flight path distance needed is 2.5 meters.

The measurement will be done indoor with radiation dose-controlled area, in the normal atmosphere and room temperature (no neutron closed track). Sample for the measurement should be a very thin sheet-shaped sample to simulate particle-like debris used in the common NRTA demonstration.

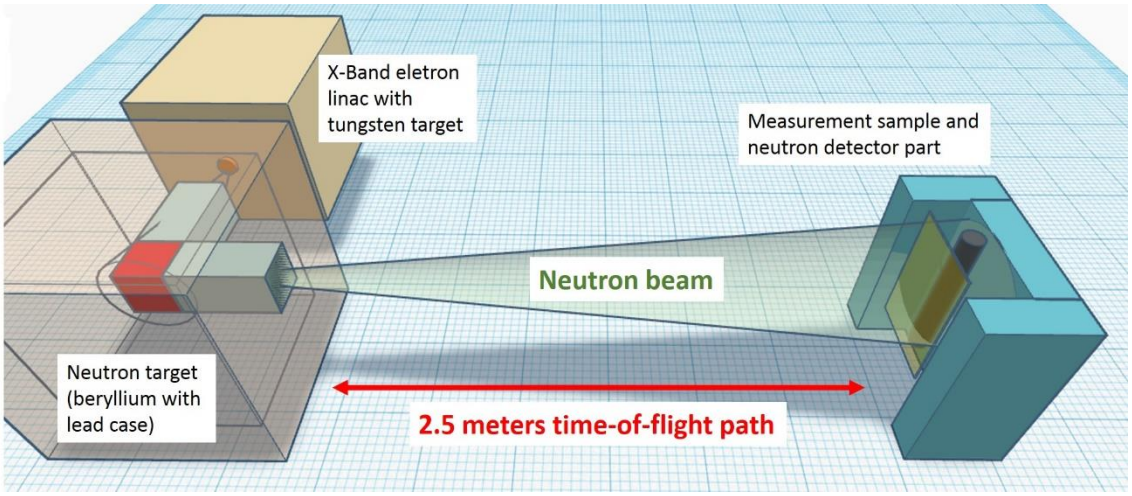

Figure 3.1 Schematic of the short-distance neutron TOF measurement concept.

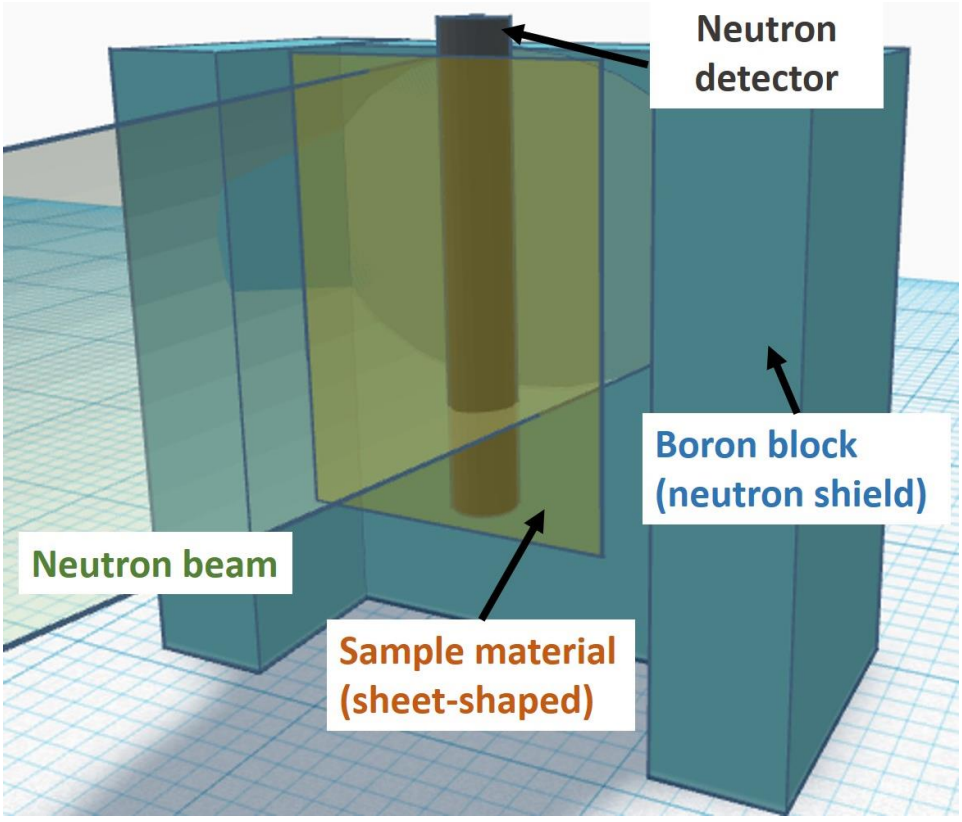

Figure 3.2 Schematic of the short-distance neutron TOF measurement concept, closer look on the sample and neutron detector part.

3.2 Neutron detectors

The relative probabilities of the various types of neutron interactions change dramatically with neutron energy. Neutrons are divided into two categories on the basis of their energy, which are “fast” neutrons and “slow” neutrons. The dividing border will be at about 0.5 eV, or about the energy where the drastic decrease in absorption cross-section in cadmium for energy over 0.5 eV happen[18]. Considering this factor, before we choose a neutron detector for this purpose of short-distance TOF measurement, the range of the neutron energy that is subject to measurement needs to be known first.

In the case of this research, the neutron energy range subjected to measurement is the resonance neutron area, which is 1-300 eV and this range falls in the slow neutron area. Therefore, it is more effective to choose for the material which capture cross-section is larger in this energy range, since capture reaction is more dominant in slow neutron. However, most of slow neutron detectors can only detect neutron positions and counts and cannot detect their energies, though it is still can be used in TOF measurement method.

There are three common isotopes with a considerably high neutron capture cross-section especially in the slow neutron area used for neutron detector: ^{10}B, ^{6}Li, and ^{3}He. The plot of their neutron capture cross-section is shown in the figure 3.3[45]. For slow neutrons (< 10 keV), reactions with large positive Q-values are required to produce secondary charged particles of sufficient energy in order to make the neutron detection easier. The lower cross section is generally a disadvantage but is partially offset by the higher Q-value and resulting greater energy given to the reaction products. ^{6}Li occurs with a natural isotopic abundance of 7.40% and is also widely available in separated form[18]. Despite having lower capture cross-section, ^{6}Li has the largest Q-value among the other two isotopes.

Based on the neutron capture cross-section plot, ^{3}He detector would be the generally better choice of neutron detector suitable to this research needs, and has been widely used. This neutron detector type is also the main detector to be used in the TOF experiments of this research. The image of ^{3}He neutron detector is shown in figure 3.4[46].

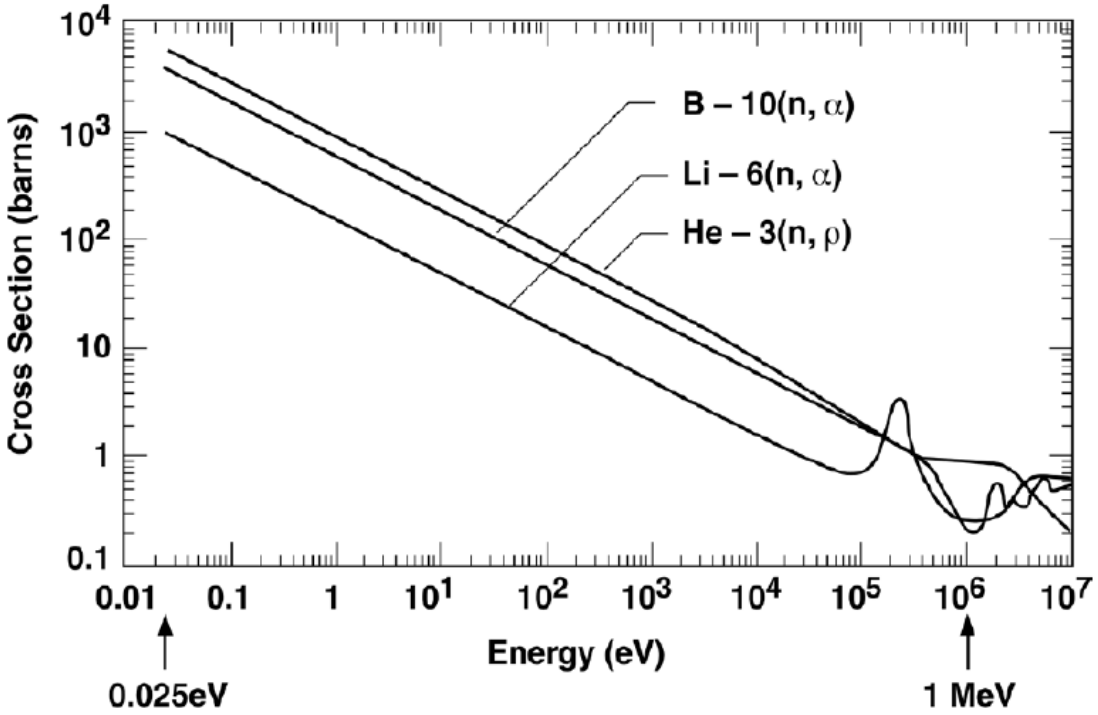

Figure 3.3 The neutron capture cross-sections for ^{10}B, ^{6}Li, and ^{3}He.

Figure 3.4 Image of ^{3}He neutron detector.

However, one significant concern regarding the use of ^{3}He as gas proportional detectors is the global shortage of ^{3}He. The isotope is rarely found in nature but exists as a decay product of tritium, which is primarily produced in nuclear reactors. Because of the ^{3}He shortage, a replacement technology for neutron detection is required in the very near future [47]. It is estimated that the total ^{3}He demand is ~65 m^3/year, while total supply is ~15 m^3/year[48]. Therefore, for long-time usage, using an alternative neutron detector aside from ^{3}He should be considered as well.

Other type of neutron detector potential for NRTA measurement would be LiCAF, or LiCaAlF6, which is a scintillator crystal consist of Lithium-6, Calcium, Aluminum, and Hexafluoride. As for the neutron detection element, LiCAF has ^{6}Li to detect neutron via neutron capture reaction. ^{6}Li has a large neutron absorption cross-section, and low gamma sensitivity due to its light composition as well as other elements forming this scintillator crystal[49].

3.3 Experimental setup

Experiment on short-distance TOF neutron resonance transmission analysis has been performed at Tokai Campus of The University of Tokyo. For safety reason, instead of radioactive elements, this experiment used non-radioactive dummy materials with neutron energy absorption value similar to that of ^{238}U the details of these materials will be explained in the next chapter about experiment results. Through Time-of-flight measurement method, the formed resonance peak in the experiment can be used to identify the isotopes contained within the sample material. Figure 3.5 shows the experimental setup to measure neutron Time-of-flight. The setup is divided into 3 main parts: neutron source part, signal amplifier part, and digital signal processing part.

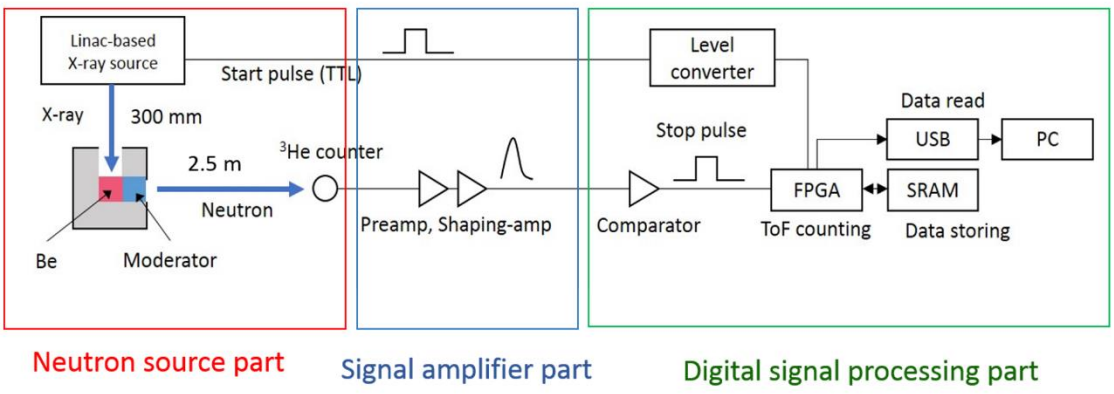

Figure 3.5 Experimental setup to measure neutron TOF.

The actual setting photo for the configuration of the sample and neutron detector of the neutron source part can be seen at figure 3.6. The sample materials used in the following experiments are sheet-shaped with the thickness of 0.1 mm to simulate the particle-like sample of nuclear debris and based on the past research of optimum sample thickness for NRTA measurement as well[50]. Samples are held onto the boron block moderator while the open space between them will be the measured area, with about 6 cm apart from the surface of the ^{3}He detector which is covered by the lead cover, making the effective measurement area to be 20×80 mm^{2}. In the experiment where the sample size is smaller than the detection area, a 20×20 mm^{2} sample size was used, as shown in figure 3.7. The thickness of the sample can be adjusted by combining multiple sheets for a measurement.

In the case where a sample material is put in front of the detector, resonance peak in the energy spectrum will appear as the emitted pulsed neutron passed through the sample material. This way, we can match the observed resonance peak from the neutron spectrum obtained through experiment with the one from references in order to see if this isotope detection system works properly.

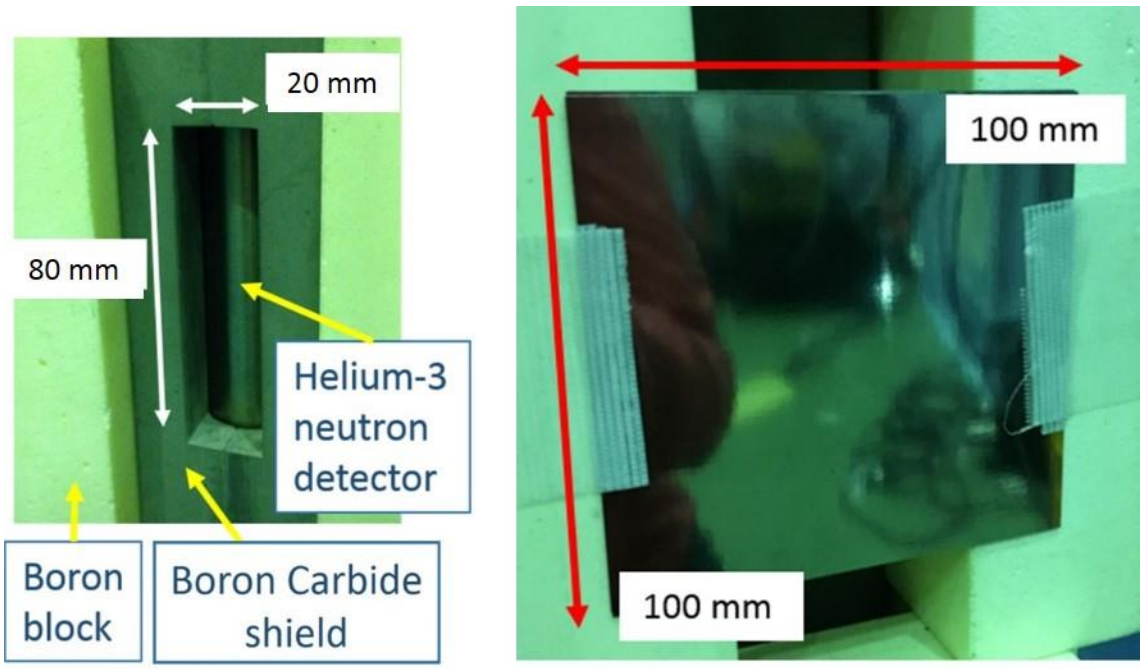

Figure 3.6 Sheet-shaped sample used for the NRTA experiment (right) and the size of the neutron detector window (left).

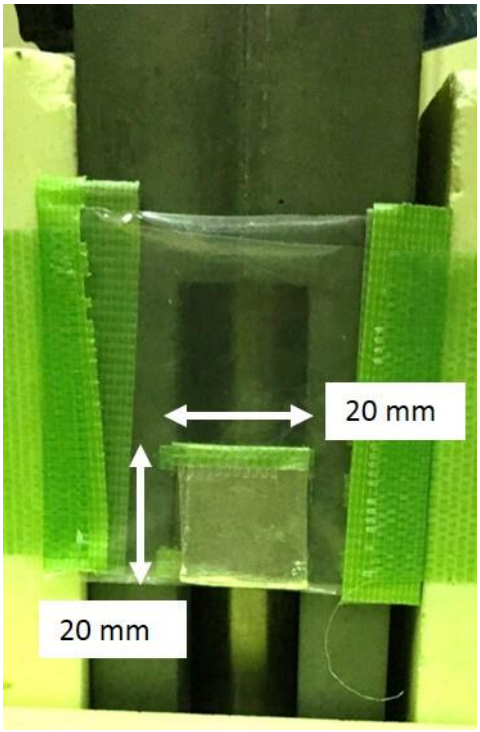

Figure 3.7 Sheet-shaped sample used for the NRTA experiment with the size of 20×20 mm^2.

In neutron source part, aside from the neutron source that has been explained in the previous chapter, there are also several detector components. X-band electron-linac based neutron source produced pulsed neutron, where it is detected by the ^{3}He neutron detector. In order to be able to use ^{3}He detector and read the signal detected by it, equipment such as high voltage power supply and amplifier is needed.

The high-voltage power supply (HVPS) provides a positive or negative voltage necessary for the operation of the detector. Figure 3.8 shows the front and rear view photos of a HVPS[51]. The HVPS is constructed in such a way that the HV at the output changes very little even though the input voltage (110 V, AC) may fluctuate. The front panel has an indicator light that shows whether the unit is on or off and, if it is on, whether the output is positive or negative voltage. There are two knobs for voltage adjustment, one for coarse changes of 500-V intervals, and the other for changes of 0.1 V. The output is at the rear of the unit[52].

Figure 3.8 High voltage power supply (right: front view, left: rear view).

Before going through amplifier, the signal that comes out from the output of a detector goes through the preamplifier first. The primary purpose of the preamplifier is to convert the current signal into voltage signal, as well as provide an optimized coupling between the output of the detector and the rest of the counting system to minimize any sources of noise that may change the signal. Schematic of a preamplifier is shown at figure 3.9[53]. The preamplifier shapes the signal and reduces its attenuation by matching the impedance of the detector with that of the amplifier. After going through the preamplifier, the signal may be safely transmitted to the amplifier[52].

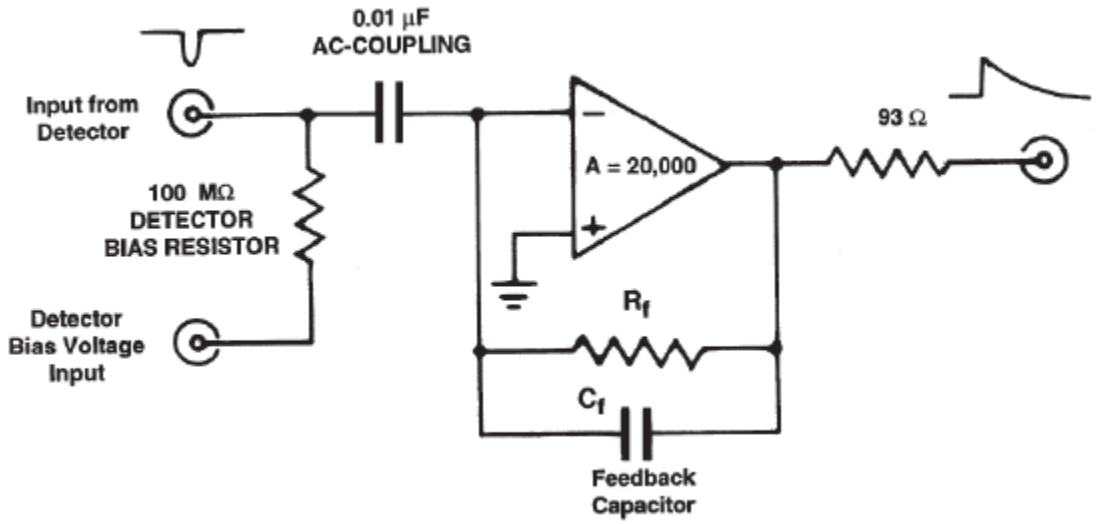

Figure 3.9 Diagram of the AC-coupled charge-sensitive preamplifier.

Charge-sensitive preamplifiers are preferred for most energy spectroscopy applications. The signal from a semiconductor detector or ion chamber is a quantity of charge delivered as a current pulse lasting from 10^{-9} to 10^{-5} seconds, depending on the type of detector and its size. For most applications the parameters of interest are the quantity of charge and/or the time of occurrence of an event. A charge-sensitive preamplifier can deliver either or both. Because it integrates the charge on the feedback capacitor, its gain is not sensitive to a change in detector capacitance, and in the ideal case, the rise time of the output pulse is equal to the detector current pulse width[53].

On the signal amplifier part, the main amplification unit is the amplifier, which increases the signal by as many as 1000 times or more. Modern commercial amplifiers produce a maximum signal of 10 V, regardless of the input and the amplification. Figure 3.10 shows a photo of front and rear view of an amplifier unit[54].

Figure 3.10 Amplifier (right: front view, left: rear view).

In addition to signal amplification, an equally important function of the amplifier is to convert the signal at the output of the preamplifier into a form suitable for the measurement desired, in other words, shaping the signal. Most commercial amplifiers provide at the output two types of pulses, called unipolar and bipolar[52]. For the case of 3.95 MeV X-ray source, the gamma burst from it will create a long dead time for the detector. Therefore, bipolar shaping is better than unipolar because it can quickly recover the signal baseline to zero, getting the measurement starts back again in short time.

And lastly, at the digital signal processing part, both signal from the detector and the accelerator are recorded in order to calculate their time difference which will represent the neutron's flight time. In order to match the square-shaped signal (digital signal) coming from the accelerator, the sinusoidal signal shape from the detector needs to be

converted into square-shaped signal as well by using comparator, and the signal from accelerator needs to be adjusted with voltage divider as well.

The comparator is an electronic decision-making circuit that makes use of an operational amplifiers with very high gain in its open-loop state where there is no feedback resistor. The op-amp comparator compares one analogue voltage level with another analogue voltage level, or some preset reference voltage, V_{REF} and produces an output signal based on this voltage comparison. In other words, the op-amp voltage comparator compares the magnitudes of two voltage inputs and determines which is the largest of the two[55].

To use operational amplifiers in open loop as comparators is quite common. This especially applies when an op-amp is already used in the application, giving the user the opportunity to use a dual channel (or quad channel) op amp which can save space in the application. This is possible even if a better alternative is to use comparators that are optimized for this purpose. Comparators, on the other hand, are designed to operate in open loop configuration without any negative feedback. In most cases, they are not internally compensated, the speed (propagation delay) and slew rate (rise and fall time) are maximized, and overall gain is also usually higher.

A single device has, ordinarily, five pins: two for power supply V_{CC}+, V_{CC}-, two as inputs V_{IN}+, V_{IN}- and one for the output V_{OUT}. It is possible to have an extra pin for standby function. When $V_{IN}(+) > V_{IN}(-)$, the output is in high state, if $V_{IN}(+) < V_{IN}(-)$, the output is in low state. Figure 3.11 shows the example of a comparator circuit[56].

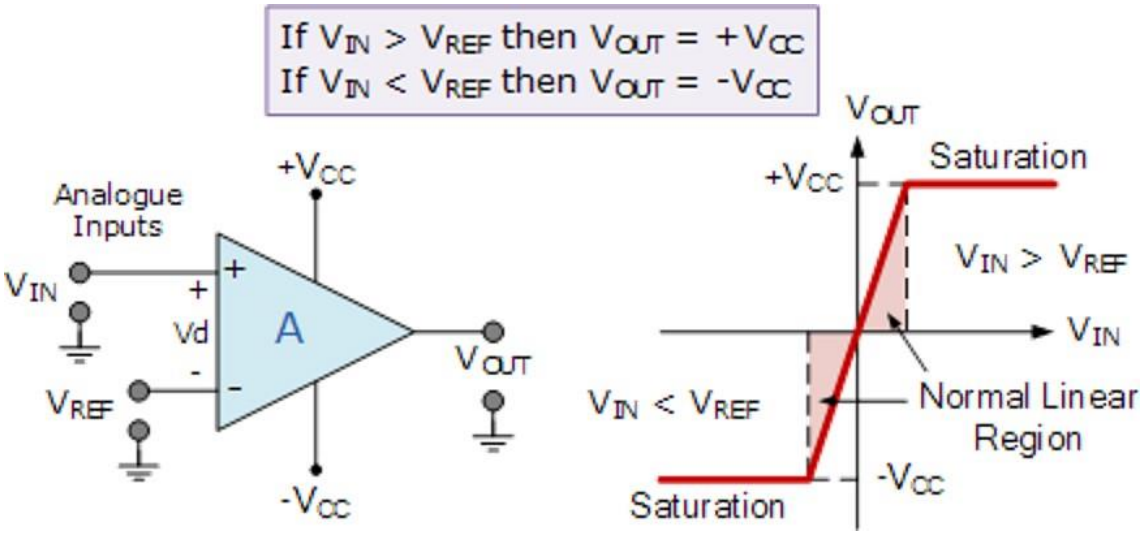

Figure 3.11 Diagram of an op-amp comparator circuit.

The example of how comparator work is explained in the figure 3.12. The comparison in this case was made by a TS3011 comparator between a 20 m V_{PP} input signal (blue) applied on V_{IN}+ and a 50 mV DC reference voltage (green) applied at V_{IN}-. The output signal (red) amplitude is 5 V. As can be seen, sometimes, the input signal exceeds the reference voltage though the output remains low. This is caused by the internal hysteresis voltage of the TS3011[55].

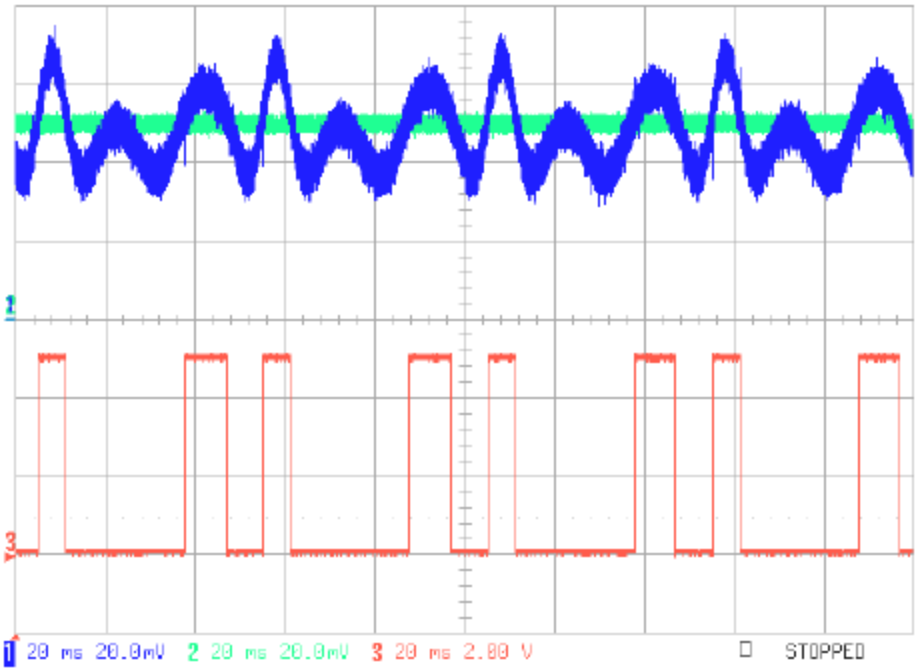

Figure 3.12 Signal comparison between the input and output from a comparator (blue is the input signal, green is the reference/threshold voltage, and red is the output signal).

For the purpose of the need in this experiment, a custom-made comparator circuit system was assembled, and the photo is shown in figure 3.13.

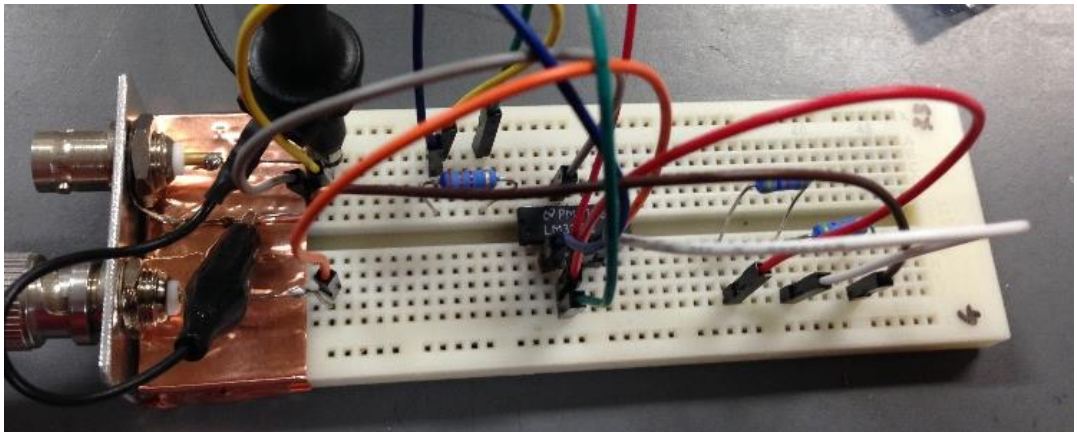

Figure 3.13 Comparator, the component for converting analog signal from amplifier into digital signal.

To confirm that the signals are transmitted and detected successfully, as well as to confirm the signal shape, an oscilloscope is connected to the signal sources from both the accelerator and the detector. The oscilloscope is an instrument that permits the study of rapidly changing phenomena, such as a sinusoidal voltage or the pulse of a counter. The phenomenon is observed on a fluorescent screen, with the horizontal axis to measures time and vertical axis gives volts. Figure 3.14 shows a photo of commonly-used oscilloscope[57].

In radiation measurements the oscilloscope is used to check the quality of the signal as well as the level and type of the electronic noise. It is always a good practice before any measurement is attempted to examine the signal at the output of the amplifier. Modern oscilloscopes provide analog as well as digital signals[52]. The output from the oscilloscope used in this experiment is shown in figure 3.15. The green signal is the analog signal output from a ^{252}Cf sample measurement, and the red squared signal is the output from the comparator.

Figure 3.14 Image of commonly-used oscilloscope.

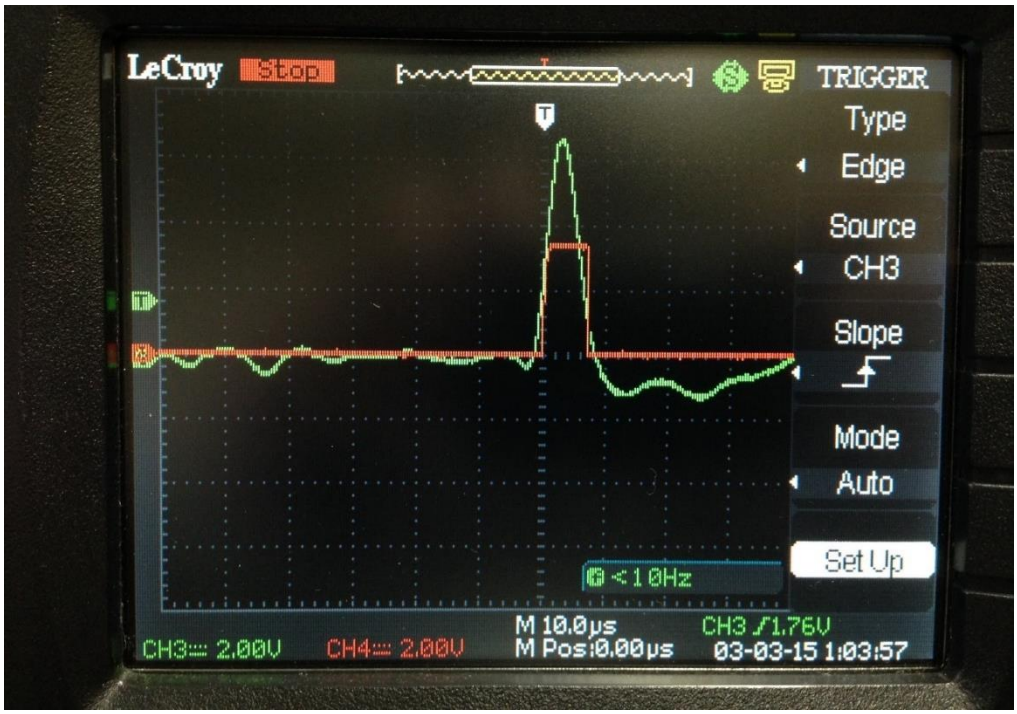

Figure 3.15 Neutron energy signal from a ^{252}Cf sample measurement with square-shaped signal conversion by comparator.

While the output signal from the accelerator doesn't need any conversion as the output is already square-shaped, the voltage is still higher than the one from the detector, therefore it also needs adjustment by using a voltage divider. The function of a voltage divider circuit or equipment is to drop the voltage of a signal so it can be measured with a smaller input range, to the level the analog or digital input can measure.

A voltage divider takes advantage of the fact that the voltage across one of the resistors in a circuit is proportional to the voltage across the total resistance in the circuit. The trick to using a voltage divider is to choose two resistors with the proper proportions relative to the full scale of the analog or digital input and the maximum signal voltage. The phenomena of dropping the voltage proportionally is often called attenuation. The formula for attenuation is:

$$A = R1 + R2/R2 \tag{13}$$

The variable A is the proportional difference between the signal voltage max and the full scale of the analog input. Schematic of a simple voltage divider can be seen in figure 3.16[58].

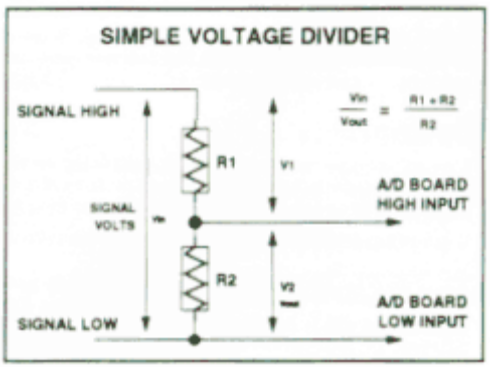

Figure 3.16 Schematic of a simple voltage divider.

After the two signals are confirmed to have the matched shape and voltage size, it can be subtracted to calculate neutron TOF through Field-Programmable Gate Array (FPGA). FPGA is a set of digital integrated circuit that contain programmable blocks of logic along with configurable interconnects between these blocks. This device can perform a tremendous variety of tasks by its programming flexibility. FPGAs are often used to prototype designs or to provide a hardware platform on which to verify the physical implementation of new algorithms[59]. In this experiment, the FPGA has been

programmed to calculate the time difference between the two signals from the detector and accelerator respectively, and record it before transferred as neutron count data to the PC for further data analysis. The photo of the FPGA used in this experiment is shown in figure 3.17.

The recorded data of the TOF is later converted manually to energy axis and plotted into neutron energy spectrum plot by using a TOF to neutron energy spectrum conversion program written in Python language.

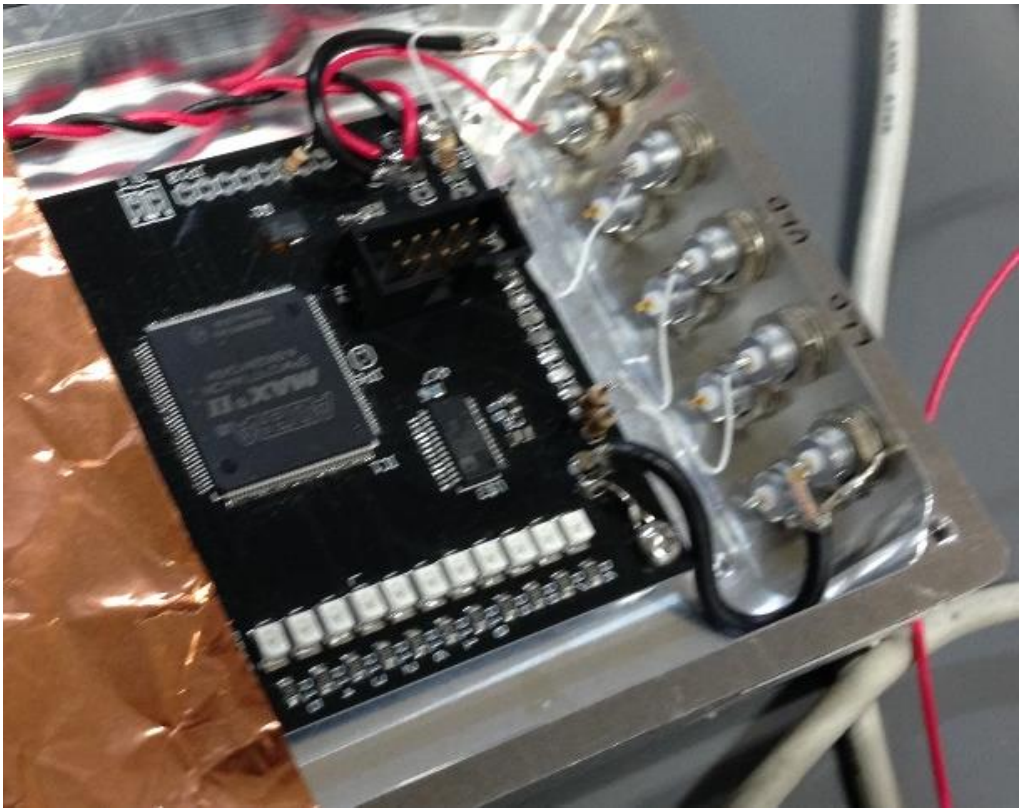

Figure 3.17 FPGA: Field-Programmable Gate Array, programmed to calculate neutron TOF.

3.4 Simulation of NRTA using short-distance time-of-flight system

To test the capability of this compact neutron source system to detect the isotopes in the nuclear fuel debris, PHITS simulation of NRTA has been performed (details of the simulation code and geometry can be seen at appendix B). The condition of the experiment is the same as the actual experiment setup for the neutron source part, and the detector used in this simulation is ^{3}He. Material sample for this simulation is also sheet shaped of 0.3 mm thickness, but this material is only containing uranium and plutonium mix. Specifically, only ^{235}U, ^{238}U, ^{239}Pu, ^{240}Pu and ^{242}Pu were used in the sample configuration of this simulation, since only these five isotopes having the dominant resonance peak in the 1-100 eV neutron energy spectrum. While this is the range that the short-distance neutron TOF system able to measure, these isotopes are also the dominant ones in uranium and plutonium. Therefore, being able to detect them means that the presence of uranium and/or plutonium inside a nuclear fuel debris sample can be confirmed.

Figure 3.18 shows the NRTA result from a Monte Carlo simulation using sample containing ^{235}U, ^{238}U, ^{239}Pu, ^{240}Pu and ^{242}Pu mix, measured from the position of ^{3}He. It shows a distinguished resonance peaks to each other which are relatively easy to be identified by using neutron energy absorption reference of each respective elements.

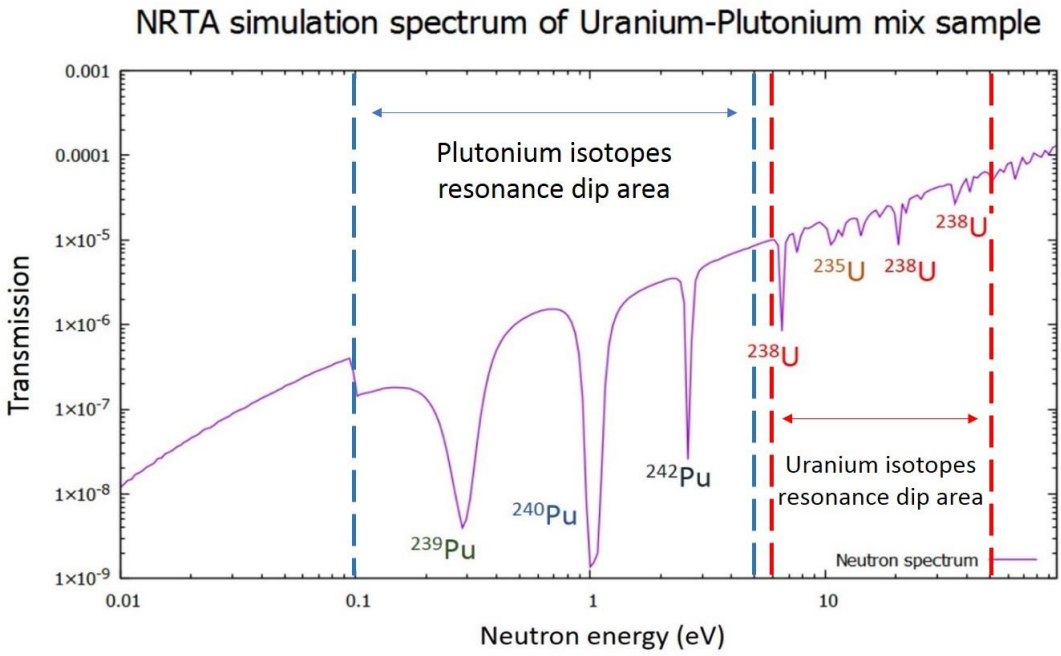

Figure 3.18 NRTA simulation result for a material with different contents, the resonance peaks represent specific isotopes.

3.5 Feasibility of short-distance NRTA to identify uranium/plutonium content in nuclear fuel debris

Based on the investigations of TMI-2 nuclear debris and simulations on MCCI, the materials contained inside nuclear fuel debris consists of zirconium oxide, uranium oxide, iron or stainless steel, and chromium. The example of the SEM image on a sample debris from TMI-2 core can be seen on figure 3.19[5]. In the aspect of nuclear debris size, the common nuclear debris powder that can be extracted from reactor have average of 5-10 mm diameter, and is within the detection capability of the neutron detector that will be used in this short-distance NRTA system.

Among these materials, none of them having resonance energy below 100 eV except Uranium isotopes (^{235}U, ^{238}U) and Plutonium isotopes (^{239}Pu, ^{240}Pu and ^{242}Pu). Figure 3.20 shows the neutron reactions cross-section of major isotopes of Zirconium (^{90}Zr), Iron/stainless steel (^{56}Fe) and Chromium (^{52}Cr), and all of them show neutron absorption value above 100 eV[20]. This value is outside of neutron energy range that can be obtained through short-distance TOF, and their resonance peak will not be able to be detected by the NRTA method using this compact neutron source system. In the simulation of NRTA with U/Pu material explained in the previous section, ^{235}U, ^{238}U, ^{239}Pu, ^{240}Pu and ^{242}Pu also has quite distinguishable resonance peak to each other, that should be relatively easy to be identified. Therefore, this on-site screening system using compact neutron source should be able to identify the Uranium and Plutonium resonance peak, without being disturbed with any other resonance peak coming from another material inside the nuclear fuel debris.

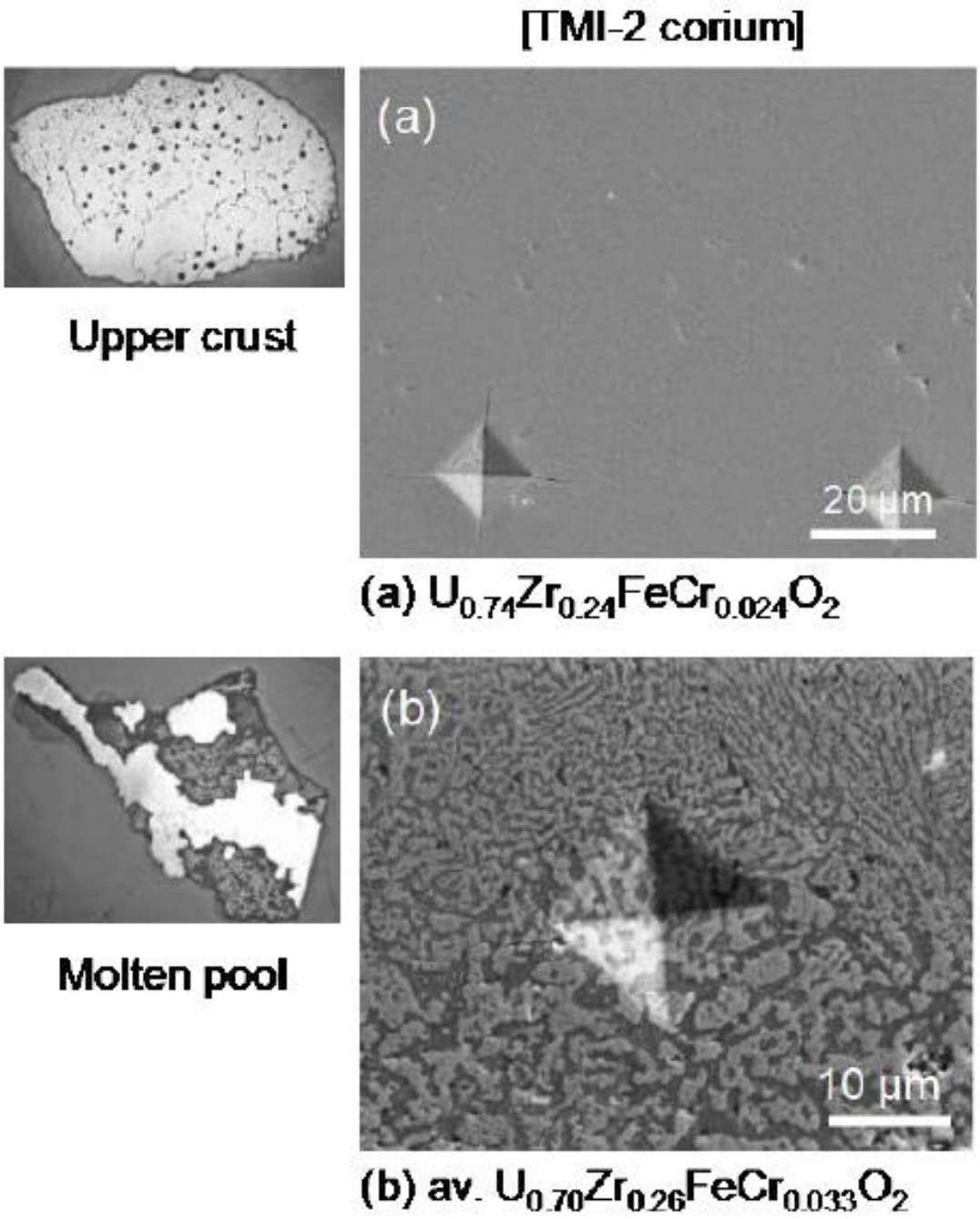

Figure 3.19 SEM images of polished cross-section of the TMI-2 corium.

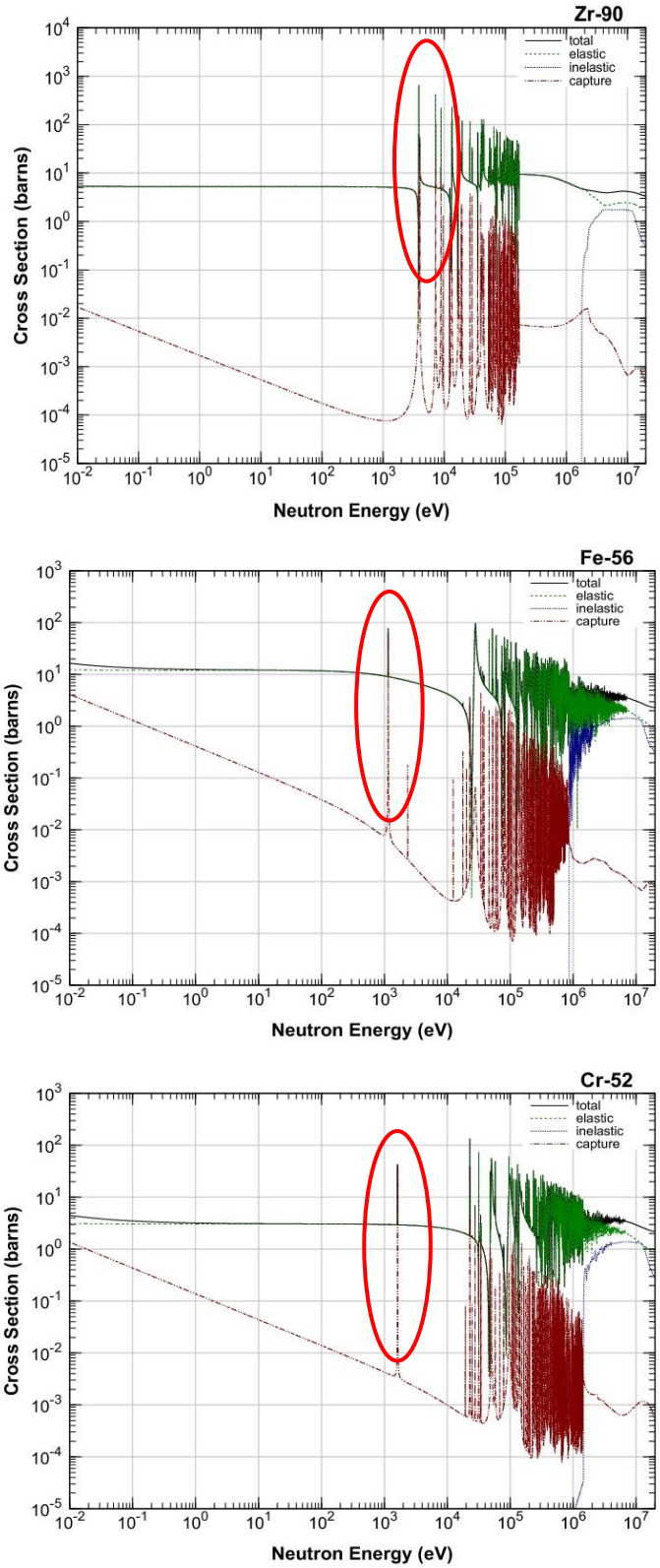

Figure 3.20 Neutron reaction energy spectrum for ^{90}Zr (top), ^{56}Fe (middle) and ^{52}Cr isotopes (bottom).

3.6 Discussion

Referring to the pulsed neutron sources explanation in the introduction part, the larger the pulse width value of a neutron source, the higher the uncertainties of the measurements will be at the higher energy spectrum. That means the error in the TOF measurement and NRTA will likely to increase too. In the case of on-site screening system where it will only perform a qualitative measurement through the detection of isotopes, it is important to set the pulse width for the neutron source to be as short as possible to reduce the error. Based on the past research by KURRI and JAEA, the ideal pulse would be on nanoseconds range, and the compact neutron source in this research operates on 1-4 μs pulse width, capable to reach as short as 500 ns.

The neutron subjected for detection in this research is in the slow neutron area, therefore it is important to choose the right detector for it. The neutron detector chosen to be used in the experiment is ^{3}He as it has the overall good performance, but alternative neutron detector needs to be considered as well when it comes to long-term usage as ^{3}He is getting scarce.

Measurement experiment setup for short-distance neutron TOF is divided into three parts: neutron source part, signal amplifier part, and digital signal processing part. In the neutron source part, the sheet-shaped target measurement material was used and put in front of the detector. Several equipment such as high voltage power source and amplifier is connected to the detector in order to be able to transmit the detected signal. At the digital signal processing part, after both signal coming from the detector and accelerator are matched in the shape and size, their time difference, or neutron's flight time, is calculated. Then, the data can be stored and plotted to neutron TOF plot after conversion into neutron energy spectrum by a Python program.

From the computer simulation of NRTA using this system's short-distance neutron TOF experiment setup, the isotopes of uranium and plutonium, specifically ^{235}U, ^{238}U, ^{239}Pu, ^{240}Pu and ^{242}Pu, the resonance peaks appeared clearly and distinguished enough to be identified. And from the evaluation of the nuclear debris analysis of TMI-2, nuclear fuel debris won't be containing any other elements that has neutron energy absorption in slow neutron area aside from the uranium and plutonium. Therefore, this short-distance neutron TOF NRTA system should be able to clearly identify ^{235}U, ^{238}U, ^{239}Pu, ^{240}Pu and ^{242}Pu isotopes in a nuclear fuel debris.

4. Experiment results

Referring to the experimental setup explained in the previous section, some short-distance neutron TOF NRTA experiment has been performed using the 3.95 MeV X-band electron linac-based neutron source. These experiments are performed at Tokai Campus of The University of Tokyo at Ibaraki, and the results will be explained in this chapter.

4.1 Neutron energy spectrum measurement of 3.95 MeV X-band electron linac-based neutron source

The first experiment is the measurement of neutron spectrum from the pulsed neutron source itself, to confirm the measurement energy range of this isotope detection system. The TOF distance used in this experiment is 2.5 meters with the measurement time of 1 hour. Polyethylene with thickness of 2 cm was put inside the neutron target box as neutron moderator. Obtained neutron spectrum is as shown in figure 4.1 (details of the code for the calculation and plot can be seen at appendix C).

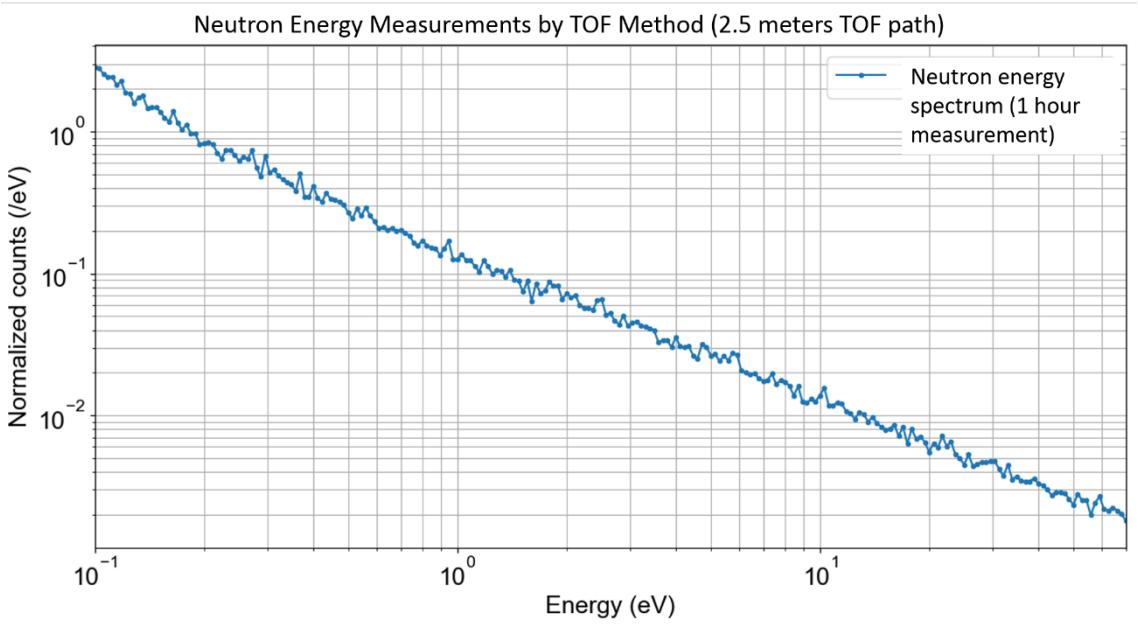

Figure 4.1 Neutron energy spectrum obtained from 3.95 MeV X-band electron linac-based neutron source.

From the result, the observable pulsed neutron spectrum energy range is up to 100 eV. The settings in this experiment serves as default condition and will be the reference for the next Time-of-flight measurement experiments using samples.

4.2 Neutron resonance transmission analysis using ^{3}He neutron detector

The first series of experiments of short-distance NRTA is the one using ^{3}He detector, which is the simplest neutron detector (details of the ^{3}He specifications can be read on the 3rd chapter). ^{3}He has very low gamma/X-ray tolerance, and therefore the detection result shouldn't be significantly affected from gamma burst or X-ray scattering from the pulsed neutron source.

4.2.1 Indium sample

The first sample measurement experiment is using indium. It was chosen because one of its isotopes, ^{115}In, has similar characteristics with one of the plutonium isotopes, ^{240}Pu, according to references from JENDL. The similarities came from their neutron absorption energy which both happen at the 0.1~10 eV energy range within the relatively same total cross-section number as well. Their major neutron absorption happens at approximately 1.5 eV, where the total cross-sections for this energy value is within 10^{4} barns. These characteristics would make indium to be a good dummy sample to test plutonium detection inside nuclear debris using the compact neutron source. Shown in figure 4.2 is the plot of ^{115}In total cross-section reference from JENDL[20].

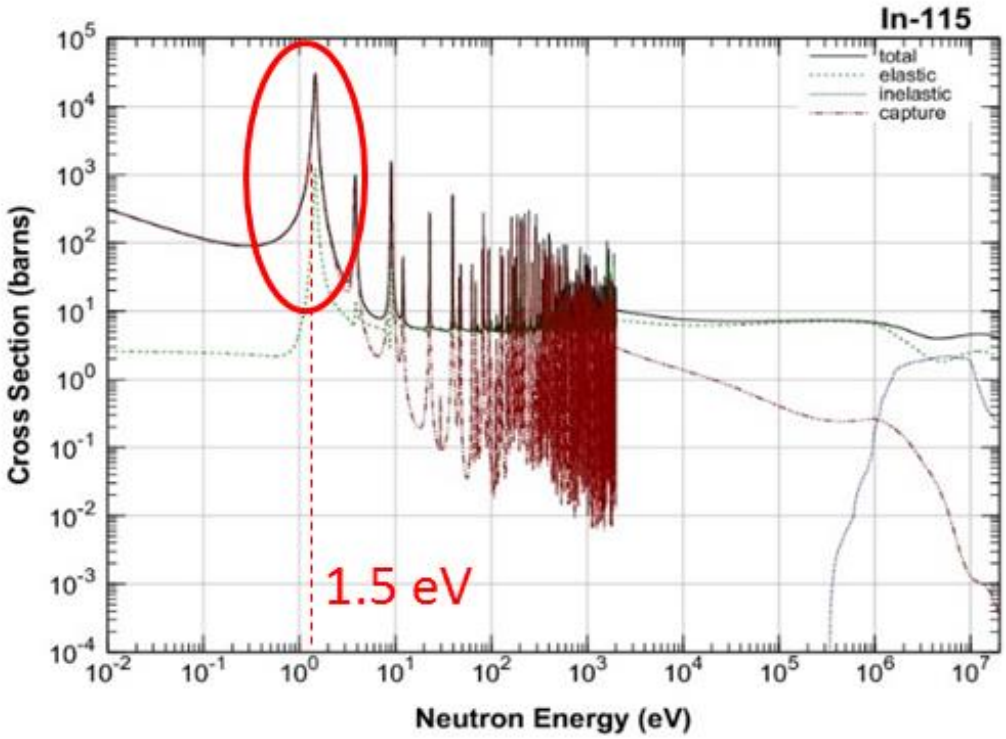

Figure 4.2 Neutron reaction energy spectrum for ^{115}In from JENDL reference.

Indium sample used in this measurement has thickness of 0.3 mm and was put in the distance 50 mm away from ^{3}He detector (picture of this experiment setting can be read at chapter 3). Obtained neutron spectrum of this measurement is shown in figure 4.3.

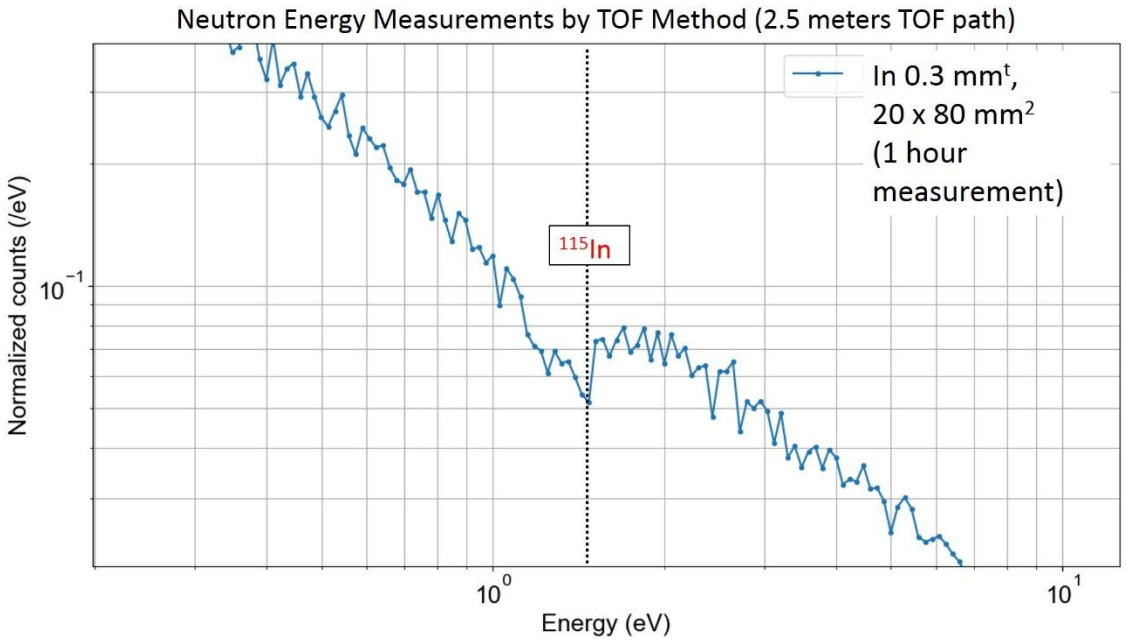

Figure 4.3 Neutron energy spectrum obtained from 1-hour measurement of indium sample.

A resonance peak can be observed around the 1.5-1.8 eV value of the energy axis, which supposedly belongs to one of the indium's isotope. This value matched with the reference from JENDL where the highest neutron absorption value of ^{115}In is at 1.5 eV[14].

4.2.2 Tungsten sample

The next sample for the experiment of preliminary NRTA measurement is tungsten, which was chosen for the similar reason as indium. In tungsten's case, its isotopes' neutron absorption energies and total cross-sections are similar to that of uranium isotope, ^{238}U. Their absorption energies are between 10~50 eV within 10^3 barns total cross-section. These similarities will make tungsten isotopes ideal as material to simulate uranium detection inside nuclear debris using the short-distance NRTA. Shown in figure 4.4 is the plot of ^{238}U and tungsten isotopes (^{186}W, ^{180}W, ^{182}W, ^{183}W) total cross-section reference from JENDL[20].

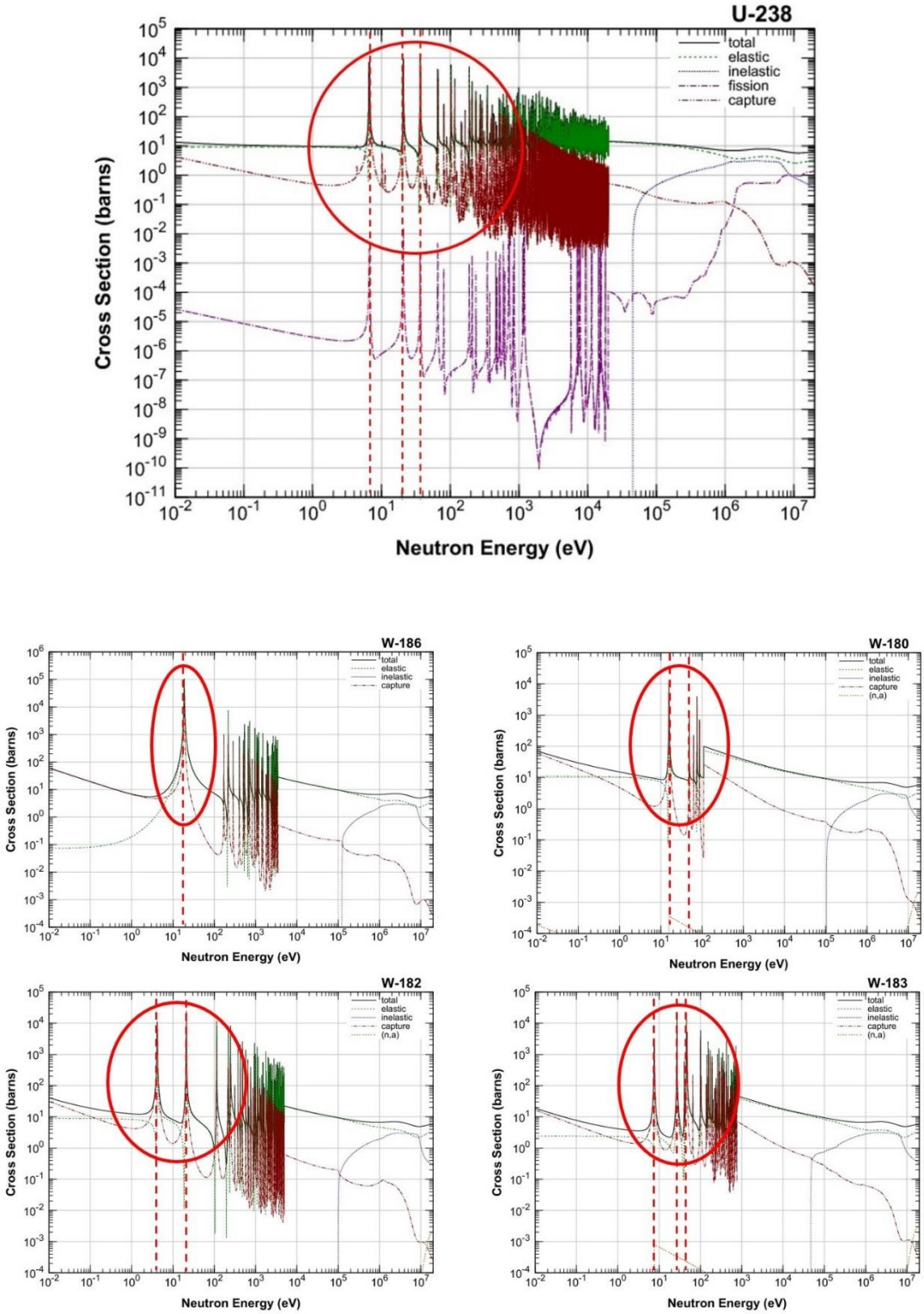

Figure 4.4 Neutron reaction energy spectrum for ^{238}U (top) and tungsten isotopes of ^{186}W, ^{180}W, ^{182}W, ^{183}W (bottom).

The tungsten sample's thickness used for the measurement was 0.3 mm as well, and the obtained neutron spectrum of this measurement for 1 hour is as shown in figure 4.5.

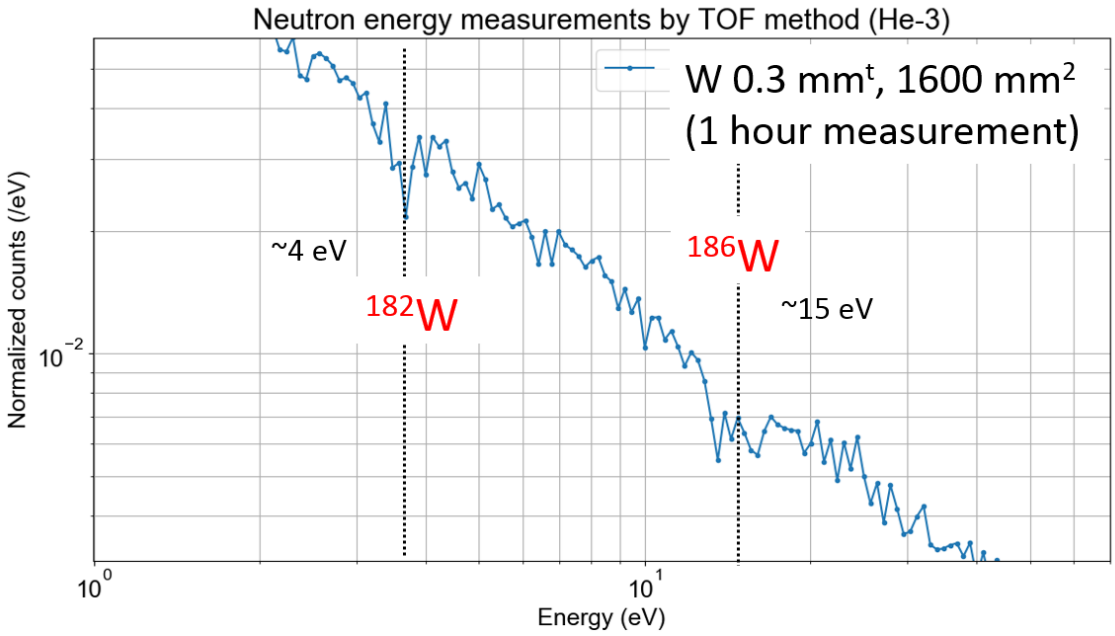

Figure 4.5 Neutron energy spectrum obtained from 1-hour measurement of tungsten sample using ^{3}He neutron detector.

Neutron spectrum obtained from the measurement of tungsten sample shows resonance peak at the energy value around 4 eV and 15 eV. This value matches the references from JENDL for isotopes ^{182}W and ^{186}W[20], and it proves that isotopes with similar neutron energy absorption with Uranium isotope (specifically, ^{238}U) can be detected with this system.

4.3 Neutron resonance transmission analysis using Eu:LiCAF neutron detector

As an alternative to ^{3}He detector, scintillator detector with photomultiplier is used. The scintillator used in this experiment is Eu:LiCAF, which contains lithium as the main neutron detector element. Theoretically, lithium is more sensitive in detecting neutron compared to ^{3}He gas. While still using the same setup as previous experiments, the

detector is now replaced and lead blocks were put as gamma-ray shielding, since scintillator detector is more sensitive to scattered X-ray from the neutron source.

4.3.1 Tungsten sample

The same 0.3 mm tungsten sheet used in the previous experiment was used for a 1-hour measurement using Eu:LiCAF scintillator neutron detector. The TOF plot is shown in figure 4.6.

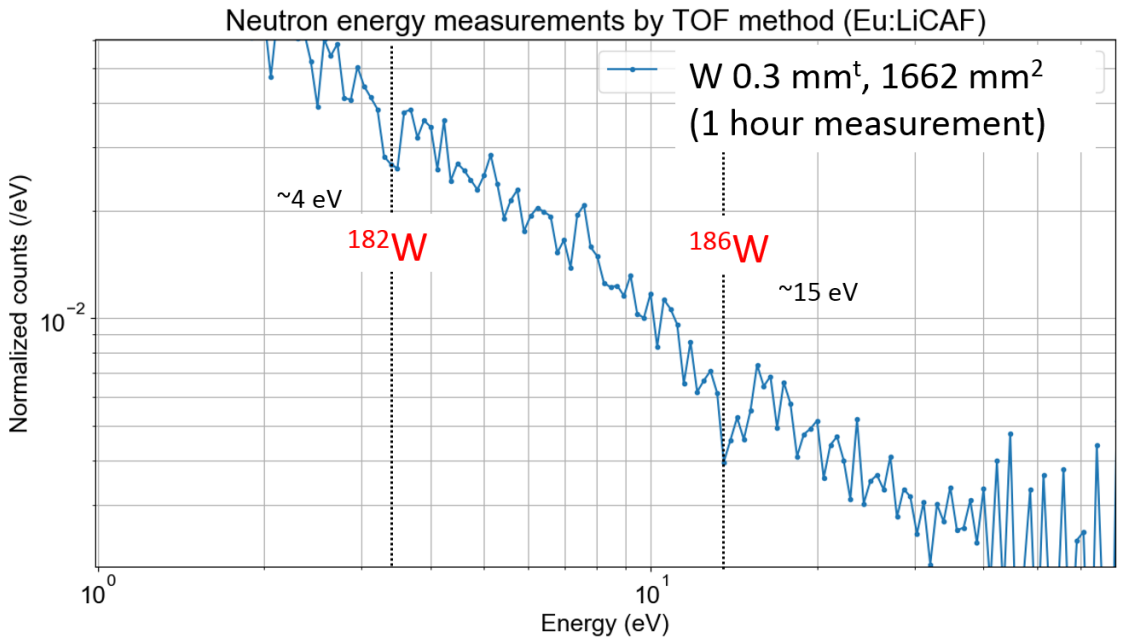

Figure 4.6 Neutron energy spectrum obtained from 1-hour measurement of tungsten sample using Eu:LiCAF scintillator neutron detector.

The measurement result shows that Eu:LiCAF scintillator can be used to measure the neutron TOF in short-distance NRTA system as well. Neutron spectrum obtained from this measurement of tungsten sample shows resonance peak at the same energy value as the one obtained from ^{3}He neutron detector. However, in general, the obtained neutron spectrum by Eu:LiCAF has higher fluctuation for the same duration of measurement, and more noise at the higher energy spectrum.

After the measurement using two kinds of neutron detector, the comparison between the obtained results can be discussed. In terms of the measured neutron spectrum, there

is almost no difference between the shape of the plot and resonance peak's depth. It can be assumed that the peak's depth doesn't depend on the sensitivity of the detector. In terms of setup, both detectors are equal on the adjustment of the gain, comparator, etc., to obtain the same spectrum. However in this measurement, Eu:LiCAF seems to suffer more from the high fluctuation and noise in the spectrum, likely coming from electronic and RF. This is causing the neutron counts with Eu:LiCAF to be only half that of ^{3}He detector. Therefore, from this discussion, it is decided that ^{3}He would be the best detector for the current neutron source and NRTA setting.

4.4 Neutron resonance transmission analysis for mixed sample

This experiment used the same indium and tungsten pure metal sheet as sample just like in the previous experiments, but this time, the measurement for both is simultaneous. The purpose is to simulate the actual condition of the nuclear debris where uranium, plutonium, and other elements will be mixed together. The previous 0.3 mm thick indium and tungsten sheet were combined into 0.6 mm, each different material sheet stacked into each other, where indium sheet facing outside will be exposed by neutron first.

As discussed in the previous short-distance NRTA experiment results, in this simultaneous measurement experiment, the neutron detector used will be ^{3}He neutron detector. Additionally, the relation between measured sample size and measurement time will be investigated. To determine whether the resonance peaks can still be observed when the sample is smaller than the detection area, and closer to solid block rather than sheet, measurements using different sample size and thickness were used. While gradually decreasing the size and increasing the thickness, 1-hour NRTA on each of them were performed. This way, the minimum size and weight of the measurable samples by using 3.95 MeV X-band electron linac-based pulsed neutron source system can be determined.

4.4.1 Indium and tungsten mix sample: Large size

The first combined sample size for the indium and tungsten simultaneous measurement is $20\times80\times0.6$ mm^3, where the detection area size is the same as detector's window. TOF plot of the measured result is shown in figure 4.7.

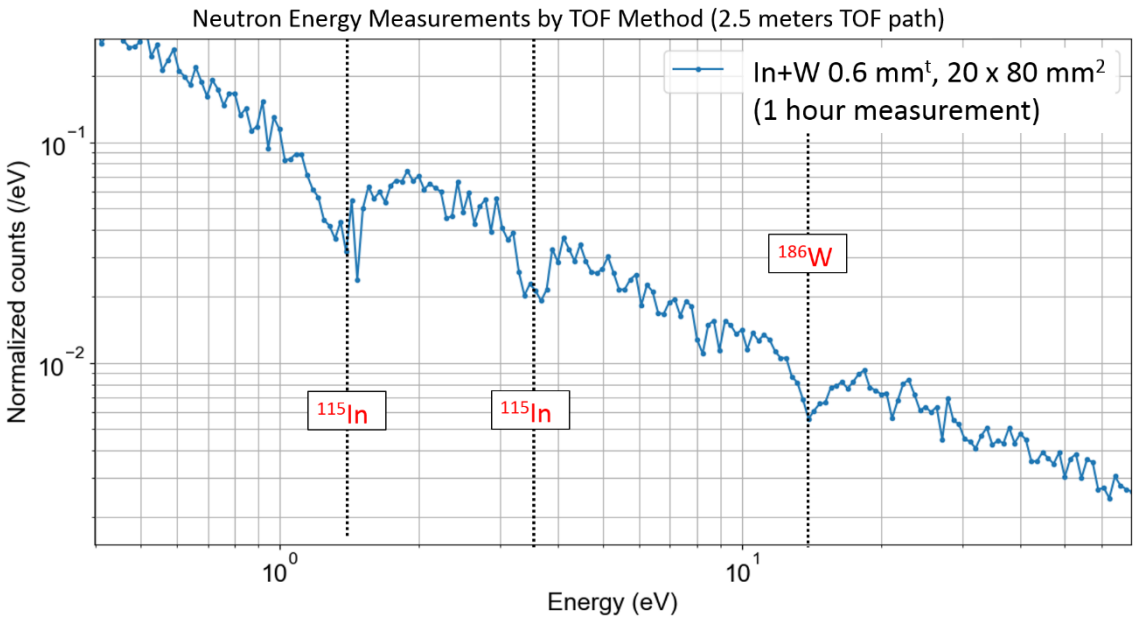

Figure 4.7 Neutron energy spectrum obtained from 1-hour measurement of indium and tungsten combined sample using ^{3}He neutron detector for 20×80×0.6 mm^3 sample size.

4.4.2 Indium and tungsten mix sample: Small size

The second combined sample size for the indium and tungsten simultaneous measurement is 20×20×1.2 mm^3. This time the size is reduced to be smaller than the detector area, and made thicker, to simulate the typical nuclear debris size mentioned at the introduction.

From this measurement, it was found that when using smaller sample area, the resonance peak will be more difficult to observe from the 1-hour measurement TOF spectrum. Therefore, to lessen the fluctuation in the spectrum, the measurement time needs to be extended into 2 hours. Plot of the measured result is shown in figure 4.8.

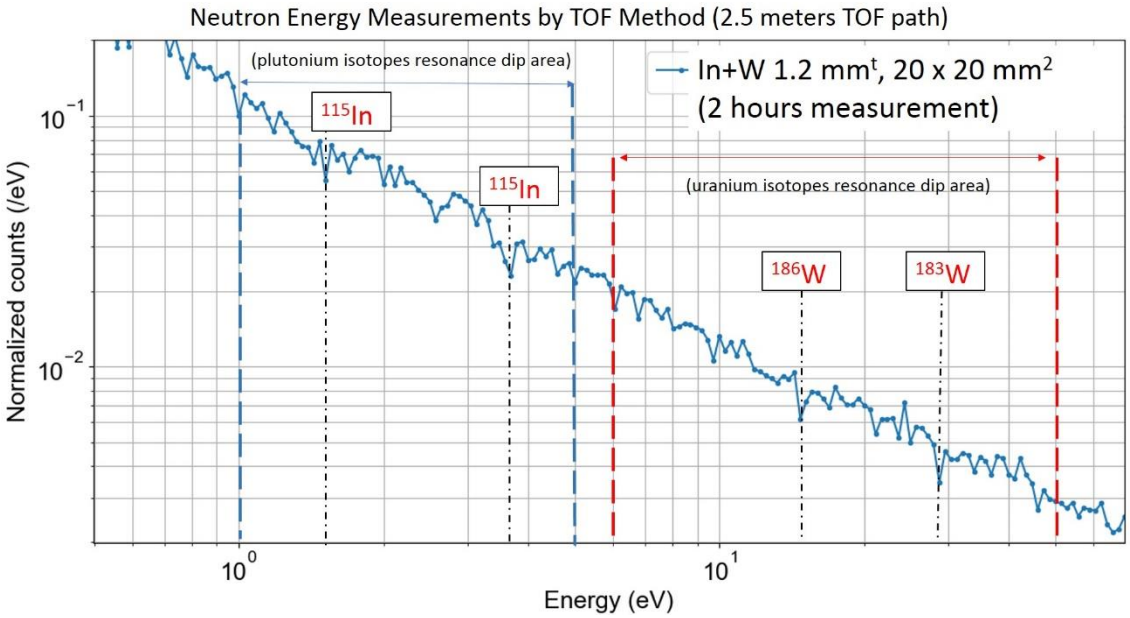

Figure 4.8 Neutron energy spectrum obtained from 2-hours measurement of indium and tungsten combined sample using ^{3}He neutron detector for 20×20×1.2 mm^3 sample size.

By comparing the resonance result from the experiment with the one from simulation, it is proved that this system can possibly be used to detect the U/Pu isotopes with distinguished resonance peaks' location between them.

4.4.3 Energy resolution calculation for compact TOF system with ^{3}He detector

Energy resolution of a TOF system is related to the time resolution, or the overall time dispersion divided by flight path lengths. It stems from flight path uncertainties due to the size of the sample and detector geometry, and the intrinsic time resolution of the detector. To calculate the energy resolution, the following formula in equation (14) is used.

$$\frac{\Delta E}{E} = \frac{2}{L}\sqrt{\frac{E}{\alpha^2}\Delta T^2 + \Delta L^2} \tag{14}$$

ΔE/E is the energy resolution, L is the flight path length, and α is time of flight of a 1 eV neutron to cover a distance of 1 m, where it is a constant of 5227.039$^{1/2}$[60]. The ΔT or TOF

uncertainty is mainly affected by linac pulse width and neutron detector delay time. ΔL is flight path uncertainty, which can be calculated through equation (15).

$$\Delta L = \sqrt{L^2 + h^2} - L \tag{15}$$

In this equation, h is the half of the detector's length. Therefore, the uncertainty in flight path is mainly affected by detector's geometry. By using these equations and observing neutron energy of interest where resonances happen, the energy resolution of this short-distance NRTA system can be calculated. The calculation results are shown in table 4.1.

Table 4.1 Energy resolution of short-distance 2.5 meter TOF for neutron energies of interest.

Neutron energy (eV)	Pulse width (μs)	L (m)	h (m)	ΔT (μs)	ΔL (m)	ΔE/E
1.37	2.5	2.5	0.015	2.5	3.05E-02	3.24%
3.55	2.5	2.5	0.015	2.5	3.05E-02	5.21%
14.20	2.5	2.5	0.015	2.5	3.05E-02	10.42%

Compared to the large TOF facility with a long flight path and a neutron source pulse width of 1 ns with the energy resolution value of 1%[61], our system's energy resolution seems reasonable. Given that the measured TOF is in microseconds order, even with 4%~10% energy resolution, it is still within the separation border of uranium and plutonium resonance peak area. Therefore, the formed resonance peaks should still be able to be identified as either uranium or plutonium.

4.4 Discussion

From the experiments on short-distance neutron TOF, it proves that the 3.95 MeV X-band electron linac-based neutron source can perform a neutron TOF measurement from only 2.5-meter distance, where it gives the observable neutron energy spectrum up to 100 eV. The NRTA experiment using dummy material indium, which neutron energy absorption value is relatively low with high neutron cross-section, gives a good start by having a significant resonance peak happened at the accurate reference value with only 1 hour of measurement.

The next experiment is using tungsten sample, which was chosen because its isotope's (^{186}W) similarity with ^{238}U in the terms of neutron energy absorption and neutron cross-section. The resonance peak of ^{186}W can be observed in this experiment as well. In the measurement using Eu:LiCAF detector, the highly-fluctuated detection result shows that ^{3}He would be the best neutron detector for the current setting. It has also successfully identified multiple isotopes simultaneously in a measurement through the sample of indium and tungsten mix, with the smallest sample size being 20×20×1.2 mm^3.

Resonance peak's resolution, as well as energy resolution still has room for improvements, but for now the short-distance neutron TOF measurement system is feasible for the clarification of uranium and plutonium contents in nuclear debris, through the isotopes detection of ^{238}U, ^{235}U, ^{239}Pu, ^{240}Pu and ^{242}Pu. These experiment results show that 3.95 MeV X-band electron linac-based compact neutron source can be used in detecting several different isotopes in a mixed sample, which is close to the actual condition of the nuclear debris that contains various materials in it.

5. Proposal and scheme of the on-site neutron and X-ray combined analysis

The main objective of this research is to make a meaningful contribution to criticality calculations for nuclear debris containers, via the determination of uranium and plutonium material density. Therefore, the schematic and plan of the practical application of on-site screening system consisting the utilization of neutron and X-ray combined method will be explained in this chapter. It will also give a better understanding about the role of each method in the system, and how short-distance NRTA method will complement the X-ray CT method.

5.1 Nuclear debris storage and its criticality calculation

Based on the second phase of the nuclear debris removal project, the debris will be contained in large canisters to be transported, which means it is at risk of criticality problem. Figure 5.1 shows the schematic plan of the canister to contain 1F nuclear fuel debris by IRID[11]. The canisters will contain several smaller unit cans that will be stacked inside it. Target of the criticality calculation is the unit cans, which will be filled with screened nuclear debris and separated based on its U/Pu concentration. The unit cans with higher U/Pu concentration will undergo more detailed content analysis before they are stored within the canisters.

Criticality of contained nuclear material is related to multiplication factor as eigenvalue (keff). It is obtained through the ratio between neutron production and absorption in fission, shown in equation (16). The value of $k_{eff} < 1$ means that the container is subcritical, which is the normal condition, where $k_{eff} = 1$ means critical condition reached and $k_{eff} > 1$ means supercritical where neutron production exceeds the absorption process.

$$k_{eff} = \frac{neutron\ produced\ in\ fission}{neutron\ absorbed\ in\ fission} \tag{16}$$

Keff is related to macroscopic cross-section, and macroscopic cross-section is calculated from the material density information, which needs the weight and size of the said fissile material. The formula for macroscopic cross-section is shown in equation (17).

$$\Sigma = \sigma \cdot N \tag{17}$$

$\boldsymbol{\Sigma}$ is macroscopic cross-section, and σ is microscopic cross-section which values are fixed for each isotope. N is density, which can be calculated through the following formula shown in equation (18).

$$N = \frac{n}{V} = \frac{\rho \cdot N_A}{M} \tag{18}$$

Where N_A is Avogadro number, M is molecular weight, and ρ is the material density (g/cm^3). The information of ρ is the one that will be obtained from the nuclear debris screening result.

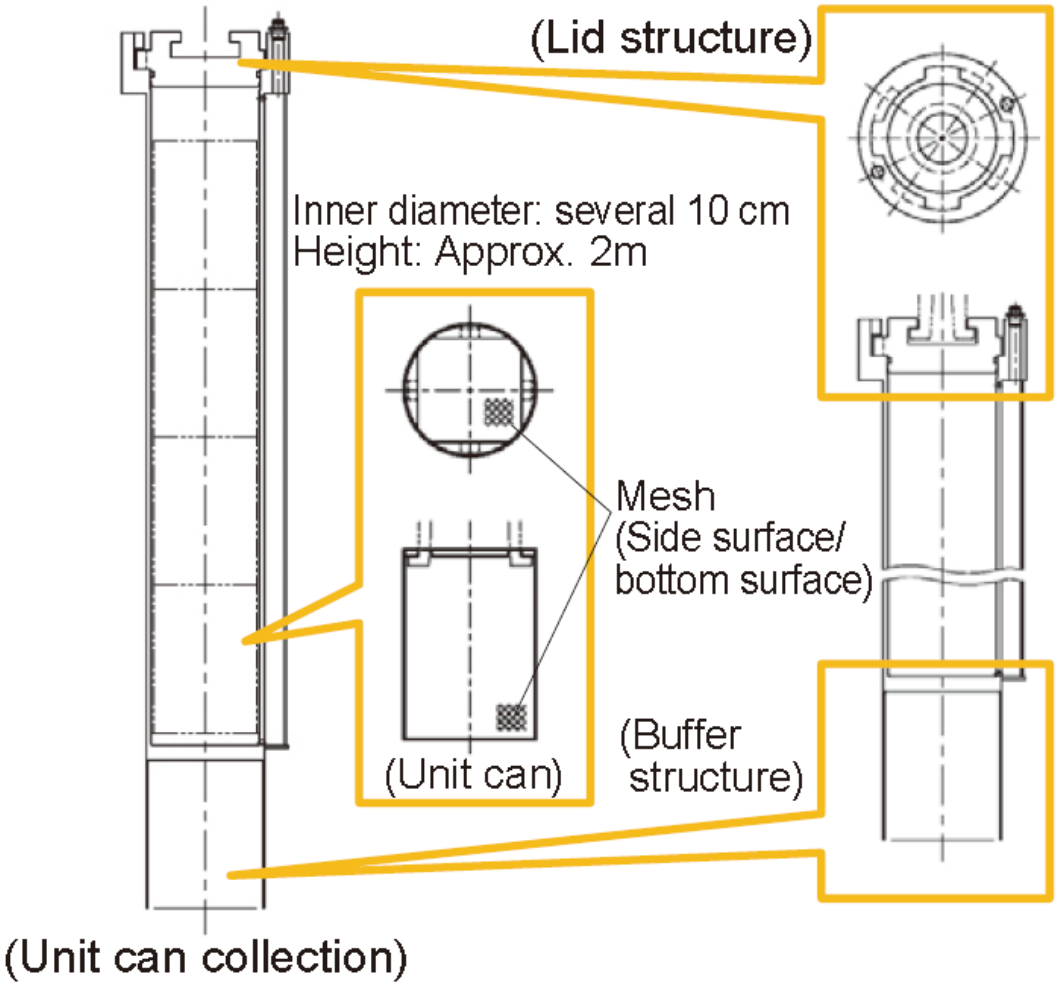

Figure 5.1 Schematic of the nuclear debris storage canister incorporated by IRID.

5.2 Flow of preliminary screening activity

Short-distance NRTA will complement X-ray CT system in the study nuclear debris with on-site screening. The flow of screening activity using the combination of both methods can be seen in figure 5.2. X-ray CT can be used to estimate the size and weight of the uranium and plutonium content in the debris, which is necessary for material density calculation. After that, the existence for uranium and/or plutonium will be confirmed through short-distance NRTA method, to correct the X-ray screening result. Due to its limited sample shape for measurement and long measuring time, for the consideration of practical use of the screening system, this short-distance NRTA will be used at the test extraction step for the purpose of system calibration.

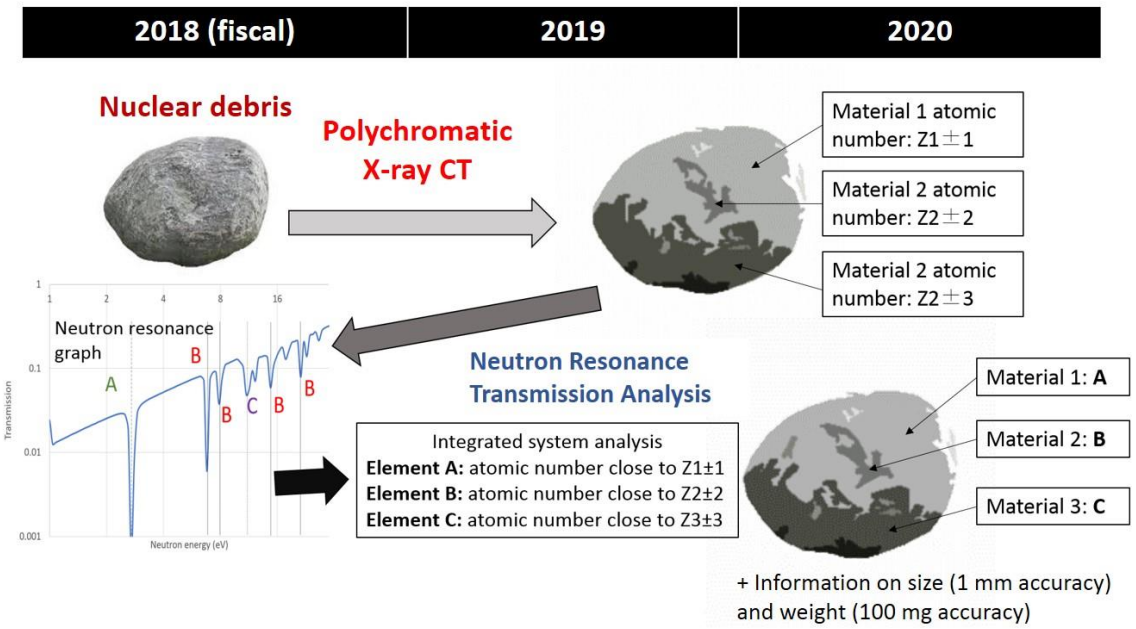

Figure 5.2 Flow of the preliminary screening activity of nuclear debris.

5.3 NRTA as complementary to X-ray CT screening system

While X-ray can do imaging and measure the size of the respective materials, it has the downside of difficulty in getting accurate identification of elements with close Z number. This will be a problem in distinguishing uranium and plutonium in measured nuclear debris (atomic number of U: 92, Pu: 94). Uranium and plutonium have very different microscopic cross-section (σ) value, where σPu > 200 σU. Plutonium is more

reactive and prone to reach critical condition faster, so uranium and plutonium storage need to be separated. Therefore, NRTA is needed with the purpose of determining the existence of uranium and plutonium with higher accuracy to complement the X-ray CT imaging of the respective measured nuclear debris.

5.4 Rapid line detector system for debris extraction

For practical use, short-distance NRTA will be used at the test extraction step and system calibration. Actual screening process during mass extraction will utilize fast line detector system by polychromatic X-ray CT, which is a faster measurement method for nuclear debris samples. When mass extraction of nuclear debris happens, the actual screening process will be conducted by a fast line detector system by polychromatic X-ray CT of partial angle and parallel motion that is able to do the measurement faster for several nuclear debris samples. The schematic of this rapid line detector system is shown in figure 5.3, along with how it contributes in the criticality estimation before proceeding to nuclear debris storage.

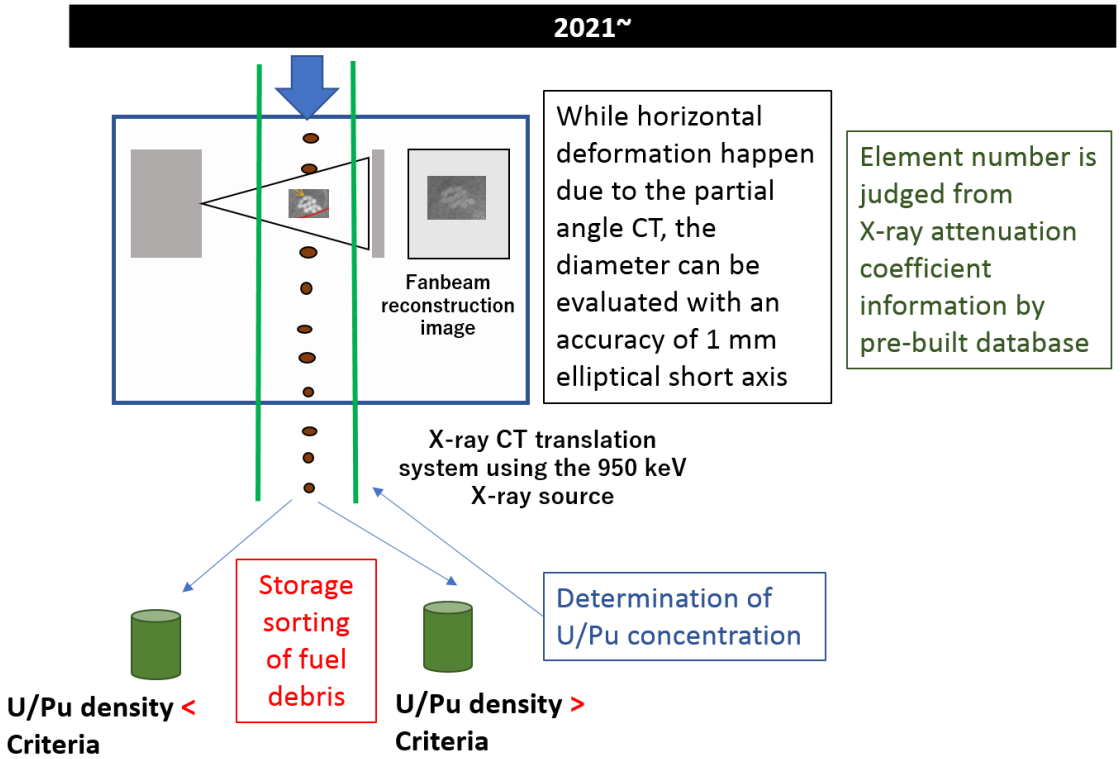

Figure 5.3 Rapid line detector system for nuclear debris mass-extraction and storage.

In the current stage of development, artificial elongation of reconstructed image happens due to the partial angle CT. This error has been evaluated for the X-ray bridge inspection and the diameter of reinforced iron wires and rods can be estimated with the spatial resolution of 1 mm[37][62]. The same treatment is planned to be introduced for the next step of development for the practical design.

6. Conclusion and future developments

6.1 Conclusion

After the Fukushima Daiichi nuclear reactor incident, as part of its decommissioning project, the nuclear fuel debris from the reactor core needs to be removed for the purpose of safeguards and criticality safety. Before a thorough debris removal plan is made, the condition of the nuclear debris distribution inside the PCV must be investigated through nuclear debris activity mapping. In order to get the data of the nuclear debris for the effective and efficient mapping activity, an on-site nuclear debris screening activity needs to be performed. This screening activity will consist of two different methods that complements each other: polychromatic X-ray CT and short-distance NRTA.

The latter method, which is the main theme of this research, is a method to identify isotopes inside a material. NRTA method has been widely used in nuclear data analysis by using high-energy neutron sources in various accelerator facility in the world, and the short-distance TOF NRTA introduced the compact, mobile version of it for the purpose of on-site screening of nuclear fuel debris. Unlike the normal NRTA that can detect wide range of isotopes, this compact system will only detect ^{238}U, ^{235}U, ^{239}Pu, ^{240}Pu and ^{242}Pu, which are necessary for the data of nuclear debris activity mapping.

By using X-band electron linac coupled with photon and neutron converter, a compact pulsed neutron source with high mobility can be constructed for the purpose of short-distance neutron TOF measurement and performing NRTA of the nuclear debris content. From the experiment result using 3.95 MeV X-band electron linac with tungsten as photon converter and beryllium as neutron converter, an NRTA experiment can be performed to detect neutron resonance peak in the energy range 1-100 eV through only 2.5-meter TOF path, which is within the energy range of neutron energy absorption value for ^{238}U, ^{235}U, ^{239}Pu, ^{240}Pu and ^{242}Pu. The experiments using tungsten as dummy sample with the closest neutron energy absorption value with ^{238}U, as well as multiple isotopes identification, has been done successfully and shows the capability of short-distance TOF method to perform NRTA of specific neutron energy range within the slow neutron area. It proves that this system is feasible to confirm the existence of uranium and plutonium content inside nuclear debris, through the isotopes detection of ^{238}U, ^{235}U, ^{239}Pu, ^{240}Pu and ^{242}Pu.

With its compact size and short TOF path, this advantage will make the system able to be implemented in on-site nuclear debris screening system and perform isotope identification system at Fukushima Daiichi nuclear reactor, as a complementary to increase the accuracy of polychromatic X-ray CT imaging method. Combination of these two measurement methods will be used to obtain nuclear debris composition data necessary for nuclear debris activity mapping of Fukushima Daiichi reactor core area, as well as nuclear debris storage criticality control.

6.2 Improvement and future development

6.2.1 NRTA using realistic model nuclear fuel debris

In order to get more realistic measurement data, a model debris was made to mimic Fukushima fuel debris using non-radioactive materials, and it was also planned to be used for the NRTA experiment with the current compact neutron source. The first sample of nuclear debris has been made successfully by the Heavy Irradiation Research Management Department, The University of Tokyo. This model nuclear debris consists of zirconium and iron (stainless steel), pictured in figure 6.1.

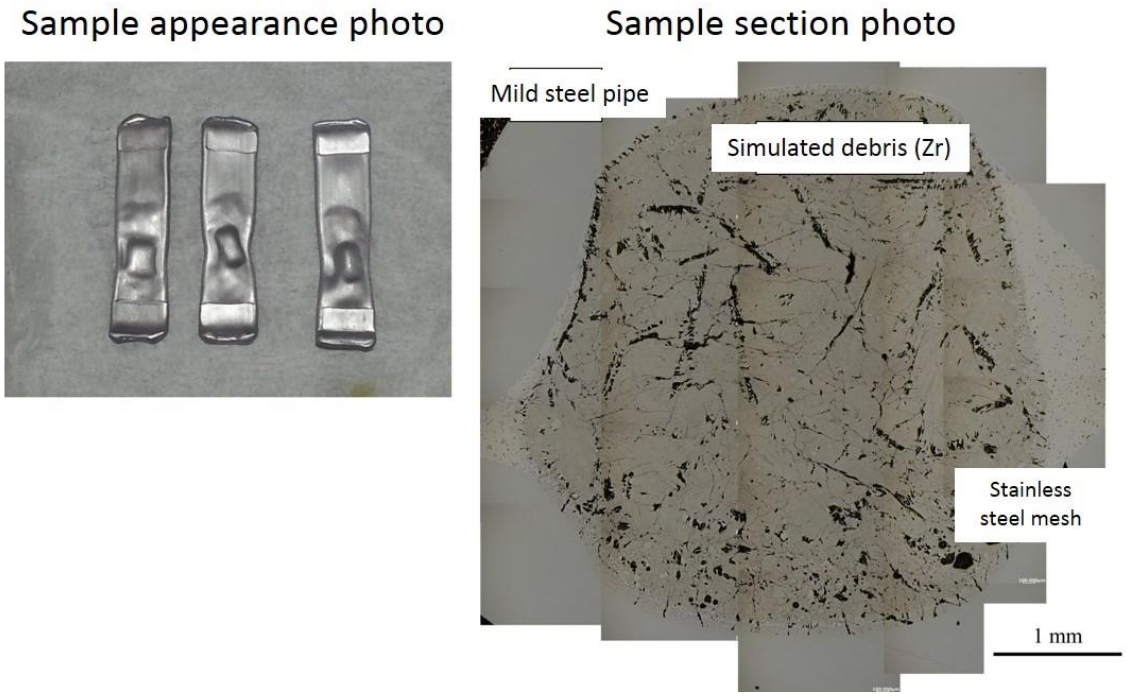

Figure 6.1 Simulated nuclear fuel debris model (incorporated by Dr. Kano Sho, et al).

As the neutron energy absorption value of Zr and Fe is outside of the range of compact electron linac-based neutron source used in this research, the model nuclear debris to be used for the experiment needs to have material with the neutron energy absorption similar to that of ^{238}U, ^{235}U, ^{239}Pu, ^{240}Pu and ^{242}Pu. The next fabrication of model nuclear debris is planned to have these materials included in the mixture, which

could be tungsten, indium, or any of the material used in the NRTA experiment of this research.

Related to the matter of realistic model nuclear debris sample, the molar ratio between U/Pu model needs to be considered as well. As the actual nuclear debris will have different molar ratio between its contained uranium and plutonium, it might affect the NRTA measurement sensitivity.

Other model debris sample option is the one containing actual uranium, within the regulated amount permitted. By using the model nuclear debris containing actual uranium incorporated by The University of Sheffield and/or JAEA, we can do a realistic model nuclear debris measurement using this compact nuclear debris screening system. In the near time, focus of the next experiment will be on how to perform NDA successfully on the available nuclear debris sample shape. As this research isn't constrained to field practical application time, longer measurement time shall be the option to obtain better neutron spectrum with less fluctuation.

6.2.2 Nuclear debris sample size adjustment for measurement

Based from the explanation regarding nuclear debris type chapter 1, the actual powder-type nuclear debris size will be much smaller and three-dimensional. Meanwhile, with the current experiment parameters and setting, the smallest measurable debris size is 20×20×1.2 mm^3. The simplest way that could possibly be performed next to anticipate this is by using a film to put powder debris inside it instead. If a film of size 20×20×1.2 mm^3 is used, several nuclear debris can be placed into the said film as a sample placeholder, to fulfill the minimum required sample area.

6.2.3 Utilization of 30 MeV linac to increase neutron intensity

It is not easy to do fast measurement on-site by 3.95 MeV. Instead, there is an option to install 30 MeV linac in a certain facility near 1F site and perform NRTA in short time. Neutron intensity enhancement of the four order (3.86×10^7 to 8×10^{11} n/s) can be achieved by using 30 MeV X-band linac on the neutron source system. Based on the calculation on improvement estimation shown in table 6.1, it enables detection of uranium and plutonium in a few mm fuel debris within order of ten seconds.

Table 6.1 Improvement estimation on measurement time and sample size with 30 MeV X-band linac

	3.95 MeV		**30 MeV (estimation)**
Sample size	20 x 80 x 0.6 mm^3	20 x 20 x 1.2 mm^3	5 x 5 x 5 mm^3
Measurement time	1 hour	2 hours	~5.8 seconds

6.2.4 Optimization of experiment parameters and settings

Simulating and/or experimenting another experiment setup to produce sharper resonance peak for easier observation in smaller sample will be one of the plans for future improvement of this system. Improvement on neutron intensity that includes the following options: Neutron target (beryllium) size modification, using shorter neutron source's pulse width, and linac power capacity increase up to 2 MW. The use of collimator around detector area to increase detected neutron count and opening the possibility to use smaller debris size for the measurement sample.

As the flux of the neutron generated by this compact neutron source is quite low, the amount of the neutron reaching the detector might be even lower when the measurement is performed in open atmosphere. Therefore, one of the solutions to make the result of the NRTA measurement better is to apply neutron collimator. Another is to make the measurement time longer to increase the detected neutron count and reduce fluctuation in the obtained spectrum.

While the 2.5 meters TOF path distance used in here is already able to detect the uranium and plutonium isotope, it is also due to the space limitation of the experiment area. Theoretically, the energy resolution for the area above 50 eV can still be improved by optimizing the distance of the TOF path up to 5 meters, to keep the compactness of the system. Additionally, ^{3}He neutron detector has a time delay at both ends of each cathode during the neutron detection process. This issue shall be addressed as well, since it might affect the energy resolution calculation of the TOF system.

Aside from the neutron target and experiment setting, the calculation of gamma and X-ray radiation intensity leaking from the X-ray source and/or beryllium might need to be considered as well.

Appendix A. PHITS simulation code of 3.95 MeV X-band electron linac-based compact neutron source

```
[ T i t l e ]
Beryllium compact neutron source - X-Ray source 3.95 MeV

[ P a r a m e t e r s ]
$ mode
$ 7: t-gshow, 11 t-3dshow
$ 5: Source Check
icntl = 0

$ event number
maxcas = 1.0E5

$ batch number
maxbch = 1.0E3

itall = 1
istdev = -1

$ 2: neutron, 12: electron, 14: photon
emin(2)  = 1.0E-15
emin(12) = 1.0E-1
emin(14) = 1.0E-3
emin(13) = 1.0E-1

dmax(2)  = 20.0
dmax(12) = 20.0
dmax(14) = 20.0
dmax(13) = 20.0

$ considering photo nuclear reaction
ipnint = 1

$ Coulomb scattering
nspred = 1

$ Energy straggling of charged particle
nedisp = 1

$ Use egs5 for photon&electron
negs = 1

$ considering gamma
igamma = 1

$ bias the photo-nuclear reaction cross section
$ pnimul = 1.0

$ reading source file from dump
$ idmpmode = 1

$ event generator mode
e-mode = 2
```

```
file(6) = phits.out
file(7) = C:\phits\data\xsdir.jnd
file(14) = C:\phits\data\trxcrd.dat
file(20)= C:\phits\XS\egs

$------------------------------------------------------------------------
[ S o u r c e ] #put the photon file in here
s-type = 19 #cone beam shape from 15 cm distance
proj = photon
x0 = 0.0
y0 = 0.0
z0 = 27.5
x1 = 0.0
y1 = 0.0
z1 = 27.5
r1 = 1.0
r2 = 0.0
dir = -1.0
dom = 17.066

e-type = 1
ne = 61
1.2026E-03  7.6099E-06
1.3738E-03  3.7318E-06
1.5693E-03  4.4240E-06
1.7926E-03  8.2600E-06
2.0477E-03  3.0861E-06
2.3391E-03  6.0662E-06
2.6719E-03  2.7302E-05
3.0521E-03  5.5037E-05
3.4865E-03  6.8892E-05
3.9826E-03  9.3019E-05
4.5494E-03  1.5870E-04
5.1967E-03  1.5704E-04
5.9363E-03  4.1759E-04
6.7810E-03  5.3381E-04
7.7460E-03  6.6454E-04
8.8482E-03  2.7087E-02
1.0107E-02  5.0606E-03
1.1546E-02  2.5413E-04
1.3189E-02  2.9960E-04
1.5065E-02  3.8599E-04
1.7209E-02  5.8917E-04
1.9658E-02  8.7340E-04
2.2456E-02  1.4465E-03
2.5651E-02  2.0861E-03
2.9302E-02  3.1913E-03
3.3471E-02  4.9044E-03
3.8234E-02  7.4898E-03
4.3675E-02  1.0878E-02
4.9890E-02  1.7512E-02
5.6990E-02  2.6179E-02
6.5100E-02  4.6981E-02
7.4364E-02  5.3179E-02
8.4946E-02  6.1614E-02
9.7034E-02  7.1884E-02
1.1084E-01  7.6564E-02
```

```
1.2662E-01  8.0121E-02
1.4463E-01  8.1396E-02
1.6522E-01  8.2418E-02
1.8873E-01  8.2325E-02
2.1558E-01  7.9603E-02
2.4626E-01  7.7905E-02
2.8130E-01  7.5236E-02
3.2133E-01  7.2100E-02
3.6706E-01  6.9148E-02
4.1930E-01  6.6025E-02
4.7896E-01  6.0637E-02
5.4712E-01  5.9067E-02
6.2498E-01  5.3268E-02
7.1392E-01  4.9970E-02
8.1551E-01  4.6221E-02
9.3156E-01  4.2739E-02
1.0641E+00  3.9166E-02
1.2156E+00  3.4360E-02
1.3885E+00  3.0528E-02
1.5861E+00  2.6769E-02
1.8118E+00  2.2543E-02
2.0697E+00  1.8509E-02
2.3642E+00  1.4409E-02
2.7006E+00  1.1060E-02
3.0849E+00  7.2538E-03
3.5239E+00  3.7588E-03
4.0254E+00  6.8365E-04

$-----------------------------------------------------------------------
[ M a t e r i a l ]
$   Air at ground level  1.21e-3 g/cm^3
mat[11] 14N 4.0586E-05
        16O 1.0800E-05
        40Ar 2.4255E-07

$   W 19.25 g/cm^3
mat[1] 180W 0.12
       182W 26.50
       183W 14.31
       184W 30.64
       186W 28.43

$   Cu 8.94 g/cm^3
mat[2] 63Cu 69.15
       65Cu 30.85

$   Pb 11.34 g/cm^3
mat[3] 204Pb 0.014
       206Pb 0.241
       207Pb 0.221
       208Pb 0.524

$   BPE 1.00 g/cm3
mat[4] 1H  0.4495
       12C 0.1550
       10B 0.0924
       16O 0.3031
```

```
$   Be 1.85 g/cm^3
mat[6] 9Be 1.0

$-------------------------------------------------------------------
[ Mat Name Color ]
mat   name      color
11    Air       lightgray
1     W         green
2     Cu        red
3     Pb        darkgreen
4     BPE       cyan
6     Be        orange

$-------------------------------------------------------------------
[ S u r f a c e ]
$ Atmosphere around Neutron Source
999 rpp -10000.0 10000.0
        -10000.0 10000.0
        -10000.0 10000.0
$ Atmosphere around target
998 rpp -2.5 2.5
        -2.5 2.5
         2.5 12.5

997 rpp -12.5 -2.5
        -2.5 2.5
        -2.5 2.5

$-----------------------------------------------------------
$-------------- Pb bremsstrahlung converter --------------
100 rpp -12.5 12.5
        -12.5 12.5
        -12.5 12.5
$-----------------------------------------------------------
$-------------- Pb bremsstrahlung converter (small)--------------
900 rpp -10.5 4.5
        -10.5 10.5
        -4.5 4.5
$-----------------------------------------
$-------------- BPE moderator --------------
200 rpp -10.5 10.5
        -10.5 10.5
        -10.5 10.5
$-----------------------------------------------------------------
$-------------- Be photoneutron production target --------------
400 rpp -2.5  2.5
        -2.5  2.5
        -2.5  2.5

[ C e l l ]
$-----------------------------------------------------------
$-------------- Outer void --------------
$ Outer void
99999 -1 999

$-----------------------------------------
$-------------- Atmosphere --------------
$ Surrounding Atmosphere
```

```
9999 11 -1.21e-3 -999 998 997 #1100 #1200 #1400 #1900
9998 11 -1.21e-3 -998 #1400
9997 11 -1.21e-3 -997

$-----------------------------------------------------------
$-------------- Pb bremsstrahlung converter --------------
1100 3 -11.34 -100 998 997 #1200 #1400 #1900
1900 3 -11.34 -900 998 997 #1400

$-------------------------------------------
$-------------- BPE moderator --------------
1200 4 -1.000 -200 998 997 #1400 #1900

$-------------------------------------------------------------
$-------------- Be photoneutron production target --------------
1400 6 -1.85  -400

$-------------------------------------------------------------------------
[ T - T r a c k ] # photon track
     mesh =  xyz            # mesh type is xyz scoring mesh
   x-type =    2         # x-mesh is linear given by xmin, xmax and nx
       nx =  100            # number of x-mesh points
     xmin =  -30        # minimum value of x-mesh points
     xmax =   30        # maximum value of x-mesh points
   y-type =    2            # y-mesh is given by the below data
       ny =   1            # number of y-mesh points
     ymin =   -30
     ymax =    30
   z-type =    2          # z-mesh is linear given by zmin, zmax and nz
       nz =  100            # number of z-mesh points
     zmin =  -30         # minimum value of z-mesh points
     zmax =   50         # maximum value of z-mesh points
     part = photon
      e-type = 2             # e-mesh is given by the below data
       ne =   1            # number of e-mesh points
      emin =  1.0E-11
      emax =  10.0
     unit =   3            # unit is [1/cm2/Lethargy/source]
     axis =   xz            # axis of output
     file = track_xz_photon.out   # file name of output for axis
    title = Geometry of Photon Track Detection using [T-track] tally
    gshow =    3          # 0: no 1:bnd, 2:bnd+mat, 3:bnd+reg 4:bnd+lat
   epsout =    1            # (D=0) generate eps file by ANGEL
$-------------------------------------------------------------------------
[ T - T r a c k ] # neutron track
     mesh =  xyz            # mesh type is xyz scoring mesh
   x-type =    2          # x-mesh is linear given by xmin, xmax and nx
       nx =  100            # number of x-mesh points
     xmin =  -30        # minimum value of x-mesh points
     xmax =   30        # maximum value of x-mesh points
   y-type =    2            # y-mesh is given by the below data
       ny =   1            # number of y-mesh points
     ymin =   -30
     ymax =    30
   z-type =    2          # z-mesh is linear given by zmin, zmax and nz
       nz =  100            # number of z-mesh points
     zmin =  -30         # minimum value of z-mesh points
     zmax =   50         # maximum value of z-mesh points
```

```
     part = neutron
      e-type =    3             # e-mesh is given by the below data
       ne =   1            # number of e-mesh points
      emin =  1.0E-9
      emax =  10.0
     unit =   3            # unit is [1/cm2/Lethargy/source]
     axis =   xz            # axis of output
     file = track_xz_neutron.out    # file name of output for axis
    title = Geometry of Neutron Track Detection using [T-track] tally
    gshow =    3           # 0: no 1:bnd, 2:bnd+mat, 3:bnd+reg 4:bnd+lat
   epsout =    1            # (D=0) generate eps file by ANGEL
$-------------------------------------------------------------------
[ T - C r o s s ] # photon flux
       title = Energy distribution in region mesh
        mesh =  reg            # mesh type is region-wise
         reg =    1           # number of crossing regions
           non    r-in    r-out     area
           1      9998     1400     25.0
      e-type =    3             # e-mesh is given by the below data
          ne =   100            # number of e-mesh points
        emin =  1.0E-11
        emax =  10.0
      unit =   3            # unit is [1/cm2/Lethargy/source]
        axis =  eng            # axis of output
        file =  cross_photon.out      # file name of output for axis
      output =  flux           # surface crossing flux [1/cm^2/source]
        part =  photon
      epsout =    1            # (D=0) generate eps file by ANGEL
$-------------------------------------------------------------------
[ T - C r o s s ] # neutron flux at Be surface
    title = Energy distribution in region mesh
     mesh =  reg            # mesh type is region-wise
      reg =    1           # number of crossing regions
        non    r-in    r-out     area
        1     1400     9997      25.0
      e-type =    3             # e-mesh is given by the below data
       ne =   100           # number of e-mesh points
      emin =  1.0E-9
      emax =  10.0
     unit =   3            # unit is [1/cm2/Lethargy/source]
     axis =  eng            # axis of output
     file =  cross_Be.out      # file name of output for the above axis
   output =  flux       # surface crossing current [1/cm^2/source]
      part =  neutron
    epsout =    1            # (D=0) generate eps file by ANGEL
   $ctmin(1)  = 1
   $ctmax(1)  = 1

[END]
```

A1. Geometry of the 3.95 MeV X-band electron linac-based compact neutron source simulation

1. Basic geometry

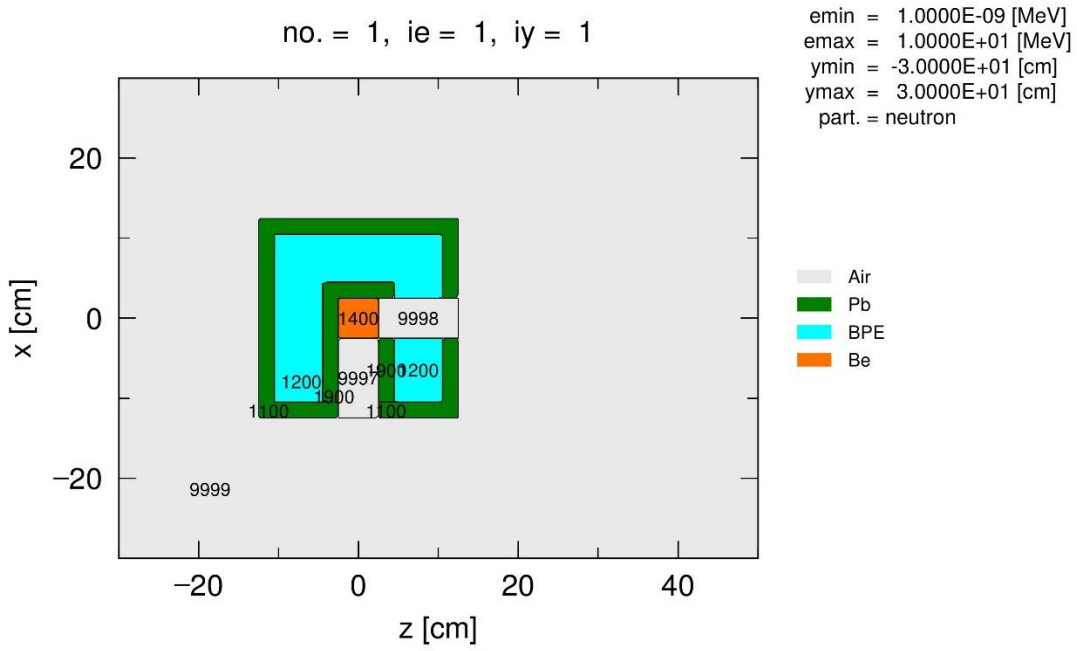

2. Irradiation with X-ray source

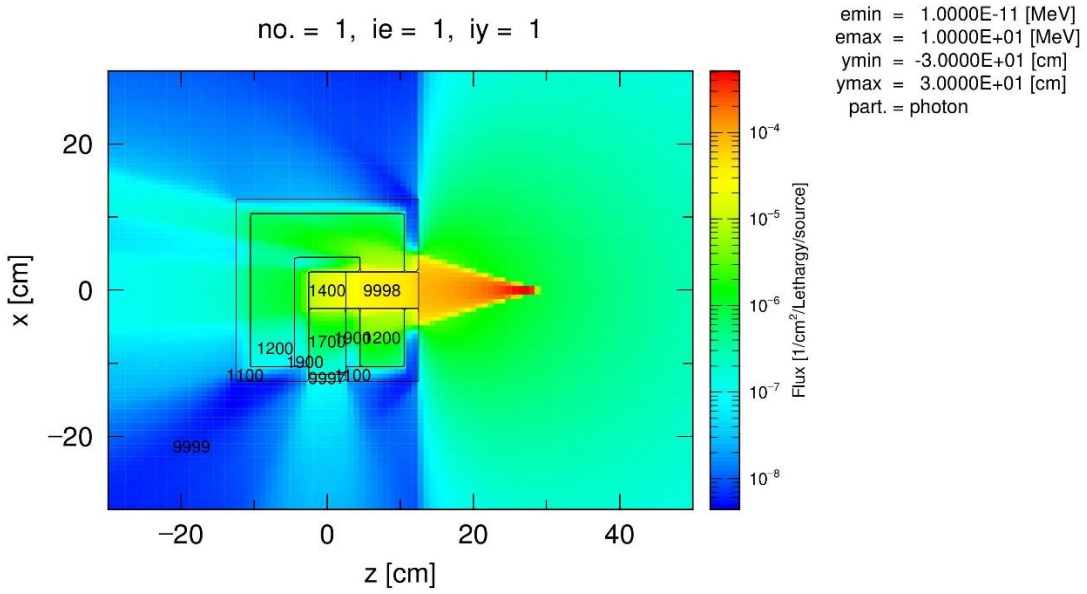

2. Neutron distribution

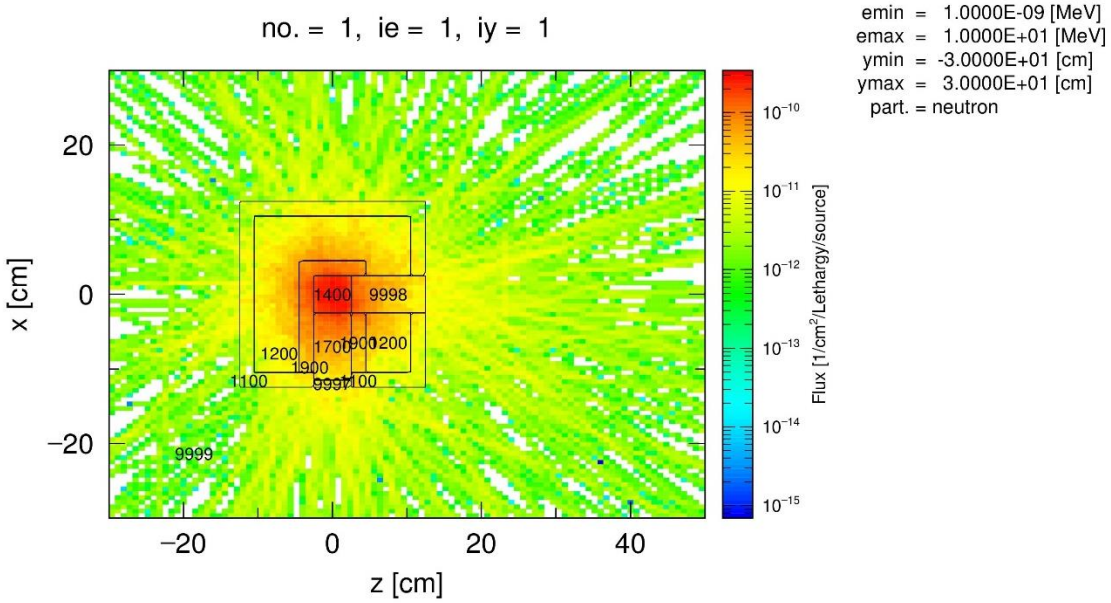

Appendix B. PHITS simulation code of NRTA experiment with uranium-plutonium mix sample using 3.95 MeV X-band electron linac-based compact neutron source

```
[ T i t l e ]
U-Pu NRTA measurement test

[ P a r a m e t e r s ]
$ mode
$ 7: t-gshow, 11 t-3dshow
$ 5: Source Check
icntl = 0

$ event number
maxcas = 1.0E5

$ batch number
maxbch = 4.0E3

itall = 1
istdev = -1

$ 2: neutron, 12: electron, 14: photon
emin(2)  = 1.0E-10
emin(12) = 1.0E-1
emin(14) = 1.0E-3
emin(13) = 1.0E-1

dmax(2)  = 100.0
dmax(12) = 100.0
dmax(14) = 100.0
dmax(13) = 100.0

$ considering photo nuclear reaction
ipnint = 1

$ Coulomb scattering
nspred = 1

$ Energy straggling of charged particle
nedisp = 1

$ Use egs5 for photon&electron
negs = 1

$ considering gamma
igamma = 1

$ bias the photo-nuclear reaction cross section
$ pnimul = 1.0

$ reading source file from dump
$ idmpmode = 1
```

```
$ event generator mode
e-mode = 2

file(6) = phits.out
file(7) = C:\phits\data\xsdir.jnd
file(14) = C:\phits\data\trxcrd.dat
file(20)= C:\phits\XS\egs

$------------------------------------------------------------------
[ S o u r c e ] #neutron source
s-type = 2 #straight beam rectangular solid
proj = neutron
x0 = -2.5
y0 = -2.5
z0 = 0.0
x1 = 2.5
y1 = 2.5
z1 = 0.0
dir = 1.0

e0 = 1.0E-8
e-type = 1
ne = 4
1.0E-8  3.0E-9
1.0E-7  1.0E-8
1.0E-6  5.0E-8
1.0E-5  4.0E-7
1.0E-4

$-----------------------------------------------------------------
[ M a t e r i a l ]
$   Air at ground level  1.21e-3 g/cm^3
mat[11] 14N 4.0586E-05
       16O 1.0800E-05
       40Ar 2.4255E-07

$   U 19.1 g/cm^3
mat[8] 238U 1.00

$   Pu 19.86 g/cm^3
mat[9] 239Pu 0.8
         242Pu 0.2

$   Cu 8.94 g/cm^3
mat[2] 63Cu 69.15
       65Cu 30.85

$   Pb 11.34 g/cm^3
mat[3] 204Pb 0.014
       206Pb 0.241
       207Pb 0.221
       208Pb 0.524

$   BPE 1.00 g/cm3
mat[4] 1H  0.4495
       12C 0.1550
       10B 0.0924
       16O 0.3031
```

```
$   Be 1.85 g/cm^3
mat[6] 9Be 1.0

$   Helium-3 detector 0.325e-3 g/cm^3
mat[7]  3He 1.0

$-------------------------------------------------------------------
[ Mat Name Color ]
mat   name      color
11    Air       lightgray
2     Cu        red
3     Pb        darkgreen
4     BPE       cyan
6     Be        orange
7    Helium-3   yellow
8    Uranium     green
9    Plutonium   blue

$-------------------------------------------------------------------
[ S u r f a c e ]
$ Atmosphere around Neutron Source
999 rpp -10000.0 10000.0
        -10000.0 10000.0
        -10000.0 10000.0

$ Atmosphere on Boron block
998 rpp -1.5 1.5
        -5.0 5.0
         250.0 256.0

$-------------- BPE moderator --------------
100 rpp -4.5 4.5
        -5.0 5.0
         250.0 256.0

$-------------- Uranium sample --------------
200 rpp -1.5 1.5
        -5.0 5.0
         250.0 250.05

$-------------- Plutonium sample --------------
300 rpp -1.5 1.5
        -5.0 5.0
         250.06 250.11

$----------------------New detection points at certain distance--------
$--------- T-Cross Tally for Neutron : detection point 1 (2.5 m) -----
201 rpp -1.5 1.5
        -5.0 5.0
         252.0 255.0

$----------------------New detection points at certain distance------
$------ T-Cross Tally for Neutron : detection point 2 (in front) ------
202 rpp -1.5 1.5
        -5.0 5.0
         249.0 249.9
```

```
[ C e l l ]
$-------------- Outer void --------------
$ Outer void
99999 -1 999

$-------------- Atmosphere --------------
$ Surrounding Atmosphere
9999 11 -1.21e-3 -999 #9998 #9997 #9996 #1100 #1200 #1300
9998 11 -1.21e-3 -998 #1200 #9997 #1300
9997 7  -3.25e-3 -201 $ detection point 2.5m at detector
9996 11 -1.21e-3 -202 $ detection point in front of sample

$-------------- BPE moderator --------------
1100 4 -1.000 -100 #9998 #9997 #1200 #1300

$-------------- Uranium sample --------------
1200 8 -19.1 -200

$-------------- Plutonium sample --------------
1300 9 -19.86 -300

$---------------------------------------------------------------------
[ T - T r a c k ] # neutron track
     mesh =  xyz             # mesh type is xyz scoring mesh
   x-type =    2         # x-mesh is linear given by xmin, xmax and nx
       nx =  100             # number of x-mesh points
     xmin =  -20        # minimum value of x-mesh points
     xmax =   20        # maximum value of x-mesh points
   y-type =    2             # y-mesh is given by the below data
       ny =   1            # number of y-mesh points
     ymin =   -20
     ymax =    20
   z-type =    2         # z-mesh is linear given by zmin, zmax and nz
       nz =  100             # number of z-mesh points
     zmin =  -20         # minimum value of z-mesh points
     zmax =  270         # maximum value of z-mesh points
     part = neutron
      e-type =  5              # e-mesh is given by the below data
      edel = log(10)
      emin =  1.0E-8
      emax =  1.0E-4
     unit =   1             # unit is [1/cm2/Lethargy/source]
     axis =   xz             # axis of output
     file = track_xz_neutron.out    # file name of output for axis
    title = Geometry of Neutron Track Detection using [T-track] tally
    gshow =    3           # 0: no 1:bnd, 2:bnd+mat, 3:bnd+reg 4:bnd+lat
   epsout =    1             # (D=0) generate eps file by ANGEL

$---------------------------------------------------------------------
[ T - T r a c k ] # neutron track (zoom)
     mesh =  xyz             # mesh type is xyz scoring mesh
   x-type =    2          # x-mesh is linear given by xmin, xmax and nx
       nx =  100             # number of x-mesh points
     xmin =  -4        # minimum value of x-mesh points
     xmax =   4        # maximum value of x-mesh points
   y-type =    2             # y-mesh is given by the below data
       ny =   1            # number of y-mesh points
     ymin =   -5
```

```
     ymax =    5
   z-type =    2          # z-mesh is linear given by zmin, zmax and nz
       nz =  100            # number of z-mesh points
     zmin =  249         # minimum value of z-mesh points
     zmax =  254         # maximum value of z-mesh points
     part = neutron
      e-type =  5             # e-mesh is given by the below data
      edel = log(10)
      emin =  1.0E-8
      emax =  1.0E-4
     unit =   1            # unit is [1/cm2/Lethargy/source]
     axis =   xz            # axis of output
     file = track_xz_neutron_zoom.out    # file name of output for axis
    title = Geometry of Neutron Track Detection using [T-track] tally
    gshow =    3          # 0: no 1:bnd, 2:bnd+mat, 3:bnd+reg 4:bnd+lat
   epsout =    1            # (D=0) generate eps file by ANGEL

$-------------------------------------------------------------------
[ T - C r o s s ] # neutron spectrum in front of sample
    title = Energy distribution in region mesh
     mesh =  reg            # mesh type is region-wise
      reg =    1           # number of crossing regions
        non    r-in    r-out     area
        1       9999   9996      30.0
        e-type =  3        # e-mesh is given by the below data
        ne = 250
        emin =  1.0E-8
        emax =  1.0E-4
     unit =  1            # unit is [1/cm^2/MeV/source]
     axis =  eng            # axis of output
     file =  cross_front.out      # file name of output for axis
   output =  flux        # surface crossing current [1/cm^2/source]
      part =  neutron
    epsout =    1            # (D=0) generate eps file by ANGEL
   $ctmin(1)  = 1
   $ctmax(1)  = 1

$-------------------------------------------------------------------
[ T - C r o s s ] # neutron spectrum at detector
    title = Energy distribution in region mesh
     mesh =  reg            # mesh type is region-wise
      reg =    1           # number of crossing regions
        non    r-in    r-out     area
        1      9998    9997      30.0
        e-type =  3             # e-mesh is given by the below data
        ne = 250
      emin =  1.0E-8
      emax =  1.0E-4
     unit =   1            # unit is [1/cm^2/source]
     axis =  eng            # axis of output
     file =  cross_250cm.out      # file name of output for axis
   output =  flux        # surface crossing current [1/cm^2/source]
      part =  neutron
    epsout =    1            # (D=0) generate eps file by ANGEL
   $ctmin(1)  = 1
   $ctmax(1)  = 1

[END]
```

B1. Geometry of the NRTA experiment with Uranium-Plutonium mix sample

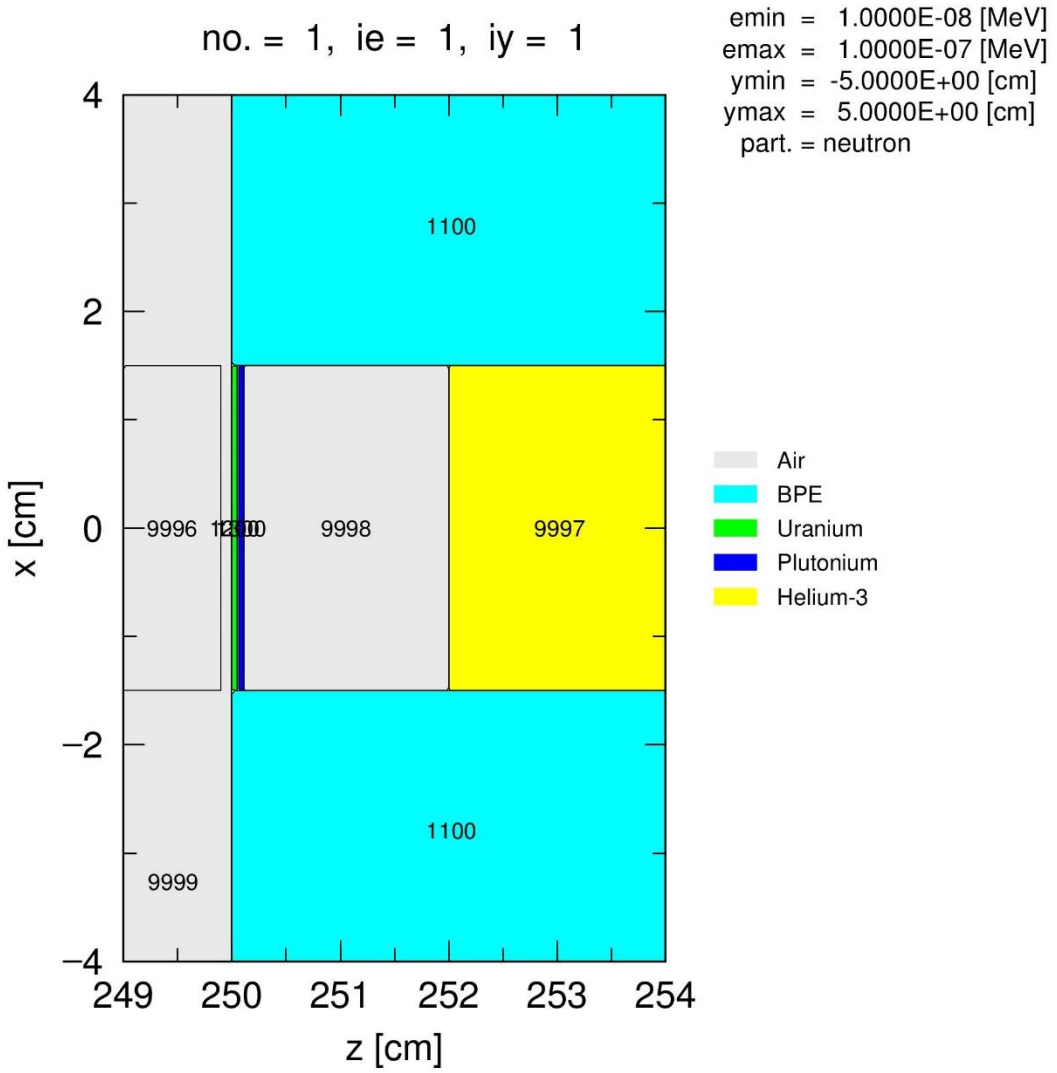

Appendix C. Python code for converting neutron TOF count into neutron energy spectrum

```
# -*- coding: utf-8 -*-
# 32 bit clock counting with MAX II board.

import numpy as np
import matplotlib.pyplot as plt

def clkcnts_to_energy(count, num_data, tof_length):
      count = count[:,1]
      count = count[0: (num_data*2) ]

      # Data n and n+1 are a pair. (n: even number, n+1: odd number)
      ind = np.asarray( range(0, num_data*2) )

      # even number data = Upper 16 bit
      upper = count[ ind%2==0 ]

      # odd number data = Lower 16 bit
      lower = count[ ind%2==1 ]

      # convert clock count to TOF (s)
      data = upper * 65536 + lower
      tof = data * clock * 1.0E-9

      # tof to velocity (m/s)
      velocity = tof_length/tof

      # velocity to energy (eV)
      energy = 5.223E-9 * velocity * velocity

      return energy

clock = 8 # ns
tof_length = 2.5 # m
hist_bins = 250
min_e_order = -1 # 10^-1 eV
max_e_order = 2  # 10^2 eV

# Note : Thermal neutron flies 1 m in 450 us

count  = np.loadtxt("./memory_data.txt")
energy = clkcnts_to_energy(count=count, num_data=71746,
tof_length=tof_length)

x = np.logspace(min_e_order, max_e_order, hist_bins)

hist, border = np.histogram(energy, bins=x, density=True)

print "hist.shape = ", hist.shape
```

```
print "x.shape = ", x.shape
print "border.shape = ", border.shape
print "Check the difference of x and border = ", x - border # should
be zeros (x and border are same)

print "bin width = ", np.diff(border)
print "hist (normalized count density) = ", hist

# differences between elements = binning widths
#bin_w = np.diff(border)
#hist = hist / bin_w

# representative values for histgram bins.
# deleting the last value to match the size of 'hist' and 'rep_bins'
rep_bins = np.delete(border, -1)
print "rep_bins.shape = ", rep_bins.shape
print "rep_bins = ", rep_bins

# font size
plt.rcParams['font.family'] = 'Arial'
plt.rcParams['font.size'] = 18

plt.title("Neutron energy measurements by TOF method")
plt.ylabel("Normalized counts (/eV)")
plt.xlabel("Energy (eV)")
#plt.xlim([1.0E-1, 1.0E+2])
plt.xlim([1.0E-1, 7.0E+1])
#plt.ylim([0, 500])

plt.plot(rep_bins, hist, '.-', label="No sample, 1 hour")
plt.xscale('log')
plt.yscale('log')
plt.grid(which='major')
plt.grid(which='minor')
plt.legend()
plt.tick_params()
#plt.savefig("output_density-by-histogram-function.png")
plt.show()
```

References

[1] www.tepco.co.jp/en/press/corp-com/release/betu12_e/images/120620e0104.pdf

[2] http://www.world-nuclear.org/information-library/safety-and-security/safety-of-plants/fukushima-accident.aspx

[3] Compensation ND. Technical Strategic Plan 2017 for Decommissioning of the Fukushima Daiichi Nuclear Power Station of Tokyo Electric Power Company Holdings, Inc. Japan: NDF; 2017.

[4] http://www.meti.go.jp/english/earthquake/nuclear/decommissioning/#roadmap

[5] M. Takano, et al. “Revisiting the TMI-2 core melt specimens to verify the simulated corium for Fukushima Daiichi NPS”, Proceedings for HOTLAB 2017, Sep 17-22, 2017, Mito, Japan.

[6] Sevón, Tuomo. "Molten core-concrete interactions in nuclear accidents." Theory and Design of an Experimental Facility. VTT Research Notes 2311 (2005).

[7] T. Washiya. “International collaborations at JAEA/CLADS toward decommissioning of Fukushima Daiichi NPS”. Proceedings for HOTLAB 2017, Sep 18, 2017, Mito, Japan.

[8] F. Tanabe, “Analysis of core melt accident in Fukushima Daiichi-Unit 1 nuclear reactor”, J. Nucl. Sci. Technol. 48 (2011) 1135-1139.

[9] Kawano, S., Hayashi, T., Morishima, Y., Takahashi, Y., Toyohara, M., Baklanov, V.V., Kolodeshnikov, A.A. and Zuev, V.A., 2017. Characterization of fuel debris by large-scale simulated debris examination for Fukushima Daiichi Nuclear Power Stations. ICAPP2017: 2017 international congress on advances in nuclear power plants; Fukui (Japan); 24-25 Apr 2017;

[10] M. Saeki, A. Iwanade, C. Ito, I. Wakaida, B. Thornton, T. Sakka, H. Ohba: "Development of a fiber-coupled laser-induced breakdown spectroscopy instrument for analysis of underwater debris in a nuclear reactor core." J. Nucl. Sci. Technol., Vol. 51, No. 7-8, pp.930-938 (2014).

[11] International Research Institute for Nuclear Decommissioning: “Development of Technology for Fuel Debris Analysis/Fuel Debris Characterization.” Annual Research Report 2017, IRID, Japan (2018).

[12] The Robotics Society of Japan. Robot technology competition for nuclear reactor decommissioning. Japan: RSJ; 2017.

[13] Kaneyasu T, Uesaka M, Dobashi K, Torikoshi M. Dual-energy X-ray CT by Compton scattering hard X-ray source. Proc. PAC 2005; 2005 May 16; Knoxville (USA).

[14] L. De Chiffre, S. Carmignato, J-P. Kruth, R. Schmitt, A. Weckenmann: "Industrial applications of computed tomography." CIRP Annals-Manufacturing Technology, Vol. 63, No. 2, pp.655-677 (2014).

[15] A. Ohzu, M. Komeda, M. Kureta, N. Zaima, Y. Nakatsuka, S. Nakashima: "Development of non-destructive assay system using fast neutron direct interrogation method for actual uranium waste drums." Nippon Genshiryoku Gakkai Wabun Ronbunshi, Vol. 15, No. 2, pp.115-127 (2016).

[16] H. Postma and P. Schillebeeckx, "Neutron Resonance Capture and Transmission Analysis", Encyclopedia of Analytical Chemistry (John Wiley & Sons Ltd), pp. 1-22 (2009).

[17] P. Schillebeeckx, A. Borella, F. Emiliani, G. Gorini, W. Kockelmann, S. Kopecky, C. Lampoudis, M. Moxon, E. Perelli Cippo, H. Postma, N.J. Rhodes, E.M. Schooneveld and C. Van Beveren, "Neutron resonance spectroscopy for the characterization of materials and objects", J. Instrum. 7, C03009 – 18 (2012).

[18] Knoll, Glenn F. Radiation detection and measurement. John Wiley & Sons, 2010.

[19] P. Schillebeeckx, B. Becker, Y. Danon, K. Guber, H. Harada, J. Heyse, A.R. Junghans, S. Kopecky, C. Massimi, M. Moxon, N. Otuka, I. Sirakov and K. Volev, "Determination of Resonance Parameters and their Covariances from Neutron Induced Reaction Cross Section Data", Nucl. Data Sheets 113, 3054 – 3100 (2012).

[20] Shibata K, Iwamoto O, Nakagawa T, Iwamoto N, Ichihara A, Kunieda S, Chiba S, Furukawa K, Otuka N, Ohsawa T, Murata T, Matsunobu H, Zukaran A, Kameda S, Katakura J. JENDL-4.0: A new library for nuclear science and technology. J. Nucl. Sci. Technol. 2011 Jan; 48:1-30.

[21] Paradela, C., et al. "Characterization of nuclear material by Neutron Resonance Transmission Analysis." Nuovo Cimento C Geophysics Space Physics C 38 (2016).

[22] C. Paradela, G. Alaerts, B. Becker, H. Harada, J. Heyse, F. Kitatani, M. Koizumi et al: "NRD Demonstration Experiments at GELINA." JRC Technical Report, Report EUR 27507 EN (2015).

[23] Sano, Tadafumi, et al. "Analysis of energy resolution in the KURRI-LINAC pulsed neutron facility." EPJ Web of Conferences. Vol. 146. EDP Sciences, 2017.

[24] http://www.rri.kyoto-u.ac.jp/en/facilities/ela

[25] Mori, Y., " Neutron Sources at KURRI." The first meeting of Union for Compact Accelerator-driven Neutron Source (UCANS-1), 2010 Aug 15-18, Beijing (China).

[26] http://phi.phys.nagoya-u.ac.jp/JCANS/huns.html

[27] Sato, Hirotaka, et al. "Performance of the Bragg-edge transmission imaging at a compact accelerator-driven pulsed neutron source." Physics Procedia 60 (2014): 254-263.

[28] Furusaka, Michihiro, et al. "Activity of Hokkaido University neutron source, HUNS." Physics Procedia 60 (2014): 167-174.

[29] Kiyanagi, Y., et al. "A new imaging method using pulsed neutron sources for visualizing structural and dynamical information." Journal of Physics: Conference Series. Vol. 340. No. 1. IOP Publishing, 2012.

[30] Naoi Yosuke, "JAEA's R&D Activities Related to Measurement and Detection of Nuclear Material and Nuclear Forensics for Nuclear Security and Safeguards." International Symposium on Technology Development for Nuclear Security, 2016 Oct 27, Tokyo (Japan).

[31] Kazuki Inoue, Kai Masuda, Taiju Kajiwara, Ryota Nakamatsu, Kazunobu Nagasaki. "Development of High-power pulsed DD-IEC neutron source for Nuclear Material Detection System." Inst. Advanced Energy, Kyoto University.

[32] http://www.adelphitech.com/products/dt109-dt110.html

[33] Auditore, L., Barna, R.C., De Pasquale, D., Italiano, A., Trifiro, A. and Trimarchi, M., 2005. Study of a 5 MeV electron linac based neutron source. Nuclear Instruments and Methods in Physics Research Section B: Beam Interactions with Materials and Atoms, 229(1), pp.137-143.

[34] Gunderson, Leonard L. Clinical radiation oncology. Elsevier Health Sciences, 2015.

[35] Uesaka, M., et al. "30 MeV X-band Electron Linac Neutron Source for Nuclear Data Study for Fukushima Accident Analysis." Physics Procedia 60 (2014): 193-202.

[36] http://indico.cern.ch/conferenceDisplay.py?confId=231116

[37] Uesaka M, Mitsuya Y, Hashimoto E, Dobashi K, Yano R, Takeuchi H, Bereder JM, Kusano J, Tanabe E, Maruyama N, Hattori Y. On-Site Non-Destructive Inspection of Bridges Using the 950 keV X-Band Electron Linac X-ray Source (Special Issue on Infrastructure Maintenance, Renovation and Management). Journal of disaster research. 2017 Jun; 12(3):578-584.

[38] Uesaka, Mitsuru, et al. "Applications of X-band 950 KeV and 3.95 MeV linac x-ray source for onsite inspection." Proceedings of IPAC (2012): 4071-4073.

[39] Graham, Donald, Paul Cloke, and Martin Vosper. Principles and applications of radiological physics. Churchill Livingstone, 2011.

[40] Holmes, R. J. "Gamma-Ray and Neutron Sources." in the Mineral Industry (1982): 123.

[41] Chadwick, M. B., et al. "Handbook on photonuclear data for applications: Cross sections and spectra." IAEA TECH-DOC 1178 (2000).

[42] Eshwarappa, K. M., et al. "Comparison of photoneutron yield from beryllium irradiated with bremsstrahlung radiation of different peak energy." Annals of Nuclear Energy 34.11 (2007): 896-901.

[43] J. Bereder, Y. Mitsuya, Y. Takahashi, K. Dobashi, M. Uesaka, J. Kusano, Y. Tanaka, Y. Oshima, M. Ishida: "Development of 3.95 MeV X-band linac-driven x-ray combined neutron source." IOP Publishing, Journal of Physics: Conference Series, Vol. 874, No. 1, pp.012104 (2017).

[44] Kusumawati Y., et al, "X-band Electron Linac-based Compact Neutron Source for Nuclear Material Detection" 7th International Symposium on Energy, Manchester, United Kingdom. 2017.

[45] United States Government Accountability Office, "Neutron Detectors - Alternatives to using Helium-3," Center for Science, Technology, and Engineering, September 2011.

[46] Saint-Gobain. (2014). Gas-Filled Radiation Detectors Helium-3 Proportional Counters. Retrieved from http://www.oilandgas.saint-gobain.com/uploadedFiles/SGoilandgas/Documents/Detectors/Detectors-Helium-3-Tubes.pdf

[47] Kouzes, RT. 2009a. "The ^{3}He Supply Problem," Technical Rpt. PNNL-18388, Pacific Northwest National Laboratory, Richland, WA.

[48] Kouzes, Richard T., et al. "Alternatives to ^{3}He for neutron detection for homeland security." Proceedings INMM 51st Annual Meeting, Baltimore, MD USA. 2010.

[49] A. Yamazaki, et al., Nucl. Instr. and Meth. A (2011), doi:10.1016/j.nima.2011.02.064

[50] Schillebeeckx P, Becker B, Harada H, Kopecky S. Neutron resonance spectroscopy for the characterization of materials and objects. In Supplement to Volume I/24 (pp. 10-66). Berlin: Springer; 2015.

[51] Ametek Inc. (2014). 556 and 556H High-Voltage Power Supply. Retrieved from www.ortec-online.com/download/556-556H.pdf

[52] Nicholas Tsoulfanidis, "Measurement and Detection of Radiation", Hemisphere Publishing Corporation, 1983.

[53] Ametek Inc. (2014). Preamplifier Introduction. Retrieved from www.ortec-online.com/download/Preamplifier-Introduction.pdf

[54] Ametek Inc. (2014).572A Amplifier. Retrieved from www.ortec-online.com/download/572a.pdf

[55] https://www.electronics-tutorials.ws/opamp/op-amp-comparator.html

[56] Smat, Radim. "Introduction to comparators, their parameters and basic applications." STMicroelectronics, App. Note 4071 (2012).

[57] Tektronix, Inc. (2015). MSO/DPO2000B Mixed Signal Oscilloscope. Retrieved from http://www.tek.com/oscilloscope/mso2000-dpo2000

[58] https://www.omega.ca/techref/das/divider.html

[59] Maxfield, Clive. FPGAs: instant access. Newnes, 2011.

[60] A. Brusegan, G. Noguere, F. Gunsing: "The resolution function in neutron time-of-flight experiments." J. Nucl. Sci. Technol., Vol. 39, No. sup2, pp.685-688 (2002).

[61] N. Shigyo, Y. Iwamoto, D. Satoh, H. Kitsuki, K. Ishibashi, and M. Numajiri: "Improvement of energy resolution in time-of-flight method for high energy neutron measurement." IEEE, Nuclear Science Symposium Conference Record, Vol. 1, pp.6-215 (2000).

[62] M. Uesaka, Y. Mitsuya, K. Dobashi, J. Kusano, E. Yoshida, Y. Oshima, M. Ishida: "On-site Bridge Inspection by 950 keV / 3.95 MeV Portable X-band Linac X-ray Sources." Bridge Optimization - Inspection and Condition Monitoring, IntechOpen, London, ISBN 978-953-51-8054-8 (2018).